

POLITECNICO DI TORINO

Master's Degree in Civil Engineering



Master thesis:

FLUID-DYNAMICS AND FLUTTER ANALYSIS OF THE GEORGE WASHINGTON SUSPENSION BRIDGE

Supervisors:

Prof. Alberto Carpinteri

Prof. Gianfranco Piana

Dott. Luca Patruno

Candidate:

Sebastiano Russo

Academic Year 2018/2019

Ringraziamenti

Porgo i miei più sentiti ringraziamenti all'istituzione Politecnico di Torino ed ai docenti che mi hanno accompagnato durante il corso di studi ed hanno contribuito alla mia crescita personale e delle mie conoscenze.

Un particolare ringraziamento va al Prof. Alberto Carpinteri che ha fatto crescere in me la curiosità riguardo specifiche criticità dell'ingegneria strutturale, fra le quali l'instabilità aeroelastica dei ponti sospesi, oggetto della tesi.

Ringrazio il Prof. Gianfranco Piana ed il Dott. Luca Patruno, che con grande disponibilità, professionalità e pazienza mi hanno seguito in questo stimolante percorso di tesi in qualità di corelatori.

Ringrazio inoltre tutti i miei amici, la mia fidanzata, i colleghi, e tutte le persone che hanno contribuito ad rallegrare ed alleggerire il mio percorso di studi.

Il ringraziamento più sentito va alla mia famiglia, che mi ha sempre donato fiducia e sostenuto nei momenti di difficoltà e debolezza. Gran parte del merito per il raggiungimento di questo traguardo va a loro.

Abstract

The aim of this thesis is to analyze the behavior of suspension bridges under wind loads. In particular, the George Washington bridge has been chosen as a case study, in both original and latest stiffened versions respectively of 1931 and 1962. The goal is to determine the critical wind velocity that leads the bridge to the well-known phenomenon of flutter instability adopting a commercial finite element software and to find a simplified approach for the estimation of the motion-related wind loads. The research is also focused on the study of the computational fluid dynamic models aimed at determining the aerodynamic parameters on which the approach mentioned before is based.

The work is divided in two parts, a first part containing the theoretical and bibliographical background on which the calculations carried out in the second part are based.

The first part begins with considerations regarding the description of wind effects on suspension bridges, some analytical approaches and descriptions of the phenomenon of flutter instability are presented, with an in-depth reference to the method used by the software adopted. A chapter was subsequently dedicated to the description of the load acting on an oscillating body in a uniform airflow by different authors. The strong duality between time-domain and frequency-domain representations is focused with the aim of reporting a relationship between flutter derivatives, Theodorsen functions and aerodynamic static coefficients. The final chapter of the first part is dedicated to a brief introduction to the computational fluid dynamic followed by some examples of application to bridge decks.

The second part starts with an application of the formulas developed in the first part for the calculation of flutter derivatives; the Great Belt and the Akashi Kaykio bridges were chosen as case studies. In the next chapter, several CFD analysis with ANSYS FLUENT have been carried out with the aim of obtaining the aerodynamic static coefficients of the bridges mentioned before. The results were compared with the data found in the literature and then the same parameters of George Washington Bridge have been calculated with the same approach. Thereafter considerations were made about numerical modelling of suspension bridges in ANSYS APDL. Some bridges have been modeled in order to make a comparison between the results obtained and the literature data. In the end a flutter analysis of the two versions of George Washington bridge have been carried out and it was possible to draw conclusions on the influence of the lower deck on the aerodynamic performance of the bridge.

Table of Contents

Abstract.....	I
List of figures.....	IV
List of tables.....	VI
PART 1.....	1
1. INTRODUCTION.....	2
1.1. George Washington Bridge.....	5
2. MOTION RELATED WIND LOADS.....	7
2.1. Problem setting and background.....	8
2.2. Thin airfoil.....	9
2.3. Bridge deck sections.....	11
2.3.1. Frequency-domain.....	11
2.3.2. Time-domain.....	12
2.3.3. Time-frequency duality.....	13
2.4. A simplified approach for flutter derivatives.....	15
3. CFD FOR THE EVALUATION OF AERODYNAMIC COEFFICIENTS.....	17
3.1. Overview on turbulence modeling.....	18
3.2. Aerodynamic analysis of Great Belt East.....	19
3.3. Aerodynamic performance of a steel truss stiffening girder.....	22
4. FLUTTER OF LONG SPAN BRIDGES.....	24
4.1. Dynamic instability.....	25
4.2. Two degrees of freedom flutter.....	27
4.3. Three degrees of freedom flutter.....	30
4.4. Flutter analysis using ANSYS.....	31
PART 2.....	34
5. FLUTTER DERIVATIVES FROM PRESSURE COEFFICIENTS.....	35
5.1. Flutter derivatives of Great Belt Est Bridge.....	36
5.2. Flutter derivatives of Akashi Kaykio.....	38
6. CFD SIMULATIONS.....	40
6.1. Great Belt East.....	42
6.2. Akashi Kaiyko.....	44

6.3. George Washington Bridge, single deck (1931).....	48
6.4. George Washington Bridge, double deck (1962).....	50
7. FLUTTER ANALYSIS OF GEORGE WASHINGTON BRIDGE.....	52
7.1. Simply supported thin airfoil structure.....	53
7.2. George Washington Bridge, single deck (1931).....	56
7.3. George Washington Bridge, double deck (1962).....	60
7.3.1. First method.....	63
7.3.2. Second method.....	65
7.3.3. Comparison between the two methods.....	67
8. CONCLUSIONS AND FURTHER DEVELOPMENTS.....	68
References.....	69

List of figures

Figure 1.1: Suspension bridge at Jacob's Creek in Westmoreland County [1]	2
Figure 1.2: Tacoma Narrows collapse [3].....	3
Figure 1.3: Motion for an Airfoil Exhibiting Flutter [4].	4
Figure 1.4: George Washington bridge, single deck [5].	5
Figure 1.5: George Washington Bridge, double deck [6].	6
Figure 2.1: Sectional model [10].	8
Figure 2.2: Real and Imaginary part of Theodorsen Function [11].	9
Figure 3.1: Aircraft in a fluid flow [19]	17
Figure 3.2: Numerical approaches for turbulence modeling [20].	18
Figure 3.3: Comparison between experimental (a), LES (b) and RANS (c) turbulent structures [25].....	19
Figure 3.4: View of the Great Belt East Bridge [21].	20
Figure 3.5: Cross-section (scale 1:80, dimension in mm) and the adopted mesh structure [12].	20
Figure 3.6: Variation of the pressure coefficients with the angle of incidence [21].	21
Figure 3.7: outline of the steel truss stiffening girder (in millimeters) [30].	22
Figure 3.8: Local computational mesh of the 2D model [30].	23
Figure 4.1: View of the Golden Gate Bridge [31].	24
Figure 4.2: Representation of dynamic instability [32].	26
Figure 4.3: Two degrees of freedom simplified model.	27
Figure 4.4: Examples of flutter derivatives [17].	28
Figure 4.5: Three degrees of freedom sectional model [33].	30
Figure 4.6: Hybrid finite element model [33].	32
Figure 5.1: Comparison between flutter derivatives of thin airfoil and streamlined cross-sections [17]. ..	35
Figure 5.2: Moment flutter derivatives of the Great Belt Est.	36
Figure 5.3: Lift flutter derivatives of Great Belt Est.	37
Figure 5.4: View of Akashi Kaykio Bridge [37].	38
Figure 5.5: Moment flutter derivatives of the Akashi Kaykio.	39
Figure 5.6: Lift flutter derivatives of Akashi Kaykio.	39
Figure 6.1: Geometrical division of the computational domain.	40
Figure 6.2: Discretization of the fluid domain.	41
Figure 6.3: Discretization of the inner regions closest to the deck.	41
Figure 6.4: Great belt East cross-section.	42
Figure 6.5: Distribution of velocity magnitude and static pressure around the deck with $\alpha = 0^\circ$	42
Figure 6.6: Distribution of velocity magnitude and static pressure around the deck with $\alpha = \pm 5^\circ$	43
Figure 6.7: Aerodynamic static coefficients of Great Belt East as functions of the angle of attack.	43
Figure 6.8: View of the Akashi Kaikyo lower level.	44
Figure 6.9: 3D model of the Akashi Kaikyo truss girder.	44
Figure 6.10: Distribution of velocity magnitude and static pressure around the deck with $\alpha = 0^\circ$	45
Figure 6.11: Distribution of velocity magnitude and static pressure around the deck with $\alpha = \pm 5^\circ$	46
Figure 6.12: Aerodynamic static coefficients of Akashi Kaikyo as functions of the angle of attack.	46
Figure 6.13: View of the lower deck of George Washington Bridge.	47
Figure 6.14: Distribution of velocity magnitude and static pressure around the deck with $\alpha = 0^\circ$	48

Figure 6.15: Aerodynamic static coefficients of George Washington Bridge (first version) as functions of the angle of attack.	49
Figure 6.16: Distribution of velocity magnitude and static pressure around the deck with $\alpha = 0^\circ$	50
Figure 6.17: Aerodynamic static coefficients of George Washington Bridge (last version) as functions of the angle of attack.	51
Figure 7.1: Finite element model for flutter analysis.	54
Figure 7.2: Flutter derivatives for thin airfoil.....	54
Figure 7.3: Variation of imaginary and real parts of the 2 nd complex eigenvalue versus wind velocity. ...	55
Figure 7.4: Finite element model of the George Washington Bridge (1931) without MATRIX27.	57
Figure 7.5: Finite element model with MATRIX 27 incorporated.	58
Figure 7.6: Flutter derivatives of George Washington Bridge (1931).	58
Figure 7.7: Variation of real and imaginary parts of complex eigenvalues versus wind velocity.	59
Figure 7.8: Variation of real and imaginary parts of the flutter mode.	59
Figure 7.9: Finite element model of the George Washington Bridge (1962) without MATRIX27.	60
Figure 7.10: Schematization of the first method for the application of aeroelastic loads.	62
Figure 7.11: Schematization of the second method for the application of aeroelastic loads.	62
Figure 7.12: Finite element model with MATRIX 27 incorporated.	63
Figure 7.13 Flutter derivatives of George Washington Bridge (1962).	63
Figure 7.14: Variation of real and imaginary parts of complex eigenvalues versus wind velocity.	64
Figure 7.15: Variation of real and imaginary parts of the flutter mode.	64
Figure 7.16: Finite element model with MATRIX 27 incorporated.	65
Figure 7.17: Variation of real and imaginary parts of complex eigenvalues versus wind velocity.	66
Figure 7.18: Variation of real and imaginary parts of the flutter mode versus wind velocity.	66
Figure 7.19: Variation of real and imaginary parts of the torsional modes versus wind velocity.	67

List of tables

Table 3-1: Experimental and numerical aerodynamic coefficients slope [21].	21
Table 3-2: Flutter conditions of the suspension bridge [30].	23
Table 5-1: Slope of the pressure coefficients of Great Belt Est.	37
Table 5-2: Slope of the pressure coefficients of Akashi Kaykio.	38
Table 6-1: Comparison of the Aerodynamic static coefficients of Akashi Kaykio.	46
Table 6-2: Aerodynamic static coefficients of George Washington Bridge (first version).	49
Table 6-3: Aerodynamic static coefficients of George Washington Bridge (last version).	51
Table 7-1: Model parameters of the simply supported thin airfoil.	53
Table 7-2: Modal frequencies of the simply supported thin airfoil.	54
Table 7-3: Comparison of flutter analysis results for thin airfoil bridge.	55
Table 7-4: Geometrical and mechanical properties of George Washington Bridge.	56
Table 7-5: Modal frequencies and shapes of George Washington Bridge (1931).	57
Table 7-6: Geometrical properties of the truss.	60
Table 7-7: Modal frequencies and shapes of George Washington Bridge (1962).	61

PART 1

1. INTRODUCTION

The longest span bridges in the world are currently the suspension bridges, this type of construction provides that the traffic-carrying deck is supported by a series of wire ropes that hang from massive cables draped between tall towers.

Earliest versions of suspension bridges were built by Tangtong Gyalpo, Tibetan saint and bridge builder from the 15th century. He built over 58 iron chain suspension bridges and one of these survived until 2004 when it was destroyed by a flood. Nonetheless the first iron chain suspension bridge in United States was designed by James Finley and made at Jacob's Creek in Westmoreland County, Pennsylvania in 1801. This bridge, as illustrated in *Figure 1.1* [1], was the first to have all the necessary components of a modern suspension bridge.

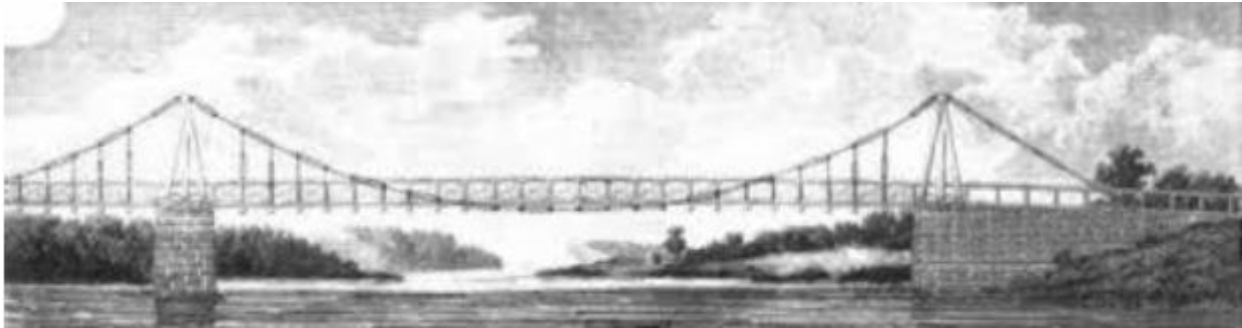


Figure 1.1: Suspension bridge at Jacob's Creek in Westmoreland County [1]

Between the 19th and the 20th centuries the historical developments of long span suspension bridges, as the main engineering advances, show an endless conflict between economy and structural performances. The use of the deflection theory allowed very slender deck for static load and shifted the design trend at that time from rigid truss to slender edge girder, this evolution ended brutally with the Tacoma Narrows Bridge disaster on November 7, 1940. Early in the morning, under a recorded wind speed of 18.8 m/s the bridge developed vertical wave motions of a character previously experienced. Then, shortly after 10:00 am, the motion changed: the main span started to vibrate with the two cables out of phase and the motion resulted in a twisting of the roadway, the tilting of the deck amounted to more than 30 degrees each way from the horizontal. As a result of this movement the main began to break up before 11:00 am (*Figure 1.2*) [2].

The failure of the Tacoma Narrows bridge is the starting point of all the studies on bridge aero-elasticity. From then on, every design of a flexible structure must assure that the structure is stable under the dynamic effects of the wind loads. In fact, wind stability has become a governing criteria in the design of long span suspension bridges.

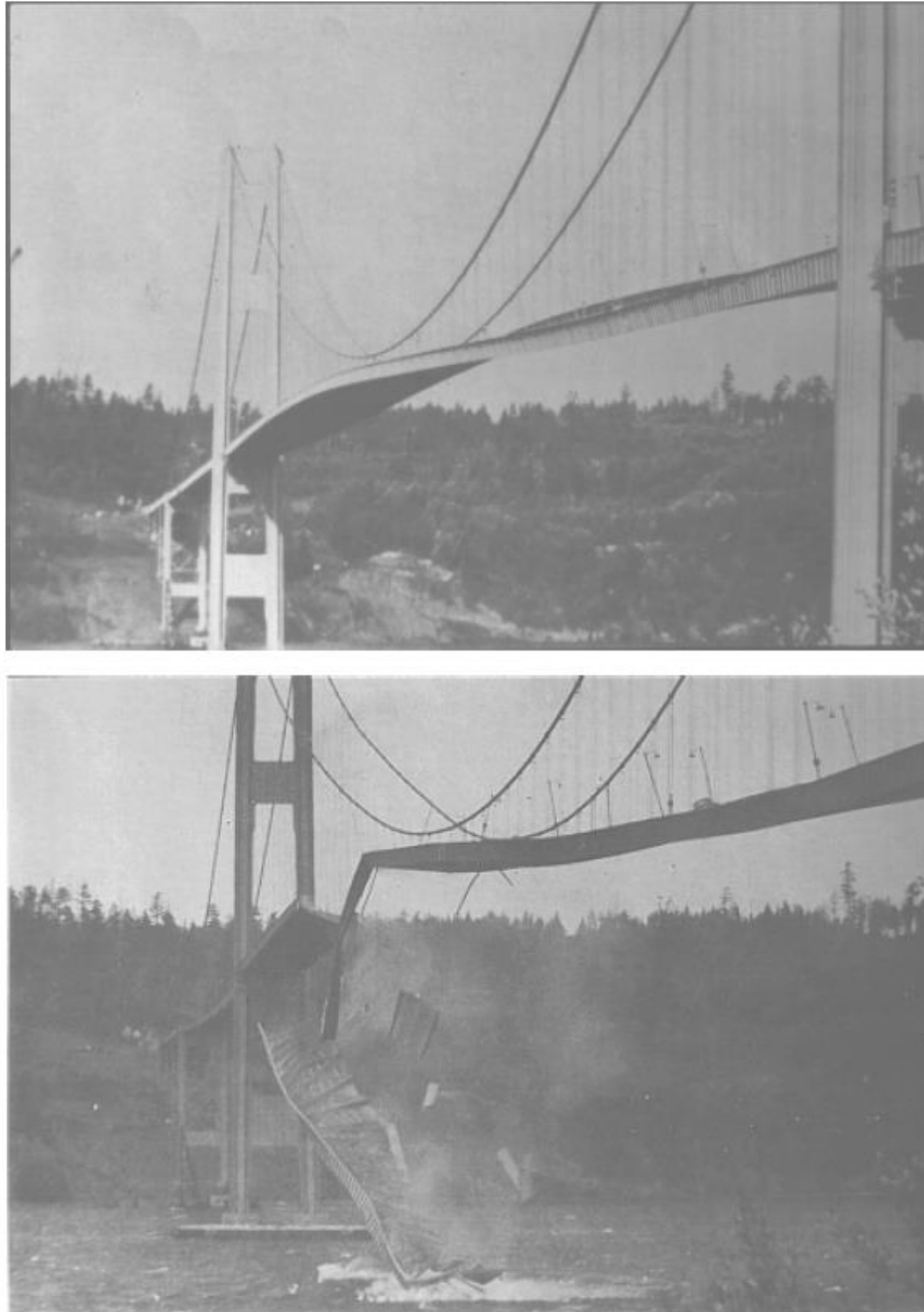


Figure 1.2: Tacoma Narrows collapse [3].

It is important to note that the phenomenon of flutter instability was observed and studied long before the collapse of Tacoma Narrows, it was a well-known concept in aeronautical field. The first recorded and documented case of flutter in an aircraft was that which occurred to a Handley Page O/400 bomber during a flight in 1916, it suffered a violent oscillation which caused extreme distortion of the rear fuselage and

the elevators to move asymmetrically. Since than considering flutter characteristic is an essential part of designing an aircraft.

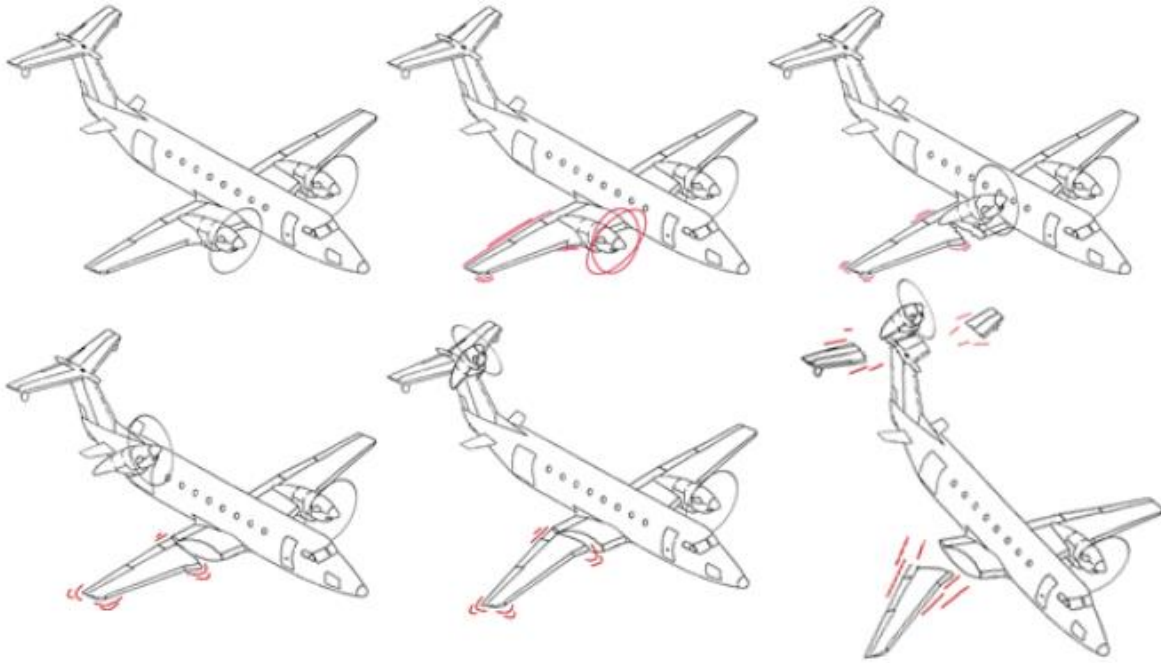


Figure 1.3: Motion for an Airfoil Exhibiting Flutter [4].

Several studies have been carried out with the aim of prevent this aero-elastic phenomenon, both in aeronautical and civil engineering field, and sometimes these studies have been compared each other leading to some interesting solutions.

1.1. George Washington Bridge

The George Washington Bridge is a suspension bridge spanning the Hudson River, it has been opened to the traffic in 1931. The bridge is made by still, has a total length of 1450 meters and a longest span of 1067m. Initially it was composed only by the upper level (*Figure 1.4*), the lower deck was constructed from 1958 to 1962 because of increasing traffic flow (*Figure 1.5*).



Figure 1.4: George Washington bridge, single deck [5].

The George Washington Bridge has been chosen as a case study because of its historical relevance, it had the longest main bridge span in the world at the time of its opening and held that distinction until 1937, when the Golden Gate Bridge was built. No studies have been found in literature regarding the aerodynamic performance of the Bridge, probably because the deck had no particular slenderness and had not the main characteristic that use to cause the flutter instability. As calculated in the final section of this thesis, the motion related load are not a big issue for the George Washington Bridge. The chose was motivated also by the peculiarity of the bridge to have two decks. In fact, many researches have been done to study the aerodynamic performances of several trusses typology but not one for a double decked

bridge. It has been interesting to compare the results obtained for the two different version. From a mechanical point of view, the double decked version is of course more rigid. But is not immediate to assert the same for its aerodynamic behavior, in fact the aerodynamic static coefficients are smaller in the single decked version, so the forces induced by the wind are higher in the double decked one. Finally, the critical wind speed that induce the phenomenon of flutter, will depend on the complex interaction between the mechanical stiffness and the aerodynamic performance.



Figure 1.5: George Washington Bridge, double deck [6].

2. MOTION RELATED WIND LOADS

The problem of evaluating the loads acting on a moving body immersed in a low-speed flow is of great importance in many applications, ranging from aeronautics to mechanical and civil engineering. The case of the airfoil moving inside an inviscid flow was solved by Wagner [7] in 1925 and Theodorsen [8] in 1935 with different approaches, but under the same assumption of a zero-thick profile namely “thin airfoil” approached by the flow with a small angle of attack. The time-domain formulation based on the Wagner indicial functions and the mixed time-frequency formulation developed by Theodorsen were reorganized and further developed by many authors, revealing the main theoretical background needed to explain some complex fluid-structure interaction problem, such as the flutter instability.

Nevertheless, when unstreamlined body as typical bridge decks are considered, possible large flow separation, reattachment, recirculation zones and vortex shedding can occur, inducing significant unsteady effects and preventing to identify a thin and well defined boundary layer. Accordingly, the thin airfoil theory should not be used directly to predict the behavior of the so called “bluff bodies”.

In order to overcome this problem several theoretical and computational approaches have been developed, based on both frequency-domain and time-domain description. In bridge aerodynamics context, motion-induced loads are described by distinguishing in-phase and out-of-phase components with respect to the time evolution of the motion, instead of the distinction between circulatory and non-circulatory effects as for the thin airfoil [9]. Regarding frequency-domain approaches, Scanlan successfully exported some features of the Theodorsen results, describing the wind loads induced by sectional harmonic motions by means of a linearized format based on experimentally evaluated parameters namely “flutter derivatives”, that supplied the lack of closed- form analytical formulations.

For the synthesis of the concepts, the scheme adopted in [10] [11] has been followed. The first part of this chapter the problem of evaluating the loads acting on a moving body immersed in a low-speed flow is defined and the main results of the airfoil theory are recalled together with the main strategies currently used to extend their applicability to bluff bodies. In the last part a unified time-domain description is introduced and the analytical relationships between time and frequency-domain quantities are deduced. The aim is to introduce the simplified approach adopted in the following chapters for the calculation of flutter derivatives, and to clarify the nature of the simplifications on which it is based.

2.1. Problem setting and background

Consider a rigid cylindrical body with an infinite span length and an elongated cross section immersed in a low-speed wind flow orthogonal to the body axis. Denote with B the chord dimension, ρ the air density, and with U the mean wind velocity of the approaching flow. As shown in *Figure 2.1* the body has three degrees of freedom in the cross sectional plane corresponding to horizontal (p_d), vertical (h_d) and angular (α) displacements. Rotation is assumed to be about a chord point distant $aB/2$ from the midpoint of the chord. Moreover the angle of incidence $\hat{\alpha}$ between the wind direction and the cross-section chord defines the reference configuration of the body.

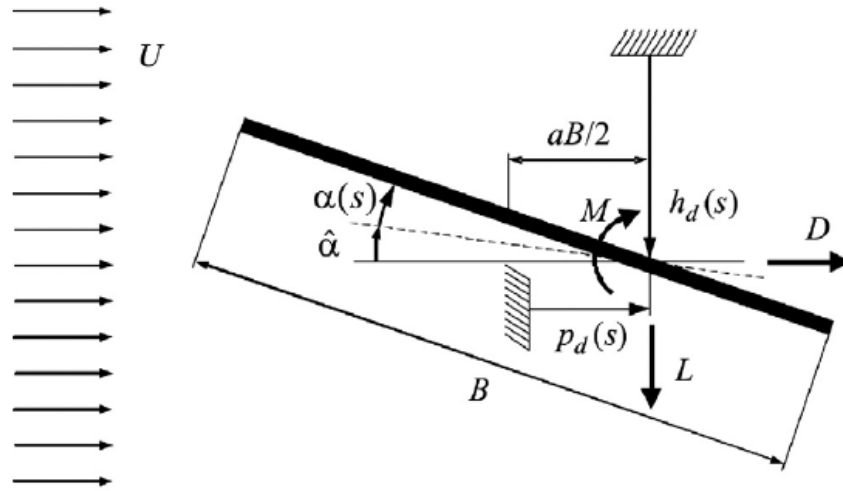


Figure 2.1: Sectional model [10].

The flow is assumed to be perfectly correlated along the span length and possible turbulence in the approaching flow is considered to be uncoupled in frequency with the turbulence initiated by the body itself. Accordingly, flow distribution can be regarded as two-dimensional in the sectional plane and the induced pressure distribution on the body can be reduced to the generalized force components illustrated in *Figure 2.1*:

$$\text{Drag: } D = \frac{1}{2} \rho U^2 B C_d \quad (2.1.1)$$

$$\text{Lift: } L = \frac{1}{2} \rho U^2 B C_l \quad (2.1.2)$$

$$\text{Pitching Moment: } M = \frac{1}{2} \rho U^2 B^2 C_m \quad (2.1.3)$$

Where C_d , C_l and C_m are the dimensionless force coefficients.

2.2. Thin airfoil

The thin airfoil is defined as a rigid flat plate with vanishing thickness, the problem related to the characterization of the aerodynamic forces acting on it while is supposed harmonically oscillating in a two-dimensional, incompressible and perfectly inviscid approaching flow, was solved by Theodorsen [8]. He defined the self-excited forces as the superposition of circulatory and non-circulatory contributions, the first depending on the frequency oscillations and accounting for flow unsteady effects and the second independent by frequency oscillations and including inertial effects due to the moved fluid mass. In dimensionless form they result in:

$$C_l^{nc}(s) = \frac{C_{l,\alpha}}{4}(\alpha' + h'' - \frac{a}{2}\alpha'') \quad (2.2.1)$$

$$C_m^{nc}(s) = -\frac{C_{m,\alpha}}{2(\frac{1}{2} + a)} \left[\frac{1}{2}(\frac{1}{2} - a)\alpha' + \frac{1}{4}(\frac{1}{8} + a^2)\alpha'' - \frac{a}{2}h'' \right] \quad (2.2.2)$$

$$C_l^c(k, s) = C_{l,\alpha}\tilde{C}(k) \left[\alpha + h' + \frac{1}{2}(\frac{1}{2} - a)\alpha' \right] \quad (2.2.3)$$

$$C_m^c(k, s) = C_{m,\alpha}\tilde{C}(k) \left[\alpha + h' + \frac{1}{2}(\frac{1}{2} - a)\alpha' \right] \quad (2.2.4)$$

Where $s = \frac{Ut}{B}$ is the dimensionless time, $k = \frac{B\omega}{U}$ is the reduced frequency, $C_{j,\alpha} = \frac{\partial C_j}{\partial \alpha}$ and f' denotes the first derivative of f with respect to s . The frequency-dependent function $C(k)$ is the Theodorsen's complex circulatory function defined by Hankel functions of the second kind [12] and it can be expressed by composing real and imaginary part as $\tilde{C}(k) = \tilde{F}(k) + i\tilde{G}(k)$, Figure 2.2 shows the variation of \tilde{F} and \tilde{G} under the reduced frequency.

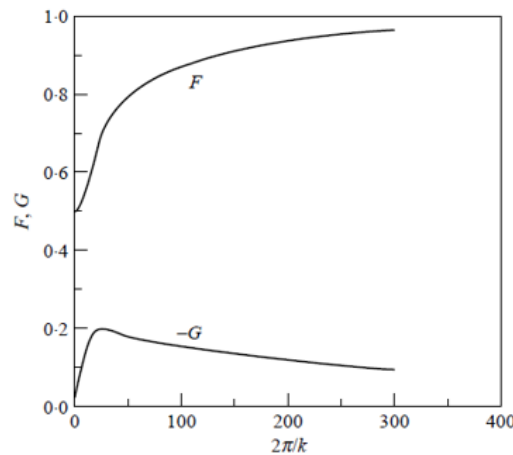


Figure 2.2: Real and Imaginary part of Theodorsen Function [11].

It must be noticed that circulatory contributions to lift and moment expressed in (2.2.4) and (2.2.3) are function of both time and frequency, so the approach proposed by Theodorsen could be considered in a mixed time-frequency domain.

By a different approach, Wagner [7] solved the problem of an abrupt change of the angle of attack from $\hat{\alpha} = 0$. He described the evolution of the lift force up to its static value by introducing an indicial lift-growth function $\phi(s)$ varying from 0.5 in initial step to 1 for s tending to infinity.

Introducing the downwash dimensionless velocity at the rear neutral point (the three-quarter chord point), on which the expressions (2.2.4) and (2.2.3) are based as:

$$w_{3/4}(s) = \alpha + h' + \frac{1}{2} \left(\frac{1}{2} - a \right) \alpha' \quad (2.2.5)$$

Due to the simplification at the basis of the thin airfoil theory, lift and moment induced by an arbitrary motion that involves also the vertical displacement h can be expressed both in function of the downwash function and the Wagner's indicial function. Invoking the superposition principle and assuming the airfoil moving from the rest at $s = 0$, circulatory terms in the time-domain can be expressed by the following Duhamel's convolution integrals [13]:

$$C_l^c(s) = C_{l,\alpha} \int_{-\infty}^s \phi(s - \sigma) w_{3/4}(\sigma) d\sigma = C_{l,\alpha} \left[\phi(0) w_{3/4}(s) + \int_0^s \phi'(\sigma) w_{3/4}(s - \sigma) d\sigma \right] \quad (2.2.6)$$

$$C_m^c(s) = C_{m,\alpha} \int_{-\infty}^s \phi(s - \sigma) w_{3/4}(\sigma) d\sigma = -\frac{1}{2} \left(\frac{1}{2} + a \right) C_l^c(s) \quad (2.2.7)$$

Where $\phi(s)$ is assumed to be 0 for $s < 0$.

By imposing a Fourier synthesis, a stronger duality was proven by Garrick [14] between time-domain and frequency-domain descriptions, resulting in the following relationships among the Theodorsen's function $\tilde{C}(k)$ and the Wagner's function $\phi(s)$:

$$\phi(s) = \frac{1}{2\pi i} \int_{-\infty}^{\infty} \frac{\tilde{C}(k)}{k} e^{iks} dk \quad (2.2.8)$$

$$\tilde{C}(k) = ik \int_0^{\infty} \phi(\sigma) e^{-ik\sigma} d\sigma \quad (2.2.9)$$

2.3. Bridge deck sections

The bridge deck sections present some differences with respect to the thin airfoil, for instances possible large flow separation, reattachment, recirculation zones and vortex shedding can occur, inducing significant unsteady effects and preventing to identify a thin and well defined boundary layer.

In order to overcome this problem several theoretical and computational approaches have been developed, based on both frequency-domain and time-domain description. In bridge aerodynamics context, motion-induced loads are described by distinguishing in-phase and out-of-phase components with respect to the time evolution of the motion, instead of the distinction between circulatory and non-circulatory effects as for the thin airfoil [9]. Regarding frequency-domain approaches, Scanlan successfully exported some features of the Theodorsen results, describing the wind loads induced by sectional harmonic motions by means of a linearized format based on experimentally evaluated parameters namely “flutter derivatives”, that supplied the lack of closed- form analytical formulations.

Time-domain approaches have not been developed as much as frequency-domain models, generally they are based on the definition of more indicial Wagner-like functions, but there are many difficulties due to the direct experimental evaluation of the response to an abrupt change of motion. Some attempts have been made by Scanlan and coworkers [15] [16] to combine Fourier synthesis and rational approximation techniques for analytically extracting the indicial functions from the experimentally derived flutter derivatives. Anyway the experimental derivation of flutter derivatives implicitly contains the non-circulatory contributions to the motion, so tightly they cannot be considered consistent with the Wagner theory that formally takes in to account the circulatory effects only.

The importance of pseudo non-circulatory contribution to the motion-related wind loads have been widely discussed, it can be considered problem dependent. For instances, it can be considered of secondary importance for a truss deck with whit large opening and grates [10].

2.3.1. Frequency-domain

In the context of the bridge aerodynamics, Scanlan [17] found an expression for lift and moment induced by small-amplitude harmonic motions linearly depending from the displacement parameters of the deck, in dimensionless form they can be expressed as:

$$C_l(s, k) = \widehat{C}_l + kH_1^*h' + kH_2^*\alpha' + k^2H_3^*\alpha + k^2H_4^*h \quad (2.3.1)$$

$$C_m(s, k) = \widehat{C}_m + kA_1^*h' + kA_2^*\alpha' + k^2A_3^*\alpha + k^2A_4^*h \quad (2.3.2)$$

Where \widehat{C}_l and \widehat{C}_m are the mean generalized dimensionless forces associated with $\hat{\alpha}$ defined in (2.1.1) and (2.1.2), and H_i^*, A_i^* ($i = 1 \dots 4$) are the flutter derivatives function of the reduced frequency k and the

mean angle of attack $\hat{\alpha}$. They naturally depend also on the section shape and actually the most reliable way to find it is to test scaled models in wind tunnel.

Considering an harmonic rotation $\alpha(s) = \alpha_0 e^{iks}$ about $\hat{\alpha}$, the dimensionless forces result in:

$$C_l(s, k) - \widehat{C}_l = k^2 (iH_2^* + H_3^*) \alpha_0 e^{iks} = H_{l\alpha}(k) \alpha(s) \quad (2.3.3)$$

$$C_m(s, k) - \widehat{C}_m = k^2 (iA_2^* + A_3^*) \alpha_0 e^{iks} = H_{m\alpha}(k) \alpha(s) \quad (2.3.4)$$

Where the square modulus of the complex functions $H_{l\alpha}$ and $H_{m\alpha}$ represent an aerodynamic frequency-response functions. Moreover, it is possible to express the forces themselves as harmonic in time with the reduced frequency k as $C_j(s, k) - \widehat{C}_j = C_j e^{i\psi_j}$ ($j = l, m$) being C_j the amplitude and ψ_j the phase shift with respect to the motion. Hence the previously equations became:

$$\frac{C_l e^{i\psi_l}}{\alpha_0} = H_{l\alpha}(k) \quad (2.3.5)$$

$$\frac{C_m e^{i\psi_m}}{\alpha_0} = H_{m\alpha}(k) \quad (2.3.6)$$

It is possible to obtain similar expressions involving the frequency-response functions $H_{jh}(k)$ by considering harmonic vertical motions $h(s) = h_0 e^{iks}$.

These formulations are fundamental to extract the flutter derivatives defining the Scanlan frequency-domain description with the forced vibration method [11].

2.3.2. Time-domain

The time domain approach developed by Wagner for the motion-induced load acting on the thin airfoil does not contain a description of the non-circulatory effects that should not be neglected in the analysis of mid-bluff body as bridge deck sections. A consistent time domain description it has been made considering the superposition of both circulatory and non-circulatory effects in the definition of the dimensionless aerodynamic loads [10]. It must be noticed that the distinction between the two effects cannot be rigorously made for the generic bridge deck sections, in the case of geometry with a moderate bluff aerodynamic response, a distinction can be postulated in terms of measurable effects between contributions depending or not on the motion history.

In the context of a time-domain description, non-circulatory loads are assumed linearly depending on the first and the second time derivatives of the displacement parameters:

$$C_j^{nc}(s) = C_{j\alpha} [I_{j\alpha 1} \alpha' + I_{j\alpha 2} \alpha'' + I_{jh 1} h' + I_{jh 2} h''] \quad (2.3.7)$$

Where the eight dimensionless quantities I_{jgi} ($j = l, m$; $g = \alpha, h$; $i = 1, 2$) are model parameters and $C_{j,\alpha} = \frac{\partial C_j}{\partial \alpha}$ as introduced previously.

The circulatory contributions are calculated by combining via convolution two indicial functions for each generalized force with downwash terms. The downwash terms are assumed to be different for each force and for each displacement component. Accordingly, circulatory terms are expressed as:

$$C_j^c(s) = C_{j\alpha} \int_{-\infty}^s [\phi_{j\alpha}(s - \sigma) w_{j\alpha}(\sigma) + \phi_{jh}(s - \sigma) w_{jh}(\sigma)] d\sigma \quad (2.3.8)$$

Where the downwash functions are:

$$w_{j\alpha}(s) = D_{j\alpha 0} \alpha(s) + D_{j\alpha 1} \alpha'(s) \quad (2.3.9)$$

$$w_{jh}(s) = D_{jh 0} h(s) + D_{jh 1} h'(s) \quad (2.3.10)$$

The eight dimensionless quantities D_{jgi} ($j = l, m$; $g = \alpha, h$; $i = 0, 1$) are model parameters and $\phi_{jg}(s)$ are proper Wagner-like indicial functions describing the transient aerodynamic response when a step-wise change in the downwash function $w_{jg}(s)$ from zero to the final value \hat{w}_{jg} occurs at $s = 0$.

2.3.3. Time-frequency duality

As seen previously for the thin airfoil, the Fourier transformation allows to find analytical relationship between time-domain and frequency-domain descriptions. By equating the Fourier transformations of self-excited loads defined by Scanlan in (2.3.1) and (2.3.2) to the time-domain equations (2.3.7) and (2.3.8), the following complex relationships hold:

$$C_{j\alpha} [ik I_{jg 1} - k^2 I_{jg 2} + \tilde{C}_{jg}(k)(D_{jg 0} + ik D_{jg 1})] = H_{jg}(k) \quad (2.3.11)$$

Where $j = l, m$ and $g = \alpha, h$, the frequency-response functions are defined as in (2.3.3) and (2.3.4), and \tilde{C}_{jg} are the four Theodorsen-like functions:

$$\tilde{C}_{jg}(k) = \tilde{F}_{jg}(k) + i\tilde{G}_{jg}(k) = ik \int_0^{\infty} \phi_{jg}(\sigma) e^{-ik\sigma} d\sigma = \phi_{jg}^0 + \bar{\phi}_{jg}(k) \quad (2.3.12)$$

So that:

$$\phi_{jg}(s) = \frac{1}{2\pi i} \int_{-\infty}^{\infty} \frac{\tilde{C}_{jg}(k)}{k} e^{iks} dk = \frac{2}{\pi} \int_0^{\infty} \frac{\tilde{F}_{jg}(k)}{k} \sin(ks) dk \quad (2.3.13)$$

Where $\phi_{jg}^0 = \phi_{jg}(0)$ and the frequency dependent quantity $\bar{f}(k) = \int_{-\infty}^{\infty} f(s) e^{-iks} ds$ denotes the Fourier transform of the time-dependent function $f(s)$. Collecting real and imaginary contributions in equation (2.4.1) the following frequency-based equations are obtained:

$$k^2 H_1^*(k) = C_{l,\alpha} [kI_{lh1} + \tilde{G}_{lh}(k)D_{lh0} + k\tilde{F}_{lh}(k)D_{lh1}] \quad (2.3.14)$$

$$k^2 H_2^*(k) = C_{l,\alpha} [kI_{l\alpha1} + \tilde{G}_{l\alpha}(k)D_{l\alpha0} + k\tilde{F}_{l\alpha}(k)D_{l\alpha1}] \quad (2.3.15)$$

$$k^2 H_3^*(k) = C_{l,\alpha} [-k^2 I_{l\alpha2} + \tilde{F}_{l\alpha}(k)D_{l\alpha0} - k\tilde{G}_{l\alpha}(k)D_{l\alpha1}] \quad (2.3.16)$$

$$k^2 H_4^*(k) = C_{l,\alpha} [-k^2 I_{lh2} + \tilde{F}_{lh}(k)D_{lh0} - k\tilde{G}_{lh}(k)D_{lh1}] \quad (2.3.17)$$

$$k^2 A_1^*(k) = C_{m,\alpha} [kI_{mh1} + \tilde{G}_{mh}(k)D_{mh0} + k\tilde{F}_{mh}(k)D_{mh1}] \quad (2.3.18)$$

$$k^2 A_2^*(k) = C_{m,\alpha} [kI_{m\alpha1} + \tilde{G}_{m\alpha}(k)D_{m\alpha0} + k\tilde{F}_{m\alpha}(k)D_{m\alpha1}] \quad (2.3.19)$$

$$k^2 A_3^*(k) = C_{m,\alpha} [-k^2 I_{m\alpha2} + \tilde{F}_{m\alpha}(k)D_{m\alpha0} - k\tilde{G}_{m\alpha}(k)D_{m\alpha1}] \quad (2.3.20)$$

$$k^2 A_4^*(k) = C_{m,\alpha} [-k^2 I_{mh2} + \tilde{F}_{mh}(k)D_{mh0} - k\tilde{G}_{mh}(k)D_{mh1}] \quad (2.3.21)$$

These equations represent a closed-form relationship between flutter derivatives and Theodorsen-like circulatory functions.

2.4. A simplified approach for flutter derivatives

The direct application of equations (2.3.14) - (2.3.21) for calculating the flutter derivatives of bridge decks is not easy to be made, the relationships are function of the sixteen parameters introduced that should be estimated via experimental or difficult numerical approaches. In this section a simplified approach is proposed, it is based on the theoretical estimation of the sixteen parameters previously introduced for the thin airfoil; the flutter derivatives will be expressed as functions of real and imaginary component of the Theodorsen function, and of the aerodynamic pressure coefficient of a generic bridge deck. In the case of the thin airfoil and considering $\hat{\alpha} = 0$ the four indicial functions introduced in (2.3.8) reduce to the Wagner function and analogously the Theodorsen-like in (2.3.11) and (2.3.12) reduce to the well-known Theodorsen function. Moreover, the sixteen parameters result in:

$$I_{l\alpha 1} = \frac{1}{4} ; I_{l\alpha 2} = -\frac{a}{8} ; I_{lh1} = I_{mh1} = 0 ; I_{lh2} = \frac{1}{4} \quad (2.4.1)$$

$$I_{m\alpha 1} = -\frac{1}{4} \frac{\left(\frac{1}{2} - a\right)}{\left(\frac{1}{2} + a\right)} ; I_{m\alpha 2} = -\frac{1}{8} \frac{\left(\frac{1}{8} + a^2\right)}{\left(\frac{1}{2} + a\right)} ; I_{mh2} = \frac{a}{4\left(\frac{1}{2} + a\right)} \quad (2.4.2)$$

$$D_{j\alpha 0} = D_{jh1} = 1 ; D_{j\alpha 1} = \frac{1}{2} \left(\frac{1}{2} - a\right) ; D_{jh0} = 0 \quad (j = l, m) \quad (2.4.3)$$

Accordingly, relationships (2.3.14) – (2.3.21) reduce to:

$$kH_1^\#(k) = -C_{l,\alpha} \tilde{F}(k) \quad (2.4.4)$$

$$kH_2^\#(k) = C_{l,\alpha} \left[\left(\frac{1}{4} - a\right) \tilde{F}(k) + \frac{\tilde{G}(k)}{k} \right] + \frac{C_{l,\alpha}}{4} \quad (2.4.5)$$

$$k^2 H_3^\#(k) = C_{l,\alpha} \left[\tilde{F}(k) - k\tilde{G}(k) \left(\frac{1}{4} - a\right) \right] + C_{l,\alpha} k^2 \frac{a}{4} \quad (2.4.6)$$

$$k^2 H_4^\#(k) = C_{l,\alpha} k\tilde{G}(k) + \frac{C_{l,\alpha} k^2}{4} \quad (2.4.7)$$

$$kA_1^\#(k) = -C_{m,\alpha} \tilde{F}(k) \quad (2.4.8)$$

$$kA_2^\#(k) = C_{m,\alpha} \left[\left(\frac{1}{4} - a\right) \tilde{F}(k) + \frac{\tilde{G}(k)}{k} \right] + \frac{C_{l,\alpha}}{4} \left(a - \frac{1}{4}\right) \quad (2.4.9)$$

$$k^2 A_3^\#(k) = C_{m,\alpha} \left[\tilde{F}(k) - k\tilde{G}(k) \left(\frac{1}{4} - a\right) \right] + C_{l,\alpha} k^2 \frac{a}{4} + \frac{C_{l,\alpha} k^2}{128} \quad (2.4.10)$$

$$k^2 A_4^\#(k) = -C_{m,\alpha} k\tilde{G}(k) - C_{l,\alpha} k^2 \frac{a}{4} \quad (2.4.11)$$

Where $A_i^\#(k)$ and $H_i^\#(k)$ are the flutter derivatives for thin airfoil as expressed by Fung [13] [18].

3. CFD FOR THE EVALUATION OF AERODYNAMIC COEFFICIENTS

The formulas developed in the last chapter for the calculation of flutter derivatives are based on some aerodynamic parameters: the derivatives of lift and moment coefficients with respect to the angle of attack. The so called pressure coefficients have been introduced in (2.1.1), (2.1.2), they characterize the distribution of pressure due to a wind flow approaching with an angle of incidence so the interaction between the structure and the wind must be evaluated. The interaction between a turbulent flow and a rigid body is theoretically explained by the *Navier-Stokes* equations that generically describe the motion of viscous fluid substances. Currently, there are no analytical solution in closed form for this set of equations so several numerical methods have been developed in order to provide approximate solutions to the problem. The *Computational Fluid Dynamics (CFD)* is a branch of fluid mechanics that uses numerical methods to analyze and solve problems that involve fluid flows. Computers are used to perform the calculations required to simulate the free-stream flow of the fluid, and the interaction of the fluid with surfaces defined by boundary conditions (*Figure 3.1*). The *Computational Fluid Dynamics* is a very complex branch, in this chapter will only be shortly introduced the main features that will be used in the simulations presented in the second part, and some examples of application will be reported and taken as a benchmark for the results obtained.

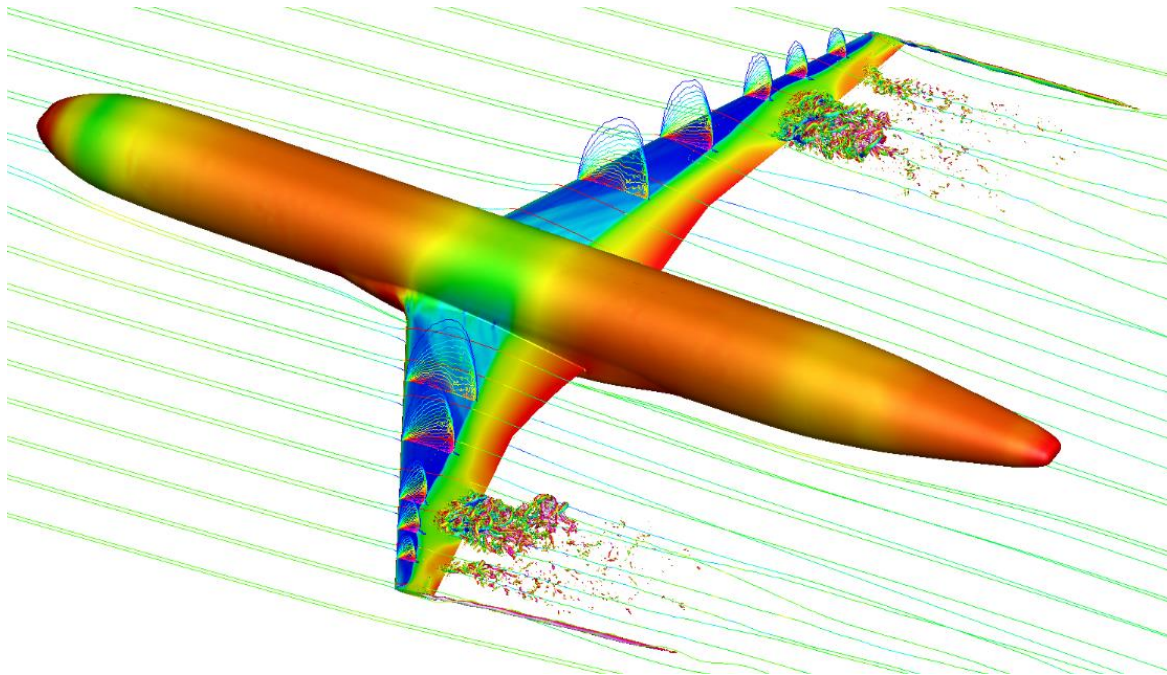


Figure 3.1: Aircraft in a fluid flow [19]

3.1. Overview on turbulence modeling

In the literature, a considerable amount of theoretical work can be found dealing with different methods adopted to take into account turbulence in fluid-structure-interaction (*FSI*) problems, spanning from laminar simulation to large eddy simulation (LES) with increasing level of physical insight, mathematical complexity and computational cost (*Figure 3.2*).

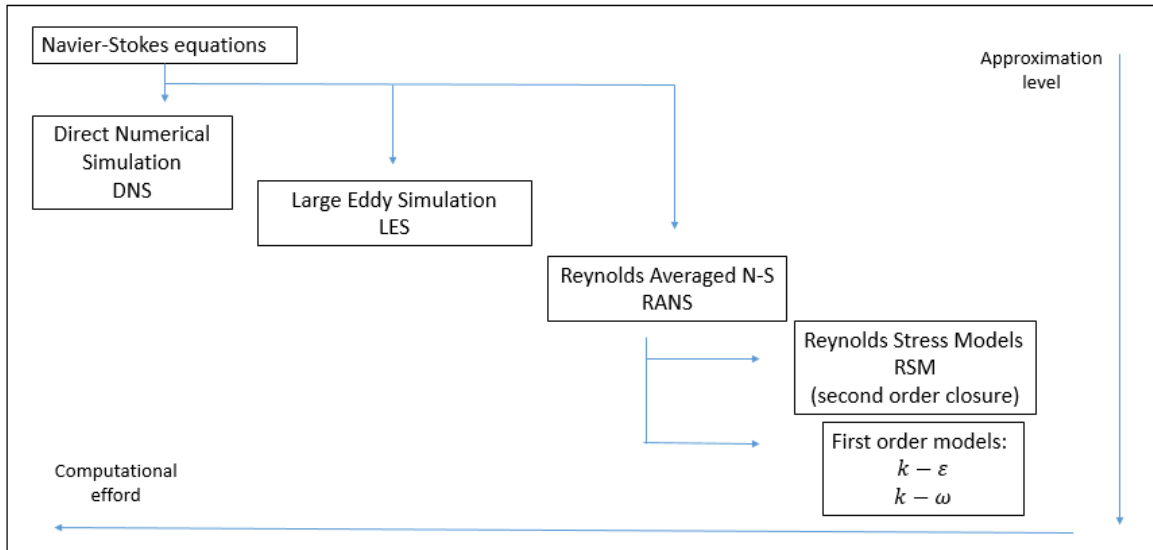


Figure 3.2: Numerical approaches for turbulence modeling [20].

The laminar approach is not even mentioned because it gives a physical representation of the flow only at very low Reynolds numbers that typically do not characterize the wind in the atmosphere. At higher Reynolds numbers inertial forces prevail and the flow field is characterized by random fluctuations whose time and length scales are smaller than the mean flow ones. The direct simulations of the turbulence flow (DNS) is rarely adopted because involves an enormous computational cost. However, it is generally accepted that the mean flow characteristics have small influence on the fluctuations developed by turbulence at several order of magnitude difference. Accordingly, a statistical approach is often used in order to take into account the small scale effects on the mean flow without directly simulating them. The most common approach currently used is the *RANS* (Reynolds-averaged Navier-Stokes), it is based on the time averaging of the Navier–Stokes equations and allows to model a turbulent flow with an acceptable computational cost [21]. Another approach, as shown in *Figure 3.2*, more sophisticated than RANS is LES (Large Eddy Simulation) [22] [23]. It is based on space-averaging rather than time-averaging adopted in RANS. As the DNS, LES use is limited because of its high computational cost that can reach $10^5 - 10^6$ times the one required by RANS [24]. In *Figure 3.3* a qualitative difference between the different approaches to simulate the turbulence is illustrated with respect to the experimental one [25]. It is

possible to notice that the time-averaging operating in RANS simulations is not able to model the details resulting from high frequency fluctuations and, therefore, these use to be modeled by a turbulence model.

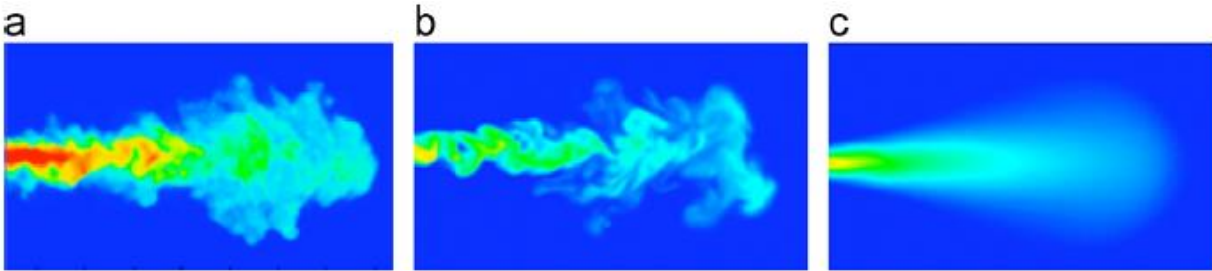


Figure 3.3: Comparison between experimental (a), LES (b) and RANS (c) turbulent structures [25].

Currently, there are a lot of turbulence models developed for RANS simulations, the most commonly used are the two equations $k - \varepsilon$ and $k - \omega$ [26] [27] models. The theoretical background of these models will not be developed in this work of thesis; they allow to model the turbulence by only two parameters and two additional equations are introduced. Their relatively low computational cost makes them suitable for industrial applications, moreover, they are the simplest turbulence models that can be considered general, in the sense that their parameters are not strongly problem-dependent. The main difference between the two equations models lies in the near wall flow solution and it is summarized in [21] as follow: the $k - \varepsilon$ model does not allow the direct integration through the boundary layer because ε becomes zero close to the wall. Otherwise, the $k - \omega$ model allows to direct integrate through the boundary layer, so permits to improve the wall boundary layer unsteady solution as demonstrated in [27]. As a drawback, the $k - \omega$ model has proved to be highly sensitive to inlet turbulence boundary conditions that can sensibly affect the solution even in large computational domain [28]. Another interesting possibility is offered by the $k - \omega SST$ model developed by Menter et al in [28]. It consists in a sort of combination between the $k - \varepsilon$ and $k - \omega$ models whose weighting is controlled by the wall distance. It preserves the main advantages of the classical $k - \omega$ model but it has been proved to be less sensible to the variation of inlet conditions.

3.2. Aerodynamic analysis of Great Belt East

The RANS approach to simulate the motion of a turbulent flow approaching against a bluff body is the most commonly used because of its relatively low computational cost. In this section the cross-section of the Great Belt Est Bridge (*Figure 3.4*) has been reported as a case study [21]. The results obtained have been compared with the ones obtained experimentally by wind tunnel tests performed on a scaled model (1:80) at the Danish Maritime institute by Reinhold et al [29]. No accessory structures are modeled, because of their small dimension and high porosity their influence on the global aerodynamic behavior can be neglected.

The model consists in a scaled bridge cross-section of length B (Figure 3.5) immersed into a computational domain having dimension of $12B$ in the direction parallel to the wind flow and $5.5B$ in the transversal direction.



Figure 3.4: View of the Great Belt East Bridge [21].

The computational analysis in the article is subdivided in two stages named steady and dynamic, the first is aimed to the determination of the pressure coefficients while the second to the determination of the flutter derivatives. Only the stationary analysis has been reported in this work in order to make a comparison with the results obtained in section 6.1.

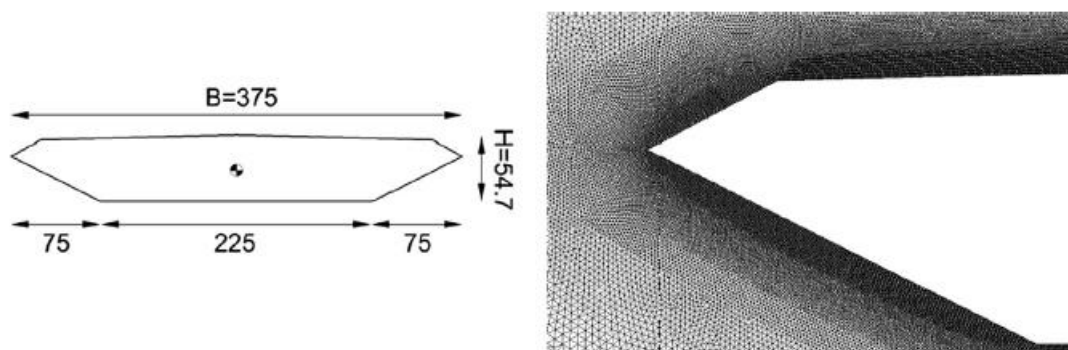


Figure 3.5: Cross-section (scale 1:80, dimension in mm) and the adopted mesh structure [12].

Generally, bridge decks cross-sections aerodynamic behavior is not strongly influenced by Reynolds number, accordingly, the meshing procedure has been performed by the authors as follows. In the region adjacent to the cross-section a structured mesh is built with cell size in the order of $B * 10^{-3}$, then, the computational grid is slowly coarsened and characterized by an unstructured mesh until a maximum size of the order of $B * 10^{-1}$. Moreover, in order to capture the vortex shedding instability, a particular care to well represent the fluid volume close to the trailing edge and the vortex street has been taken: for a distance not smaller than $4B$ the mesh size has been imposed not bigger than $B * 10^{-2}$. Finally, as a boundary conditions a velocity input and a pressure outlet regions have been created with a turbulent intensity of 0.5% according to standard wind tunnel conditions for laminar flow, and a turbulent viscosity ratio equal to 2 seeking to provide a good agreement with the static coefficients at 0° .

The pressure coefficients of the bridge deck are evaluated for five different values of the incidence angle: 0° ; $\pm 5^\circ$; $\pm 10^\circ$. The comparison between experiments and computations reveals that the proposed simulation methodology is able to predict the static bridge aerodynamic behavior for all the considered configurations (Figure 3.6).

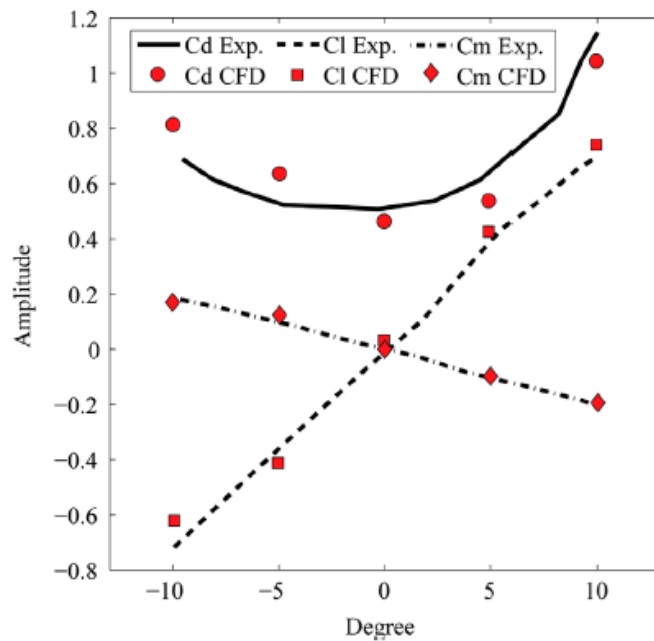


Figure 3.6: Variation of the pressure coefficients with the angle of incidence [21].

Highly relevant for the present work are the aerodynamics coefficient slopes because the previously introduced (2.4.4) and (2.4.11) are strictly dependent on them, their values are reported in Table 3.1.

Exp. $C_{L,\alpha}$	Num. $C_{L,\alpha}$	Exp. $C_{M,\alpha}$	Num. $C_{M,\alpha}$
4.13	4.09	-1.12	-1.08

Table 3-1: Experimental and numerical aerodynamic coefficients slope [21].

3.3. Aerodynamic performance of a steel truss stiffening girder

The previous section shows how the aerodynamic behavior of a streamlined bridge deck cross-section can be reliably reproduced by a RANS simulation of a two-dimensional model. It is not immediate to extend the reliability of a two-dimensional model from a streamlined section to steel truss girder, the last in fact is characterized by an unsteady envelop of the cross-section through the longitudinal direction of the bridge. This section reports an article [30] where the aerodynamic behavior of a typical truss stiffened girder is represented with a bi-dimensional CFD model with the aim of compare several different aerodynamic countermeasures to find an optimization scheme for improvement of the bridge flutter stability. It is worth to notice that the aim of this work is different, in the framework of the thesis this article has been taken as an example of how the aerodynamic behavior of a truss can be successfully modelled by a two-dimensional CFD model.

A suspension bridge with steel truss stiffening girder and a middle span of 1100 meters located in the dry-hot river valley whit deep canyon area is selected to carry out the analysis. The cross-section is characterized by a width of 27 meters and an eight is 8.2 meters (*Figure 3.7*).

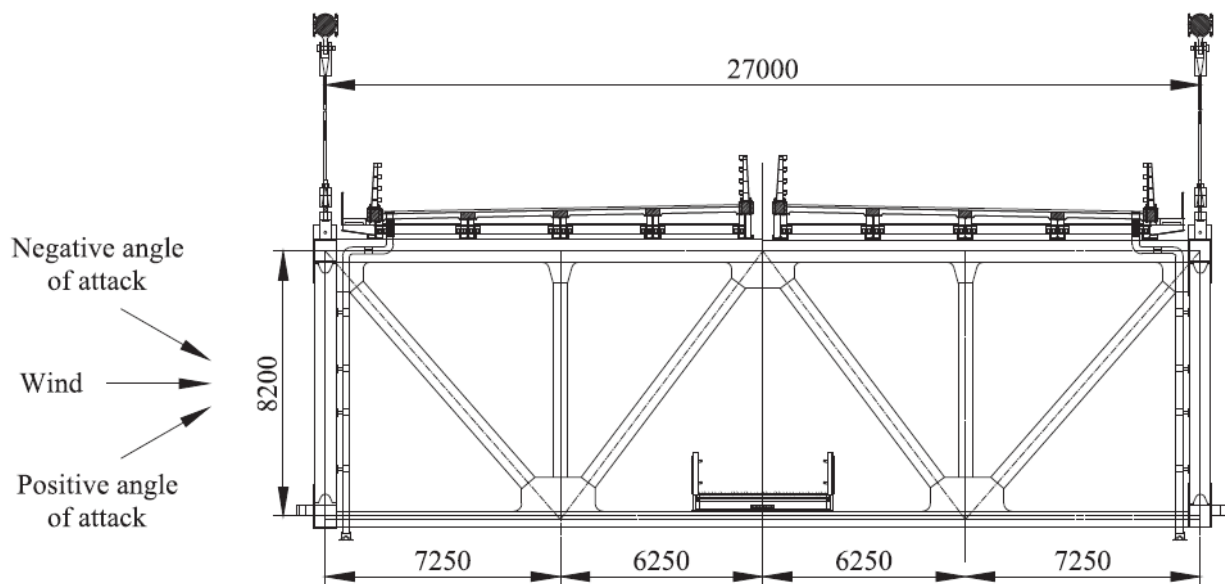


Figure 3.7: outline of the steel truss stiffening girder (in millimeters) [30].

The 2D simplified model has a scale ratio equal to $1/43.6$ which is the same value adopted in wind tunnel tests taken as comparison, and the computational mesh is shown in *Figure 3.8*. The computational domain is imposed to be $6.5 * B$ in the flow direction and $4 * B$ in the transversal direction, where B is the model width of the bridge deck; the model is placed on a distance from the inlet boundary of $2B$. As it shown in *Figure 3.8*, the computational domain is also divided in three parts meshed differently: the rigid mesh

zone is discretized by a quadrilateral unstructured grid, the dynamic mesh zone by triangular unstructured grid and the fixed mesh zone by a quadrilateral structured mesh.

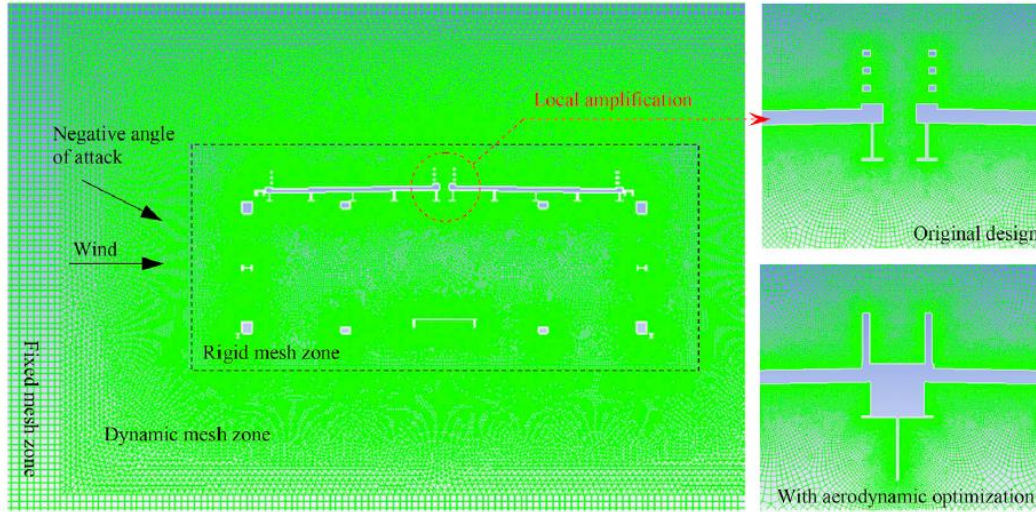


Figure 3.8: Local computational mesh of the 2D model [30].

Finally, RANS simulations are performed by using the $k-\omega$ SST model, as for the previous section, in order to estimate the flutter derivatives of the bridge. Next, several flutter analyses have been performed to obtain the flutter velocities and frequencies with and without aerodynamic countermeasures under different values of angle attack. The results are summarized and compared with the ones obtained by wind tunnel tests in *Table 3.2*.

Vibration direction		Angle of attack			
		-7°	-5°	-3°	0°
Velocity (m/s)					
Original design	Wind tunnel test	37.7	42.1	42.5	50.5
	CFD simulation	32.5	38.5	43.5	61.5
With aerodynamic countermeasures	Wind tunnel test	50.2	64.5	82.4	>90
	CFD simulation	42.5	60.5	82.0	88.0
Frequency (Hz) by CFD simulation					
Original design		0.319	0.315	0.314	0.308
With aerodynamic countermeasures		0.314	0.305	0.289	0.279

Table 3-2: Flutter conditions of the suspension bridge [30].

4. FLUTTER OF LONG SPAN BRIDGES

The history of long span suspension bridges had been characterized by the ever increasing awareness that the wind load represents one of principal challenge to be addressed during the design phase. The first suspension bridge destroyed by the wind was the *Menai Bridge*, designed by the English engineer Telford in 1826, it had a 176 main span that connected Anglesey land and England. Even in Europe and USA in 19th century several bridges fell down under wind action, in fact no analysis regarding this load was done before the bridge construction until the middle of 20th century. As mentioned in the first chapter, thanks to the improvement of the design methods, the bridges were realized with an increasing slenderness and the ratio between the height of deck and main span length became smaller. An important example of this trend is the *Golden Gate Bridge* in San Francisco (*Figure 4.1*), it was built in 1937 and it has been the longest span bridge in the world until 1964 when the *Verrazano Narrows Bridge* was erected. The *Golden Gate* few times presented fluctuations under wind action of 3 meters in horizontal plane.



Figure 4.1: View of the Golden Gate Bridge [31].

A structure with a more important slenderness was the *Tacoma Narrows Bridge*, with a main span of 853 meters, it was characterized by an insufficient stiffness to counteract wind dynamic actions and as mentioned in the introduction it fell down under a recorded wind speed of 18.8 m/s. After this disaster, the researchers decided to focus on the studies of the bridge aerodynamics and the analyses in aircraft wings were used for big span bridges to evaluate the effect of the wind load on the decks. To the current state of the art, the most dangerous phenomenon in suspension bridge is flutter, the effect of the interaction between unsteady forces produced by moving structure and its fluctuation.

4.1. Dynamic instability

The aeroelastic instability plays an important role in long span suspension bridge design. The aeroelastic instability caused by the so called “classical flutter” is characterized by the matching of two modes of fluctuation with a similar deformed shape, generally the interaction concerns flexural and torsional modes. The wind action provides energy to the system and brings frequencies closer together until the two fluctuations are timed on the same frequency. Bridge flutter can also involve a single mode, usually the torsional one.

Wind effects on decks are correctly evaluated with time domain analysis, using nonlinear numerical models defining appropriate wind stories and experimental test on scaled models in wind tunnel. Currently the most reliable tests are those conducted in wind tunnel, but theoretical models are very important for predicting at least the order of magnitude of wind speed through which the instability may occur.

The most common theoretical models consist on analysis in frequency domain based on a linearization of the phenomenon with the introduction of stiffness and damping coefficients obtained experimentally.

Assuming an elastic behavior of the structure with a sinusoidal exponentially damped response and the transition between stable and unstable configuration in condition of oscillatory motion about equilibrium configuration on average wind condition, it is possible to represent the dynamic problem, in linearized form, with this equation:

$$[M] * \ddot{\delta}(T) + [\bar{K}] * \delta(T) = 0 \quad (4.1.1)$$

Where δ , $[M]$, and $[\bar{K}]$ are the time depending displacement vector, the mass matrix and the tangent stiffness matrix, respectively. The matrix $[\bar{K}]$ includes the effect of loading. If the latter is non-conservative, $[\bar{K}]$ is non-symmetric, and dynamic instability can occur, depending on the loading level.

The necessity of performing a stability linear analysis led to consider harmonic time disturbances, because dynamic response of the structure could be divided in a series of harmonic contributions with a Fourier transformation. Hence it is assigned an harmonic disturbance $\delta(t) = \delta_0 * e^{i\omega t}$, where δ_0 is the initial displacement. The system of differential equations (4.1.1) has trivial modes as solution except for modes with ω pulsation that satisfy characteristic equation:

$$([\bar{K}] - \omega^2[M]) * \{\delta\} = \{0\} \quad (4.1.2)$$

It is possible to obtain eigenvalue $\omega_j (j = 1, 2 \dots n \text{ d. o. f.})$ as a function of a loading parameter λ , the equilibrium can become unstable in correspondence of the critical value λ_c .

Finally searching for the solution in the form mentioned above and assuming the eigenvalues composed by real and imaginary part: $\omega_j = (\omega_r + i\omega_i)_j$. It is possible to attribute the onset of the instability to the sign of the imaginary part of the eigenvalue ω_j .

Being:

$$\{\delta_j\} = \{\delta_{0,j}\} * e^{i\omega_{rj}t} * e^{-\omega_{ij}t} \quad (4.1.3)$$

- If $\omega_{ij} > 0$ for each eigenvalue, equilibrium is stable;
- If $\omega_{ij} = 0$ at least for one eigenvalue, equilibrium is metastable;
- If $\omega_{ij} < 0$ at least for one eigenvalue, equilibrium is unstable.

Dynamic instability (flutter)

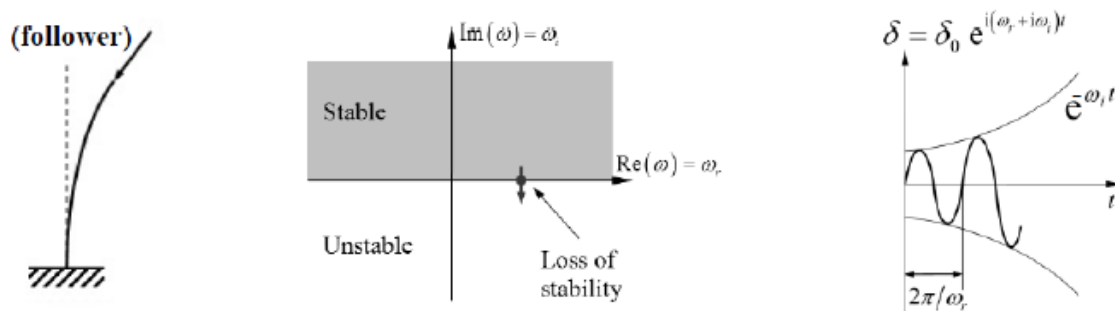


Figure 4.2: Representation of dynamic instability [32].

4.2. Two degrees of freedom flutter

After several studies, the researchers discovered the possibility to take advantages of the analysis developed in aeronautic field for the definition of the load acting on the wings of aircrafts, and adapt some models to the sections of suspension bridges deck to perform aeroelastic stability analysis. In *Figure 4.3* is reported a definition of the so called self-excited forces acting on a deck transversal section subjected to a constant wind flow U , in this simplified model the only two components of the displacement taken in to account are the vertical displacement h and the torsional rotation α .

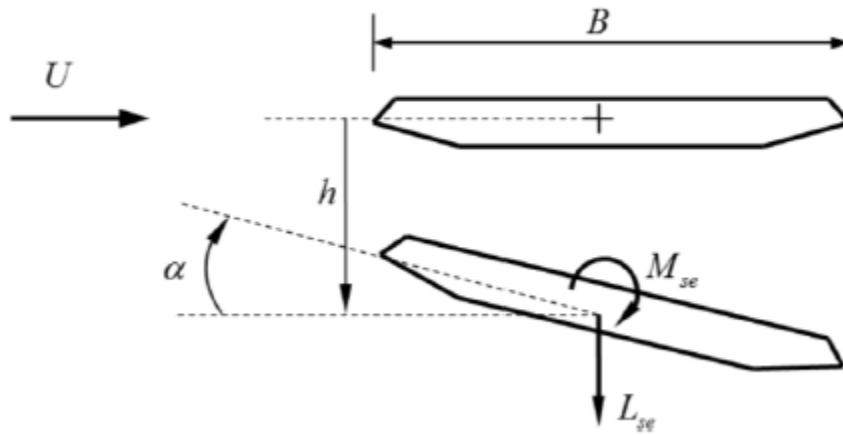


Figure 4.3: Two degrees of freedom simplified model.

Scanlan and Tomko developed an expression of self-excited forces, valid in small fluctuation field, where the wind load is linearly related to the motion coordinates of the bridge deck by means of the so called *Flutter derivatives*. This formulation is currently the most used for the flutter analysis of bridge decks and is the following:

$$L_{SE} = \frac{1}{2} \rho U^2 B \left[KH_1^*(K) \frac{\dot{h}(t)}{U} + KH_2^*(K) \frac{B \dot{\alpha}(t)}{U} + K^2 H_3^*(K) \alpha(t) + K^2 H_4^*(K) \frac{h(t)}{B} \right] \quad (4.2.1)$$

$$M_{SE} = \frac{1}{2} \rho U^2 B^2 \left[KA_1^*(K) \frac{\dot{h}(t)}{U} + KA_2^*(K) \frac{B \dot{\alpha}(t)}{U} + K^2 A_3^*(K) \alpha(t) + K^2 A_4^*(K) \frac{h(t)}{B} \right] \quad (4.2.2)$$

Where t is the time, $K = \frac{\omega B}{U}$ is the circular reduced frequency and $H_i^*(K), A_i^*(K)$ are the flutter derivatives.

Nowadays the most reliable methods for the calculation of flutter derivatives are based on experimental analysis on scale models in the wind tunnel, in *Figure 4.4* are shown some examples of flutter derivatives plotted in function of the reduced velocity U/fB .

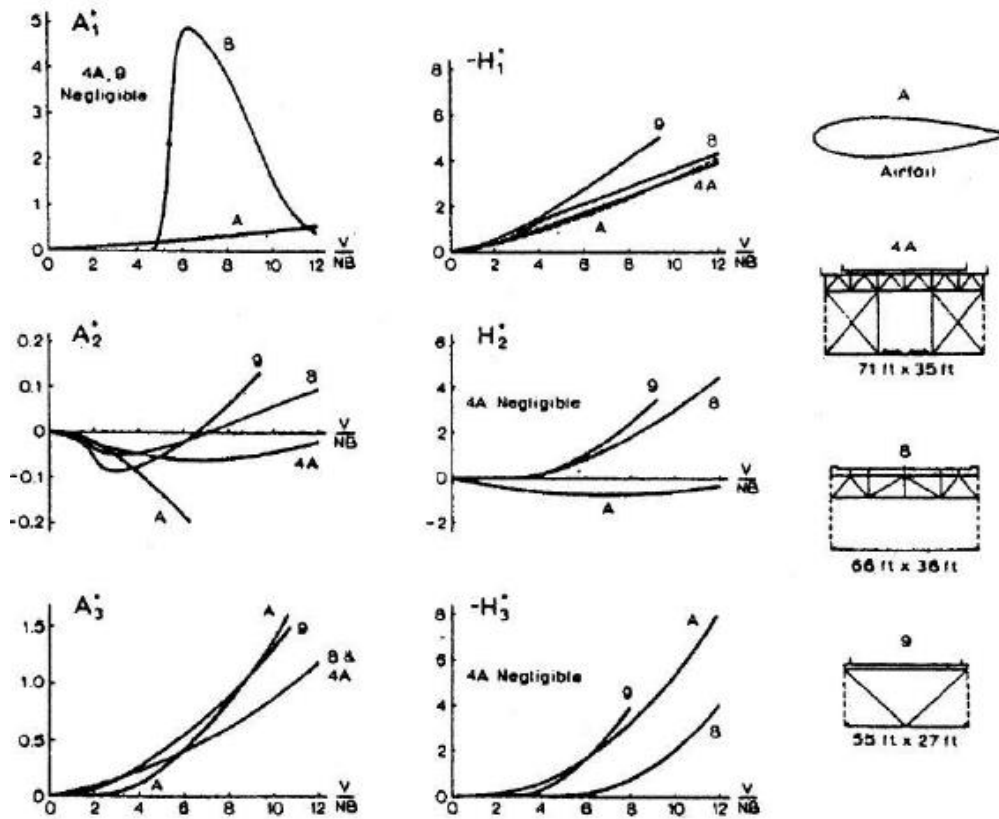


Figure 4.4: Examples of flutter derivatives [17].

Classic formulation for flutter analysis starts from the assumption that the interaction between wind and structure can be evaluated considering a bi-dimensional model representing the deck cross section, so tridimensional effects are negligible. Another simplification, that lose its validity for longest span bridges, is to neglect section motion in wind direction. So considering as only degrees of freedom the vertical displacement h and the torsional angle α of the deck (*Figure 4.3*) the equations of motion can be expressed in these forms:

$$m\ddot{h}(t) + c_h\dot{h}(t) + k_h h(t) = L_{SE}(t, K) \quad (4.2.3)$$

$$I\ddot{\alpha}(t) + c_\alpha\dot{\alpha}(t) + k_\alpha\alpha(t) = M_{SE}(t, K) \quad (4.2.4)$$

Where m and I represent the mass and the polar moment of inertia of the system per unit length, and c_i, k_i are the mechanic damping and elastic stiffness factors, respectively.

Searching solution in the harmonic form:

$$h(t) = h_0 e^{i\omega t} ; \alpha(t) = \alpha_0 e^{i\omega t} \quad (4.2.5)$$

By separating the real and imaginary parts, two equations of the 4th and 5th order in K are obtained. The common solution gives the reduced frequency K_F to which the flutter frequency ω_F is associated.

So the flutter instability speed can be obtained as:

$$U_F = \frac{B\omega_F}{K_F} \quad (4.2.6)$$

Alternatively, it is possible to define the eigenvalues of the system as a composition of real and imaginary part : $\omega_j = (\omega_r + i\omega_i)_j$. So the onset of flutter condition could be found by increasing the wind velocity until the imaginary part of at least one eigenvalue becomes negative. This method is focused in *section 4.4* with some differences related to the different form of the eigenvectors.

4.3. Three degrees of freedom flutter

Increasing the diffusion of the suspension bridges as a construction technology, the problem of the dynamic instability caused by the wind has become increasingly relevant and new analytic models have been developed. The representation of the bridge deck response with only two degrees of freedom is very affordable, it has spread widely over the years leading to excellent results. But increasing the length of the mid span and developing increasingly deformable structures, it has been noticed that the influence of the self-excited load in the direction of wind cannot be neglected. Several studies have been made to estimate the influence of the motion-induced Drag on the critical wind speed. More precisely, it has been discovered that it starts to become significant for suspension bridges having a mid-span longer than 1.5 kilometers.

The three degrees of freedom of the bridge deck cross-section are the vertical displacement, the torsional rotation and the horizontal displacement, to which correspond the aero-elastic forces reported in *Figure 4.5*.

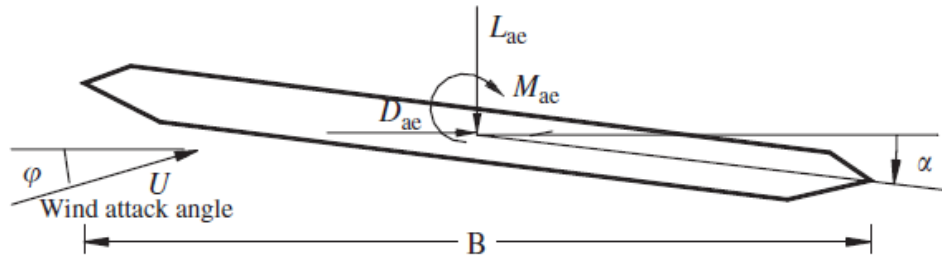


Figure 4.5: Three degrees of freedom sectional model [33].

Considering the additional horizontal degree of freedom, the expression of the self-excited (4.2.1), (4.1.2) forces is modified as follow:

$$L_{SE} = \frac{1}{2} \rho U^2 (2B) \left[KH_1^* \frac{\dot{h}}{U} + KH_2^* \frac{B \dot{\alpha}}{U} + K^2 H_3^* \alpha + K^2 H_4^* \frac{h}{B} + KH_5^* \frac{\dot{p}}{U} + K^2 H_6^* \frac{p}{B} \right] \quad (4.3.1)$$

$$D_{SE} = \frac{1}{2} \rho U^2 (2B) \left[KP_1^* \frac{\dot{p}}{U} + KP_2^* \frac{B \dot{\alpha}}{U} + K^2 P_3^* \alpha + K^2 P_4^* \frac{p}{B} + KP_5^* \frac{\dot{h}}{U} + K^2 P_6^* \frac{h}{B} \right] \quad (4.3.2)$$

$$M_{SE} = \frac{1}{2} \rho U^2 (2B^2) \left[KA_1^* \frac{\dot{h}}{U} + KA_2^* \frac{B \dot{\alpha}}{U} + K^2 A_3^* \alpha + K^2 A_4^* \frac{h}{B} + KA_5^* \frac{\dot{p}}{U} + K^2 A_6^* \frac{p}{B} \right] \quad (4.3.3)$$

4.4. Flutter analysis using ANSYS

The coupled flutter analysis, using the measured flutter derivatives from the spring-mounted bridge sectional model testing in wind tunnel, pioneered by Scanlan and described in the previous chapter cannot the capability of calculating motion-dependent aeroelastic loads.

The researchers X.G. Hua and Z.Q. Chen [33] proposed a method that allows to perform a flutter analysis using commercial finite element package ANSYS. The method is based on the definition of the aeroelastic loads by means of a particular user defined element and is shortly illustrated below.

The equation of motion for a deck section in the smooth flow can be expressed as:

$$M\ddot{X} + C\dot{X} + KX = F_{ae} \quad (4.4.1)$$

Where M , K and C are the global mass, stiffness and damping matrices, respectively; \ddot{X} , \dot{X} and X represent the nodal acceleration, velocity and displacement vectors, respectively; and F_{ae} denotes the vector of nodal self-excited forces defined in (4.3.1)-(4.3.3) and represented in *Figure 4.5*.

By converting the distributed aeroelastic forces of a generic element e of bridge girder into equivalent nodal loads acting on member ends, one obtains the equivalent nodal loadings for that element as:

$$F_{ae}^e = K_{ae}^e X^e + C_{ae}^e \dot{X}^e \quad (4.4.2)$$

Where K_{ae}^e and C_{ae}^e are the aeroelastic stiffness and damping matrices for element e , respectively. Using a lumped formulation, they can be expressed as:

$$K_{ae}^e = \begin{bmatrix} K_{ae1}^e & 0 \\ 0 & K_{ae1}^e \end{bmatrix} \quad (4.4.3)$$

$$C_{ae}^e = \begin{bmatrix} C_{ae1}^e & 0 \\ 0 & C_{ae1}^e \end{bmatrix} \quad (4.4.4)$$

$$K_{ae1}^e = a \begin{bmatrix} 0 & 0 & 0 & 0 & 0 & 0 \\ 0 & P_4^* & P_6^* & BP_3^* & 0 & 0 \\ 0 & H_6^* & H_4^* & BH_3^* & 0 & 0 \\ 0 & BA_6^* & BA_4^* & B^2 A_3^* & 0 & 0 \\ 0 & 0 & 0 & 0 & 0 & 0 \\ 0 & 0 & 0 & 0 & 0 & 0 \end{bmatrix} \quad (4.4.5)$$

$$C_{ae1}^e = b \begin{bmatrix} 0 & 0 & 0 & 0 & 0 & 0 \\ 0 & P_1^* & P_5^* & BP_2^* & 0 & 0 \\ 0 & H_5^* & H_1^* & BH_2^* & 0 & 0 \\ 0 & BA_5^* & BA_1^* & B^2A_2^* & 0 & 0 \\ 0 & 0 & 0 & 0 & 0 & 0 \\ 0 & 0 & 0 & 0 & 0 & 0 \end{bmatrix} \quad (4.4.6)$$

Where $a = \rho U^2 K^2 L_e / 2$ and $b = \rho U B K L_e$ and L_e is the length of the element e .

Hence it is necessary to represent the elemental stiffness and damping matrices due to motion-dependent aeroelastic forces by element MATRIX27. The user-defined element in ANSYS, MATRIX27 can only model either an aeroelastic stiffness matrix or an aeroelastic damping matrix instead of both of them simultaneously, so a pair of MATRIX27 elements are attached to each node of a generic bridge deck element as illustrated in *Figure 4.6*.

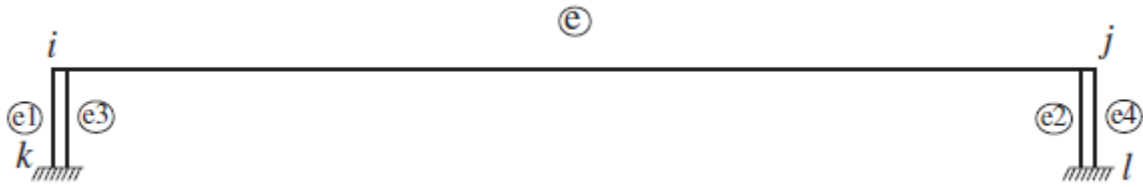


Figure 4.6: Hybrid finite element model [33].

The MATRIX27 elements $e1$ and $e3$ represent respectively the aeroelastic stiffness and damping of the node i , as the MATRIX27 elements $e2$ and $e4$ represent respectively the aeroelastic stiffness and damping of the node j . If the length of each bridge deck element is the same, the element matrices are simplified as:

$$K^{e1} = 2K_{ae}^e \quad (4.4.7)$$

$$C^{e3} = 2C_{ae}^e \quad (4.4.8)$$

$$K^{e2} = 2K_{ae}^e \quad (4.4.9)$$

$$C^{e4} = 2C_{ae}^e \quad (4.4.10)$$

Assembling all elemental matrices into global aeroelastic stiffness and damping matrices leads to:

$$F_{ae} = K_{ae}X + C_{ae}\dot{X} \quad (4.4.11)$$

Substituting (4.4.11) in (4.4.1) the mathematical model of an integrated system is obtained, with the effect of aeroelasticity parametrized by wind velocity and vibration frequency:

$$M\ddot{X} + (C - C_{ae})\dot{X} + (K - K_{ae})X = 0 \quad (4.4.12)$$

With this equation, complex eigenvalue analysis can be carried out to determine the eigenvalues of the system at specific wind velocity and vibration frequency.

Assuming the conjugate pairs of complex eigenvalues $\lambda_j = \sigma_j \pm i\omega_j$ and the conjugate pairs of complex eigenvectors $\phi_j = p_j \pm iq_j$ have been obtained, the system will be dynamically unstable if the real part of any eigenvalue become positive. Hence the condition for onset of flutter instability is stated as follow: at a certain wind velocity U_f the system has only one eigenvalue λ_f with zero real part, the corresponding wind velocity U_f being the critical flutter wind velocity and the imaginary part ω_j of the complex eigenvalue λ_f becoming the flutter frequency.

It is necessary to provide the variation of both wind velocity and vibration frequency in the complex eigenvalue analysis, so a mode-by-mode tracking method is employed to iteratively search the flutter frequency and the flutter velocity. The procedure is summarized in the following steps:

1. Establish the Finite Element model for the original structure without MATRIX27 elements, perform a modal analysis including the effect of permanent loads computing the first m natural frequencies ω_i^0 ($i = 1, 2, \dots, m$).
2. Determine the present wind velocity U .
3. Let the initial oscillation frequency ω_0 be the frequency ω_i^0 of each natural mode in turn.
4. Determine the reduced frequency K and the aeroelastic stiffness and damping matrices in MATRIX27 elements in (4.4.3) - (4.4.6) at the present iteration, and then carry out the complex eigenvalues analysis.
5. Compare the imaginary part of the i^{th} computed complex eigenvalue λ_i with ω_0 . If $|(Im(\lambda_i) - \omega_0)/Im(\lambda_i)| > 10^{-3}$ let $\omega_0 = Im(\lambda_i)$ and repeat step 4 and 5, otherwise go to step 6.
6. Loop steps 3-5 over all the m computed natural modes to obtain all m pairs of complex eigenvalues at the present wind velocity U .
7. Repeat steps 2-6 for the range of interest of wind velocity in order to obtain the variation of m pairs of complex eigenvalues with wind velocity.

PART 2

5. FLUTTER DERIVATIVES FROM PRESSURE COEFFICIENTS

As mentioned in the first part, the only method considered reliable for the calculation of flutter derivatives is based on experimental test in wind tunnels. However, several methods have been developed in the last years in order to obtain an approximate estimation very useful in pre-dimensioning phases. The most accurate are currently the ones based on the use of finite element programs. Various commercial software packages are available and able to simulate the interaction between the motion of a body immersed in a turbulent flow. Some theoretical aspect related to the numerical models of turbulence have been presented in *CHAPTER 3*, it must be noticed that the motion of the body immersed in the flow has never been introduced, in fact the body has ever been supposed motionless or fixed. Introducing the body motion leads to an exponential increase of the computational time, but rigorously it must be done for the numerical calculation of flutter derivatives.

The simplified approach presented in *section 2.4* is based on the pressure coefficients defined in Eq. (2.1.1) - (2.1.3) extractable from CFD analysis. However, the calculation of these parameters requires relatively low computational time, because the motion of the bridge deck can be neglected and performing several analyses for different flow angles of attack the coefficients slope can be calculated. It worth to note that a particularization of the method proposed in this thesis for the calculation of flutter derivatives has been already widely used: the flutter derivatives of thin airfoil. As a result of the potential flow theory [12], the pressure distribution induced by flow on a fixed airfoil under a small angle of incidence reduces in a zero drag force, an upward lift with a slope $C_{l,\alpha} = 2\pi$ and a pitching moment with a slope $C_{m,\alpha} = \frac{\pi}{2}$. By substitute these values in the Eq. (2.4.4) – (2.4.11) the flutter derivatives of thin airfoil are obtained. These formulas have been tested by Scanlan [17], in his book the flutter derivatives of thin airfoil have been compared with the flutter derivatives of three streamlined bridge deck finding a good agreement (*Figure 5.1*).

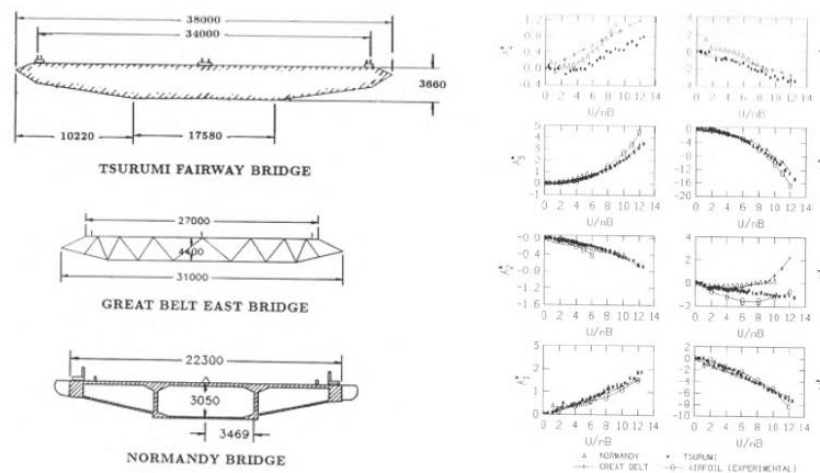


Figure 5.1: Comparison between flutter derivatives of thin airfoil and streamlined cross-sections [17].

The flutter derivatives of thin airfoil have also been used by several authors to compensate the lack of experimental data required. For instances Adel Al-Assaf in [34], after some observations of the results experimentally obtained by Scanlan for truss-stiffened girder bridges, proposed a set of “synthesized” flutter derivatives based on the Theodorsen functions. Next, he utilized that flutter derivatives to perform a flutter analysis of the Golden Gate Bridge and the second Takoma Narrows finding a good agreement with the results available in literature.

The aim of this chapter is to validate the approach abovementioned by the application of Eq. (2.4.4) – (2.4.11) in two real cases of which are available the experimental data extracted in the wind tunnel.

5.1. Flutter derivatives of Great Belt Est Bridge

The Great Belt Est Bridge (*Figure 3.4*) has been the subject of various studies because of its simplicity and high slenderness. In fact, it was one of the example presented by Scanlan in *Figure 5.1* with the aim of testing the flutter derivatives of the thin airfoil. In *Figures 5.2-5.3* are illustrated the flutter coefficients of the bridge calculated experimentally by Reinhold et al. [29], compared with the derivatives of thin airfoil and the derivatives calculated with Eq. (2.4.4) – (2.4.11). These latter have been represented in orange and have been named “Fung” while the derivatives of thin airfoil are named “Theodorsen” and illustrated in grey.

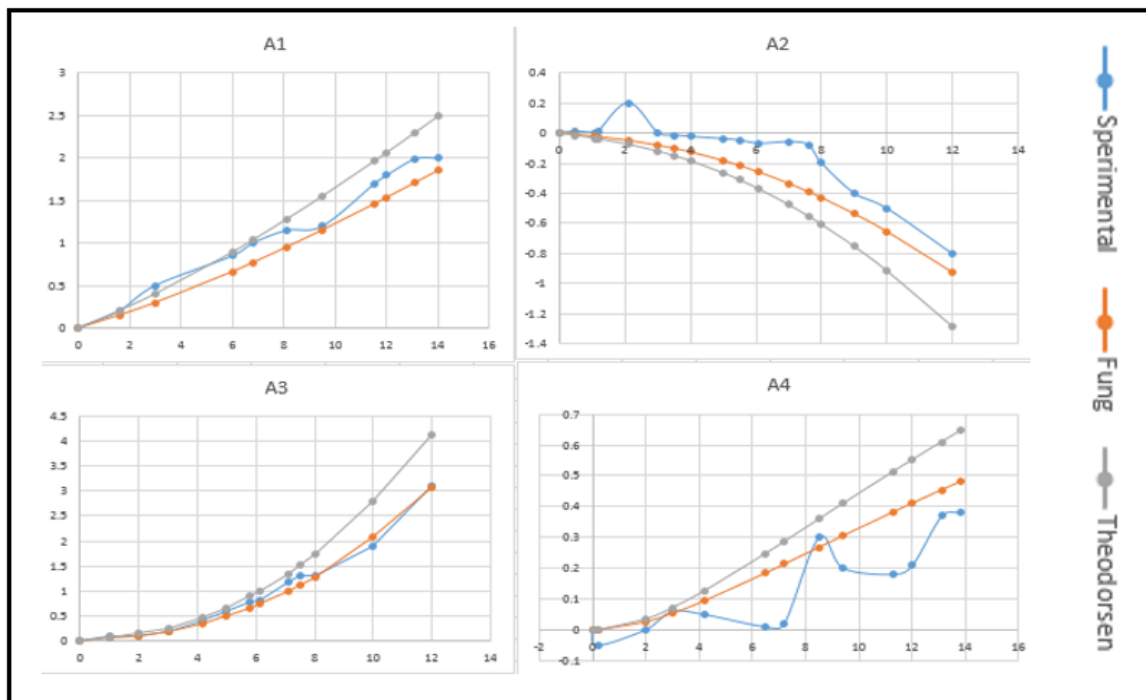


Figure 5.2: Moment flutter derivatives of the Great Belt Est.

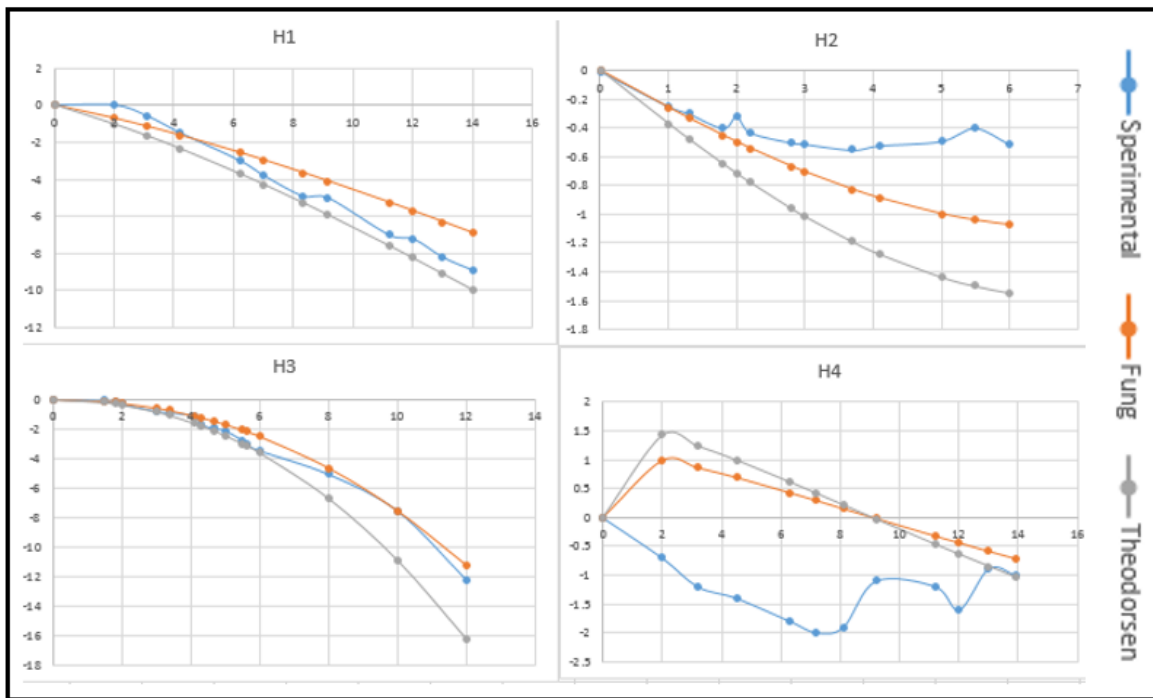


Figure 5.3: Lift flutter derivatives of Great Belt Est.

The flutter derivatives calculated by the Fung formulation refer to pressure coefficients obtained from wind tunnel testing of a 1:80 section model as reported by Larsen and reported in *Table 5.1* [35] [36]:

$C_{l,\alpha}$ [-/rad]	4.37
$C_{m,\alpha}$ [-/rad]	1.17

Table 5-1: Slope of the pressure coefficients of Great Belt Est.

From the comparison it is possible to notice that the Fung formulation leads generally to a good alignment to the experimental curves, the average trend is always respected except for the H_4 that in some cases could be neglected [34]. Moreover, it possible to conclude that in most plotted cases the Fung formulations find a better agreement with respect to the Theodorsen one, but unfortunately, is not immediate to assert which method is more conservative than the other.

5.2. Flutter derivatives of Akashi Kaykio

The Akashi Kaykio Bridge is the suspension bridge that currently has the longest span in the world: 1991 meters (its central span). It links the city of Kobe to Iwaya, on Awaji Island crossing the Akashi Strait (*Figure 5.4*).



Figure 5.4: View of Akashi Kaykio Bridge [37].

The bridge, unlike the Great Belt East treated in the previous chapter, has a steel truss stiffening girder. This characteristic makes him similar to the George Washington Bridge with the difference that the latter is equipped with a lower deck on the lowest level of the truss.

For the aerodynamic parameters of the bridge utilized in this section, reference has been made to Katsuchi [38] and Scanlan [39]. The static wind force coefficients on which are based the Fung formulas for the flutter derivatives are reported in *Table 5.2*. The flutter derivatives are shown in *Figures 5.5-5.6* where the comparison between the different formulations is made.

$C_{l,\alpha}$ [-/rad]	1.191
$C_{m,\alpha}$ [-/rad]	0.306

Table 5-2: Slope of the pressure coefficients of Akashi Kaykio.

The comparison shows a substantial alignment between the experimentally obtained flutter derivatives and the same calculated with the Fung formulation, especially with regard to the A_i . Furthermore, it is

5. FLUTTER DERIVATIVES FROM PRESSURE COEFFICIENTS

interesting to observe that for a truss-stiffened girder, the Theodorsen formulation for thin airfoil becomes unable to reliably predict the aerodynamic behavior.

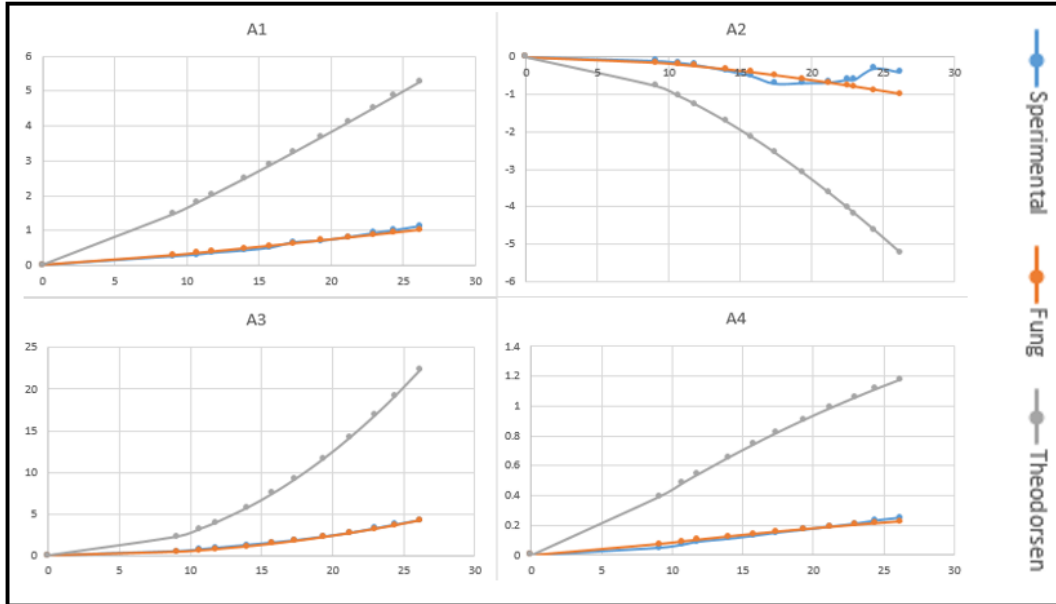


Figure 5.5: Moment flutter derivatives of the Akashi Kaykio.

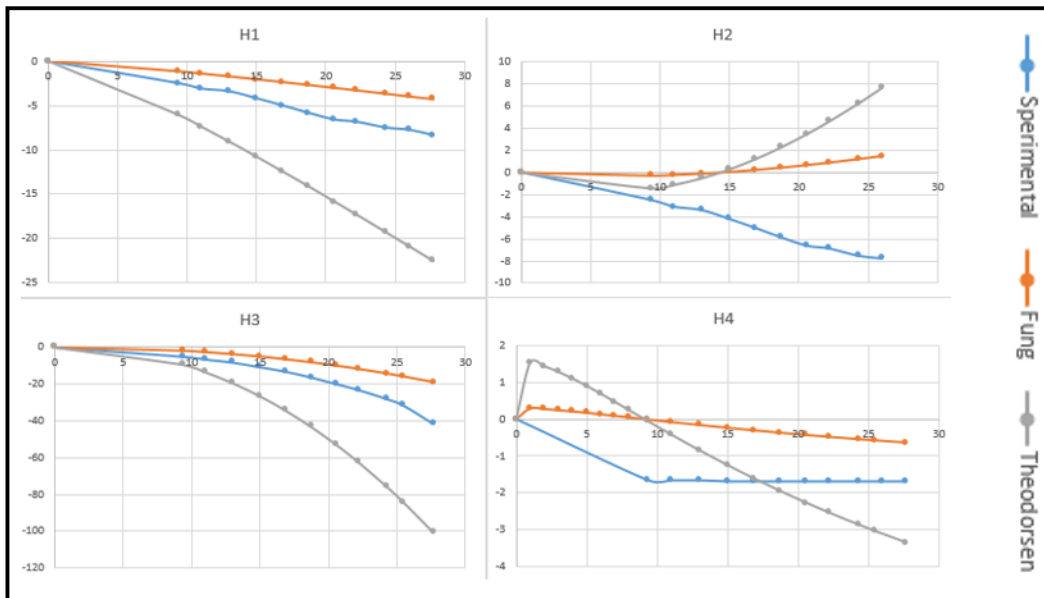


Figure 5.6: Lift flutter derivatives of Akashi Kaykio.

6. CFD SIMULATIONS

In the third chapter of this thesis, a short theoretical background of the computational fluid dynamics has been presented. Several analyses have been performed in order to test the reliability of different factors as the turbulence model, mesh sizing, extension of the computational domain and the boundary conditions. The finite element package ANSYS FLUENT was chosen both for meshing and simulating the fluid flow around the rigid body, with the aim of integrate the pressure distribution and finally obtain the aerodynamic static coefficients. Before dealing with the various case studies, the characteristic that the models have in common will be listed.

For each model a RANS simulation has been performed, modeling the turbulence with the $k - \omega SST$ as in articles mentioned in *Chapter 3*. As a boundary conditions, the velocity inlet was characterized by a wind velocity of 30 m/s , a turbulent intensity of 0.5% according to standard wind tunnel conditions for laminar flow, and a turbulent viscosity ratio equal to 2. The pressure outlet region was created with a null speed and the same turbulent intensity and viscosity of the velocity inlet. The dimensions of the computational domain were set following the indication of [21], hence around $12B$ in along the wind direction and $5.5B$ in the transversal one. The domain has been subdivided in different regions as shown in *Figure 6.1*.

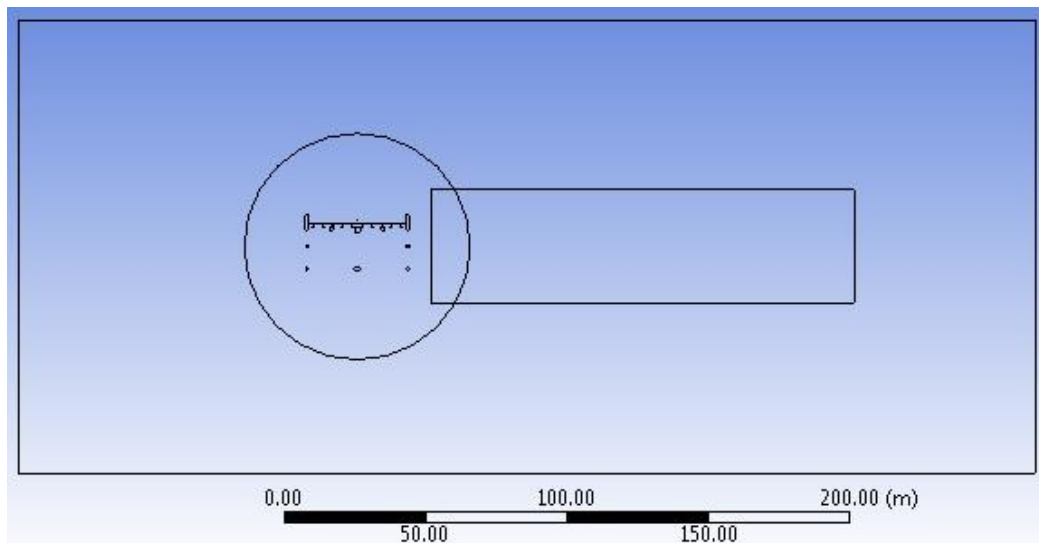


Figure 6.1: Geometrical division of the computational domain.

The outside rectangle delimits the fluid region, the left and the right size represent the velocity inlet and the pressure outlet, respectively. The circle and the inner rectangle has been created as auxiliary geometric entities allowing a differentiated meshing of the closer fluid regions and the wind wake. Being the dimensions of the models very similar, the same mesh size has been set following the indications of

[21]. In the inner regions the mesh goes from an edge sizing of *1 centimeter* until a maximum size of *25 centimeters* with a growth ratio equal to 1.1. In the fluid region between the external boundary and the inner parts a maximum size of *3 meters* was fixed and a growth ratio of 1.2. In *Figures 6.2 and 6.3* an example of meshed model is illustrated with different zoom levels.

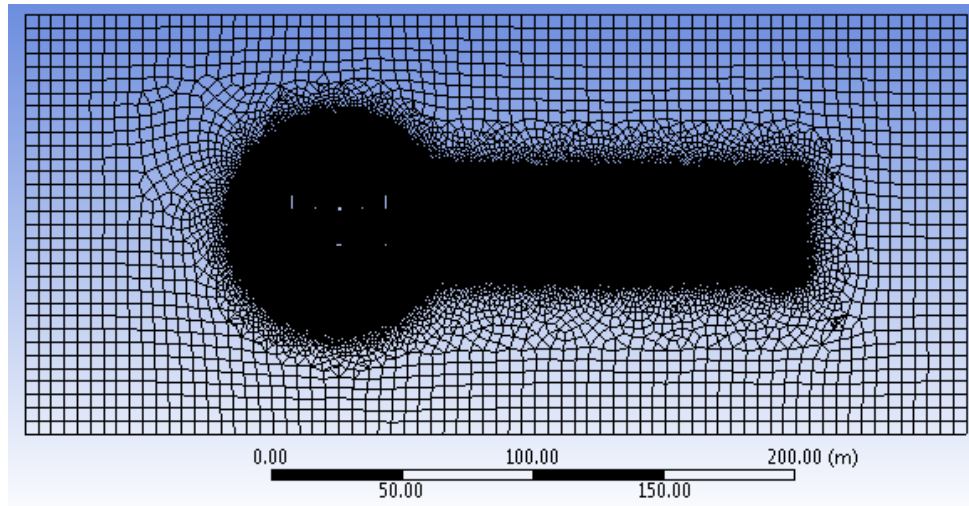


Figure 6.2: Discretization of the fluid domain.

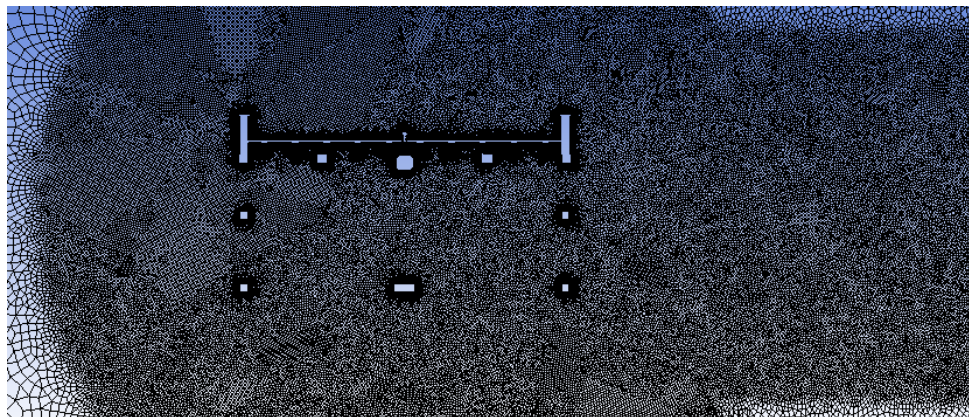


Figure 6.3: Discretization of the inner regions closest to the deck.

A quadrilateral mesh has been chosen for each models in order to reduce the computational time. Finally, the bridge deck edges were selected for the integration of the pressure distribution, and the model parameters like wind velocity, chord length (B) and air density have been set with the purpose of get the dimensionless pressure coefficients directly by the program. To take into account the different angle of attacks, several analyses has been performed rotating the bridge cross-section and keeping unaltered the boundary conditions and the computational domain. Next, the derivatives of the coefficients with respect to the angle of attack have been calculated by the definition of the incremental ratio: $\frac{C_i(\alpha_0 + \Delta\alpha) - C_i(\alpha_0)}{\Delta\alpha}$.

6.1. Great Belt East

The Great Belt East bridge was presented and shortly described in the previous chapters, its girder deck has been chosen as first test problem due to its relative simplicity. The geometrical values of the cross-section are reported in *Figure 6.3*, it worth to note that the various models found in literature may present some little geometrical differences.

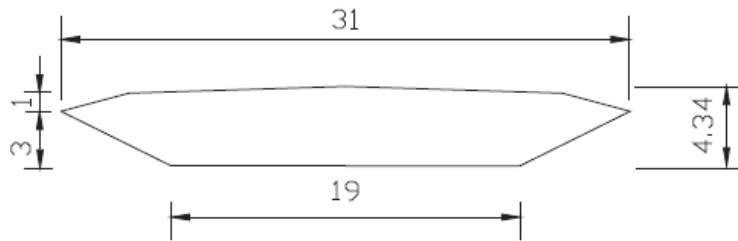


Figure 6.4: Great belt East cross-section.

The computational domain is 360×180 square meters, the inner rectangular region is 180×30 , the mesh size and the boundary conditions have been defined previously. In *Figure 6.4* the distribution of velocity magnitude and pressure are shown in the case of horizontal flow.

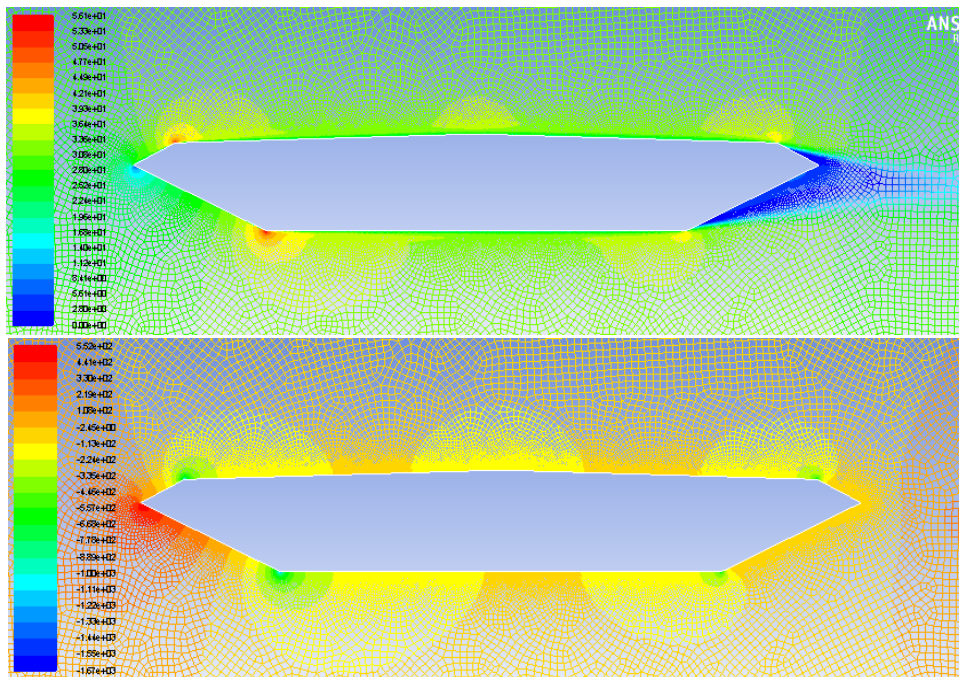


Figure 6.5: Distribution of velocity magnitude and static pressure around the deck with $\alpha = 0^\circ$.

In the next figures the same distributions are reported for different angles of attack in order to provide a qualitative representation of the parameters variation (*Figure 6.5*).

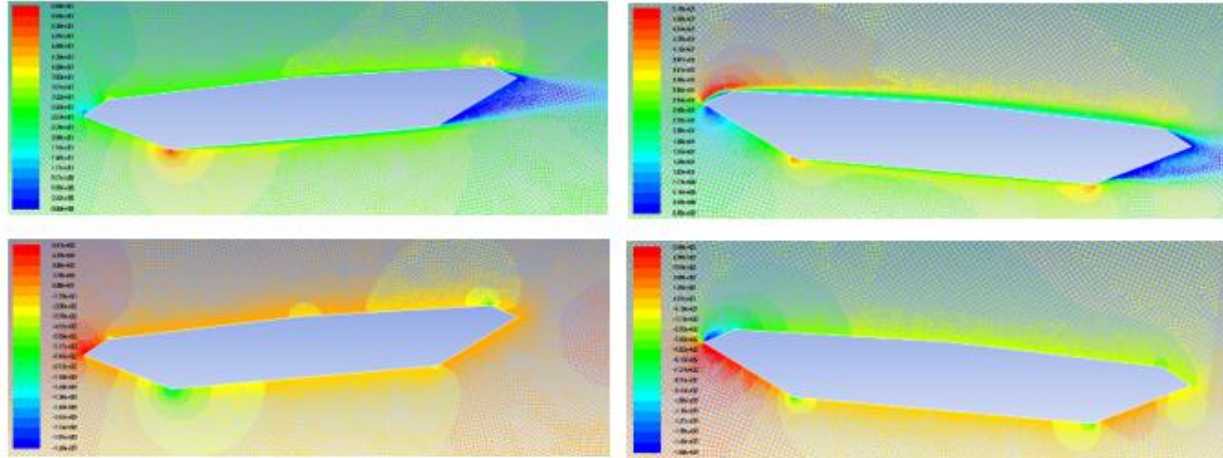


Figure 6.6: Distribution of velocity magnitude and static pressure around the deck with $\alpha = \pm 5^\circ$

The results obtained, in terms of aerodynamic static coefficients are plotted in *Figure 6.6*, where in addition, a comparison with the results obtained in the research mentioned in *section 3.2* is made [21].

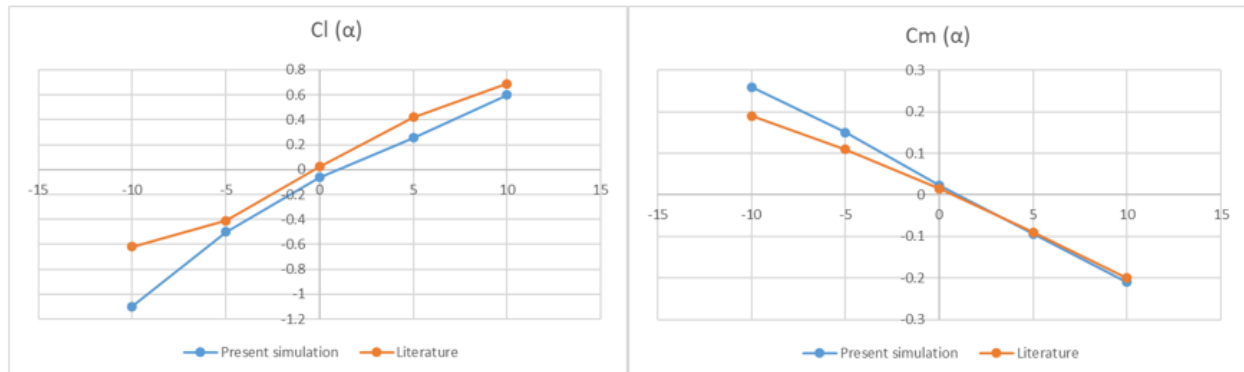


Figure 6.7: Aerodynamic static coefficients of Great Belt East as functions of the angle of attack.

The graphs above show a good agreement between the results obtained by the simulation in FLUENT and the results found in literature, especially with reference to coefficients slope. The latter indeed, represent the main goal of the simulations because the Fung formulation for flutter derivatives is based on them.

6.2. Akashi Kaikyo

The Akashi Kaikyo bridge is introduced in *section 5.2 (Figure 5.4)*, it has been chosen as a case study because of its truss girder (*Figure 6.8*). In fact, a two-dimensional model of a truss represents a forced simplification compared with the 2D model of the streamlined girder bridge presented in the previous section.



Figure 6.8: View of the Akashi Kaikyo lower level.

Initially, several efforts were made with the aim of represent the aerodynamic behavior with a simplified 3D model (*Figure 6.9*). Unfortunately, the huge solid domain and the precision level required lead to an impossibility to generate a suitable mesh discretization with the processor available.

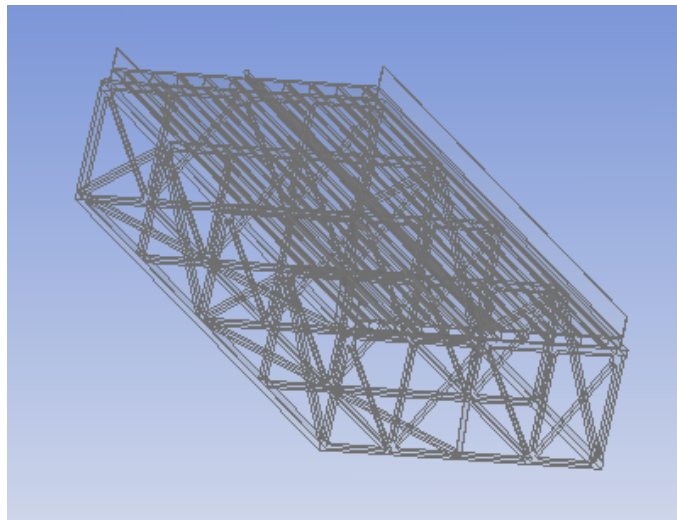


Figure 6.9: 3D model of the Akashi Kaikyo truss girder.

Hence inevitably, it was opted for a bi-dimensional model. After taking a cue from the work presented in *section 3.3* [30], the 2D model was created modeling only the main structural elements. The computational domain is 360×160 , the inner region is composed by a circle with radius equal to 40 meters and a rectangle 150×30 , the mesh size and the boundary conditions have been defined previously. In *Figure 6.10* the distribution of velocity magnitude and pressure are shown in the case of horizontal flow.

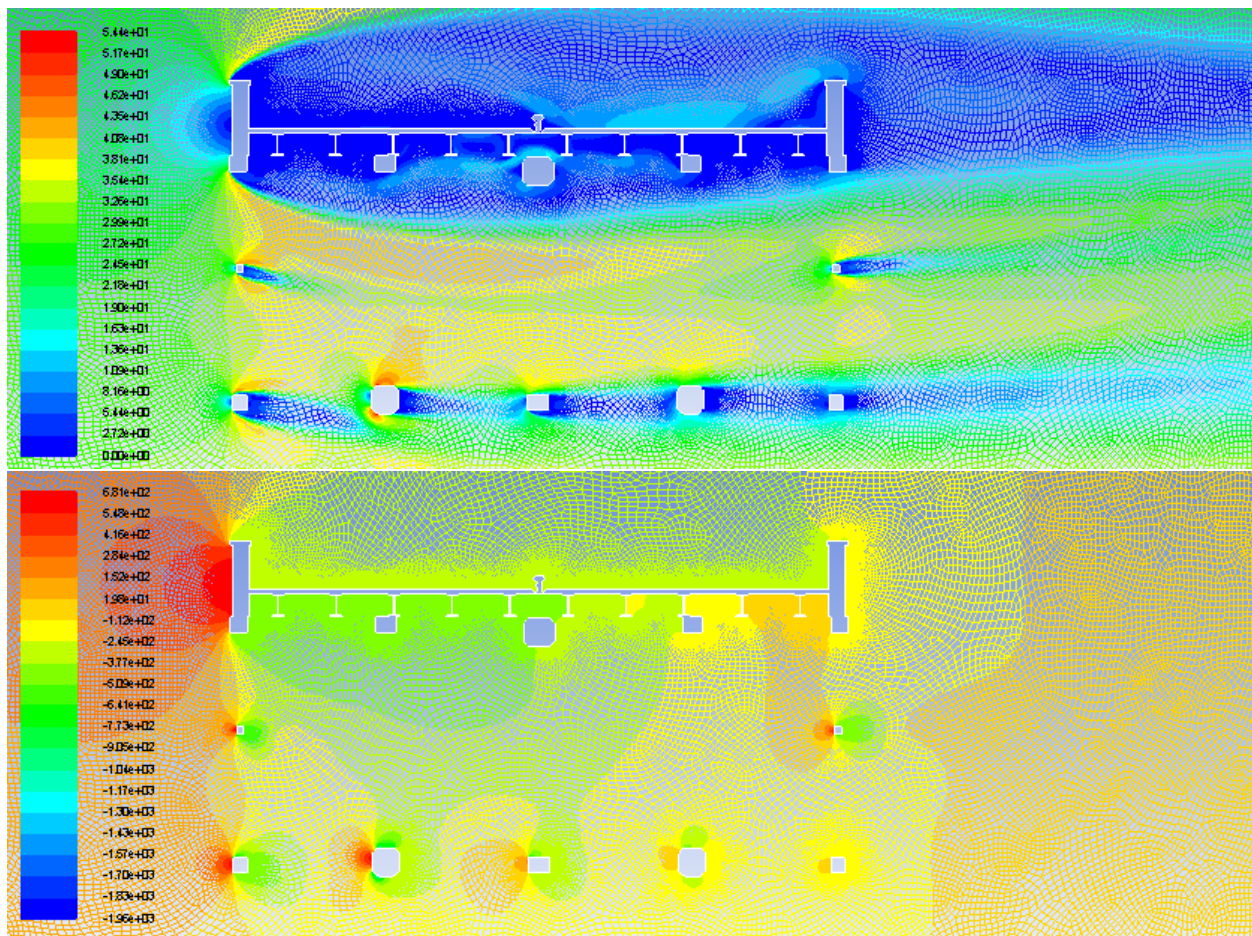


Figure 6.10: Distribution of velocity magnitude and static pressure around the deck with $\alpha = 0^\circ$.

It is possible to note that the mesh size seems able to catch the flow characteristics in the regions close to the edges. Furthermore, the interaction between the upper and the lower level is influenced by the diagonal beams composing the truss, modeled only with their cross-section placed at half height. It also must be noticed that the 2D model does not contain any information regarding the porous grids and the envelope of the truss among the wind direction.

In *Figure 6.10* the distributions of velocity and static pressure for different angles of attack are reported, in order to provide a qualitative representation of the parameters variation. The aerodynamic static coefficients are plotted as functions of the angle of attack in *Figure 6.11*, next the results are summarized

and compared with the ones obtained by other authors in *Table 6.1*. The comparison between the results obtained by other authors shows unneglectable differences. Even if the pressure coefficients obtained with null angle of attack could be considered reliable, their derivatives cannot.

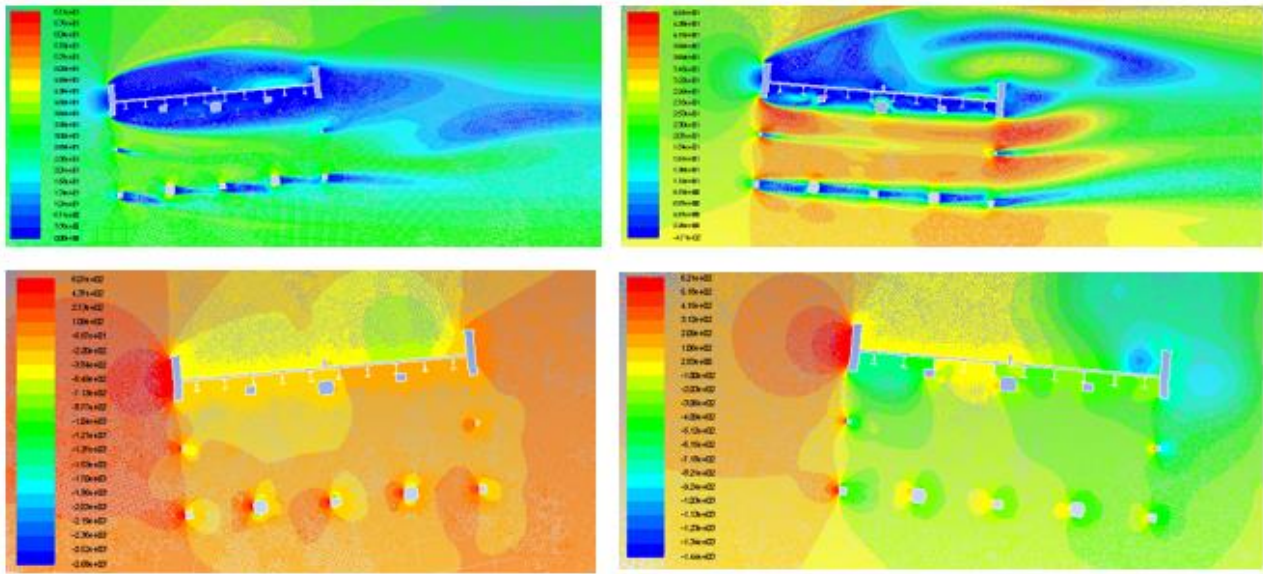


Figure 6.11: Distribution of velocity magnitude and static pressure around the deck with $\alpha = \pm 5^\circ$.

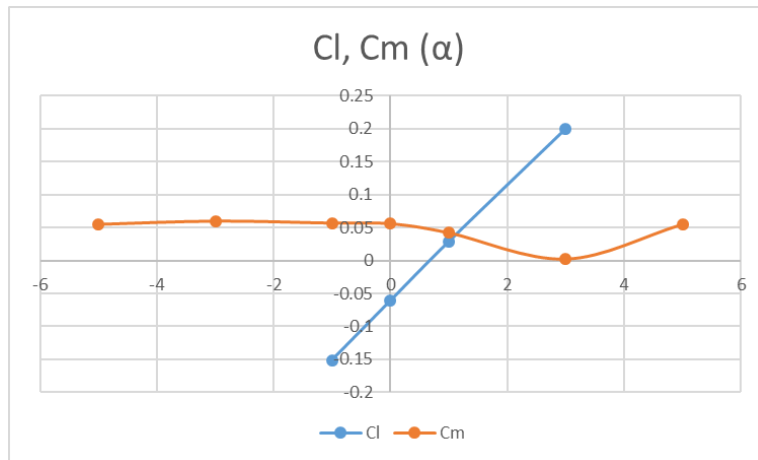


Figure 6.12: Aerodynamic static coefficients of Akashi Kaikyo as functions of the angle of attack.

Author	$C_D[-]$	$C_L[-]$	$C_M[-]$	$C'_L \left[\frac{-}{rad} \right]$	$C'_M \left[\frac{-}{rad} \right]$
Katsuchi [38]	0.386	0.094	0.01	1.905	0.272
Scanlan [39]	0.421	0.025	0.013	1.192	0.307
Present simulation	0.313	0.061	0.056	5.120	0.801

Table 6-1: Comparison of the Aerodynamic static coefficients of Akashi Kaykio.

It is possible to attribute this great difference to the complexity of the real truss girder (*Figure 6.8*). It can be asserted that a two-dimensional model is not able to represent the aerodynamic behavior of the bridge. Alternatively, the simplifications imposed by the turbulence model (*Chapter 3*), that has been validated for simpler model, could not work as well for this specific case. Or else, the turbulent intensity and viscosity set as boundary conditions could be calibrated differently.

Despite the results are not been considered correct, a 3D model is not a realizable option. Hence a 2D model has been done to represent the truss-like girder of the stiffened version of the George Washington Bridge (1962). Indeed, there are many differences between the two truss cross sections that can give hope that the analysis of the George Washington Bridge can lead to better results; in fact, the latter is characterized by two decks linked by a steel truss (*Figure 6.13*).



Figure 6.13: View of the lower deck of George Washington Bridge.

So its aerodynamic behavior could be closer to a combination of two mid-bluff decks rather than a properly truss. Anyway, in *Chapter 7* it has been proposed a method to validate the flutter derivatives by the comparison of two analyses in which the wind actions are modeled differently.

6.3. George Washington Bridge, single deck (1931)

The George Washington Bridge, as originally built was made from a single deck (*Figure 1.4*). The geometrical data of the cross section has been taken by [40], the model of the cross section is shown in *Figure 6.14*.

The computational domain is 360×180 , the inner region is composed by a circle with radius equal to 20 meters and a rectangle 150×24 for the wake, the mesh size and the boundary conditions have been defined previously. In *Figure 6.14* are also shown the distribution of velocity magnitude and pressure in the case of horizontal flow.

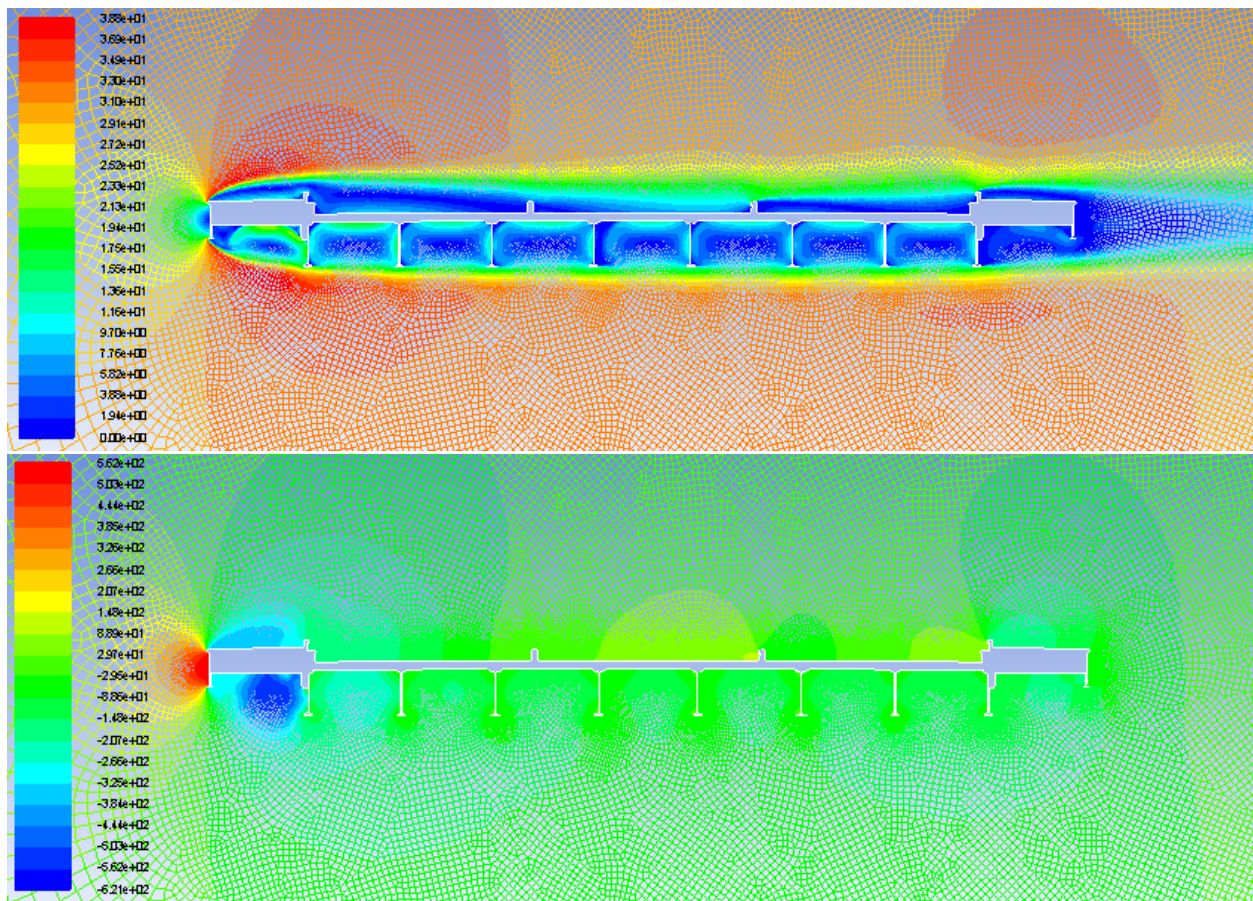


Figure 6.14: Distribution of velocity magnitude and static pressure around the deck with $\alpha = 0^\circ$.

The calculated aerodynamic static coefficients are plotted in *Figure 6.14* and summarized in *Table 6.2* in absolute value.

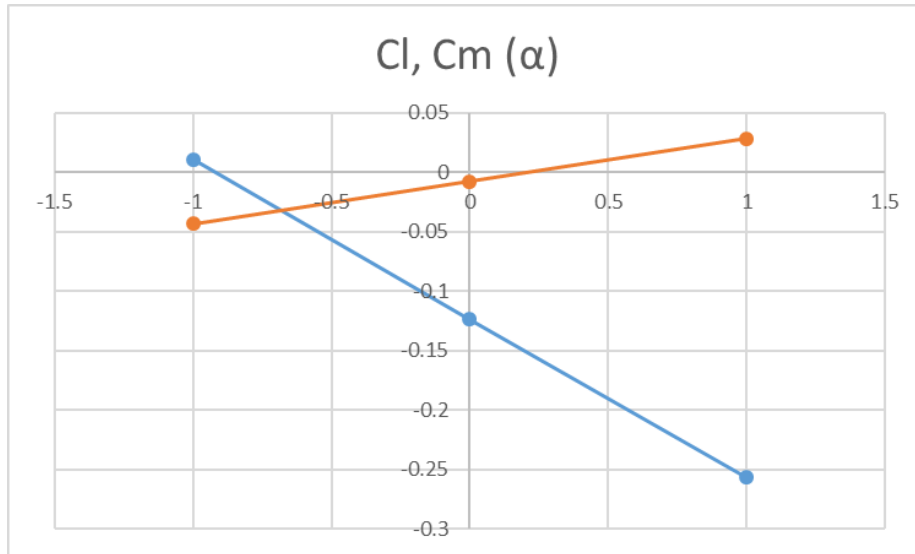


Figure 6.15: Aerodynamic static coefficients of George Washington Bridge (first version) as functions of the angle of attack.

$C_D[-]$	$C_L[-]$	$C_M[-]$	$C'_L \left[\frac{-}{rad} \right]$	$C'_M \left[\frac{-}{rad} \right]$
0.0549	0.124	0.0079	7.6	2.04

Table 6-2: Aerodynamic static coefficients of George Washington Bridge (first version).

Unfortunately, no similar analyses have been found in literature for a comparison. However, the results have been critically analyzed and considered reliable. Firstly, from *Figure 6.15* is possible to note the linearity of the functions around $\alpha = 0^\circ$, this is a peculiarity of the coefficients experimentally noticed for several mid-bluff profiles. Following, *Figure 6.14* shows that the distribution of the velocity magnitude can be viewed as a distribution around a flat plate, since the lateral obstacles deviate the airflow making him overtake the inner obstacles represented by the longitudinal beams. For this reason, the derivatives of the pressure coefficients were expected to be close to the theoretical values of the flat plate:

$$C'_L = 2\pi = 6.28 \left[\frac{-}{rad} \right] \quad (6.3.1)$$

$$C'_M = \frac{\pi}{2} = 1.57 \left[\frac{-}{rad} \right] \quad (6.3.2)$$

The higher values calculated for the bridge are well explained by the air recirculation between the longitudinal beams.

6.4. George Washington Bridge, double deck (1962)

The lower deck of the George Washington Bridge was constructed under the existing span from 1958 to 1962 because of increasing traffic flow, in fact it provides six additional lanes (*Figure 6.13*). From a mechanical point of view, the bridge has been certainly stiffened, is not immediate to assert the same for the aerodynamic aspect. The wind loads increase proportionally to the surface of the material added and the aerodynamic behavior became more complex. Anyway, in most cases the truss-stiffened girder is characterized by higher critical wind speed and a better performance with respect to the simple girder, except in cases where the cross section is designed with regard to aerodynamic aspects. The geometrical data of the cross section has been taken by [40], the model of the cross section is shown in *Figure 6.16*.

The computational domain is 360×180 , the inner region is composed by a circle with radius equal to 40 meters and a rectangle 150×30 for model the wake, the mesh size and the boundary conditions have been defined previously. In *Figure 6.16* are also shown the distribution of velocity magnitude and pressure in the case of horizontal flow.

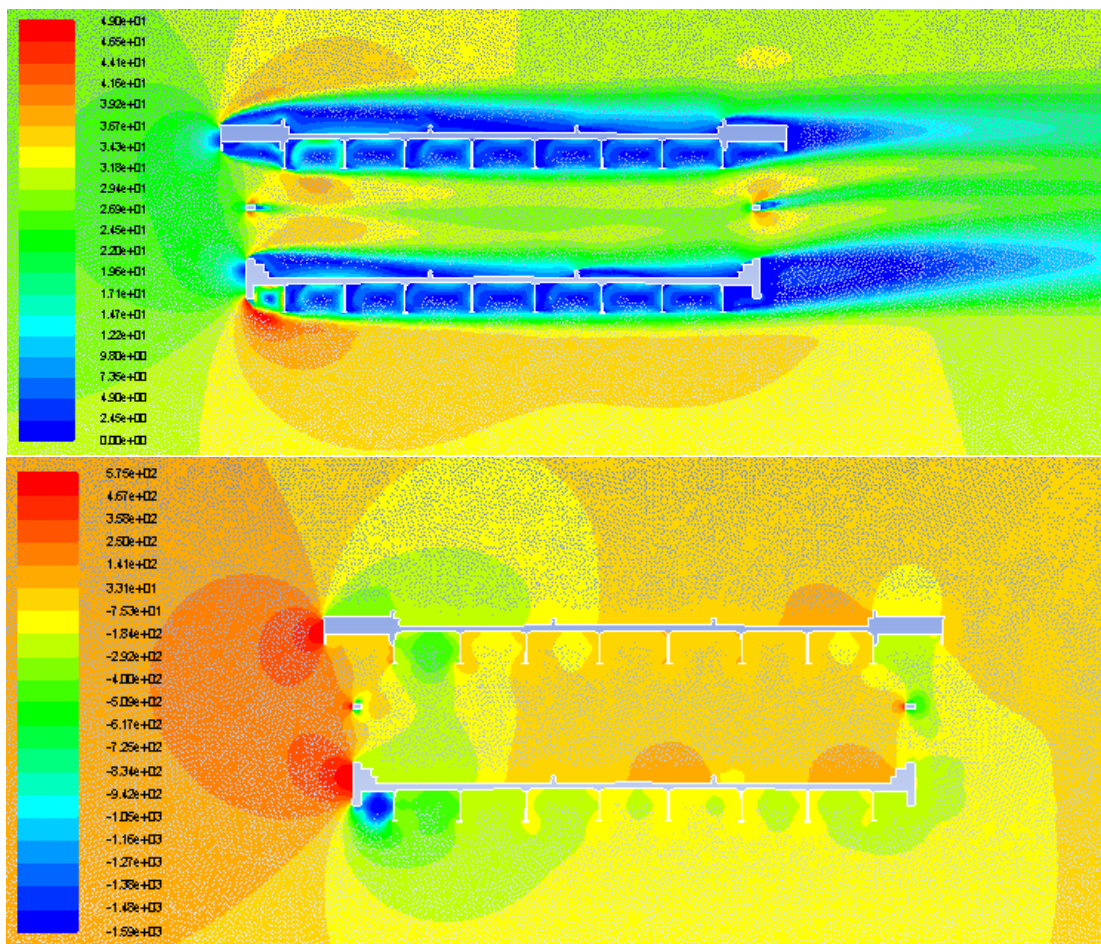


Figure 6.16: Distribution of velocity magnitude and static pressure around the deck with $\alpha = 0^\circ$

The calculated aerodynamic static coefficients are plotted in *Figure 6.17* and summarized in *Table 6.3* in absolute value.

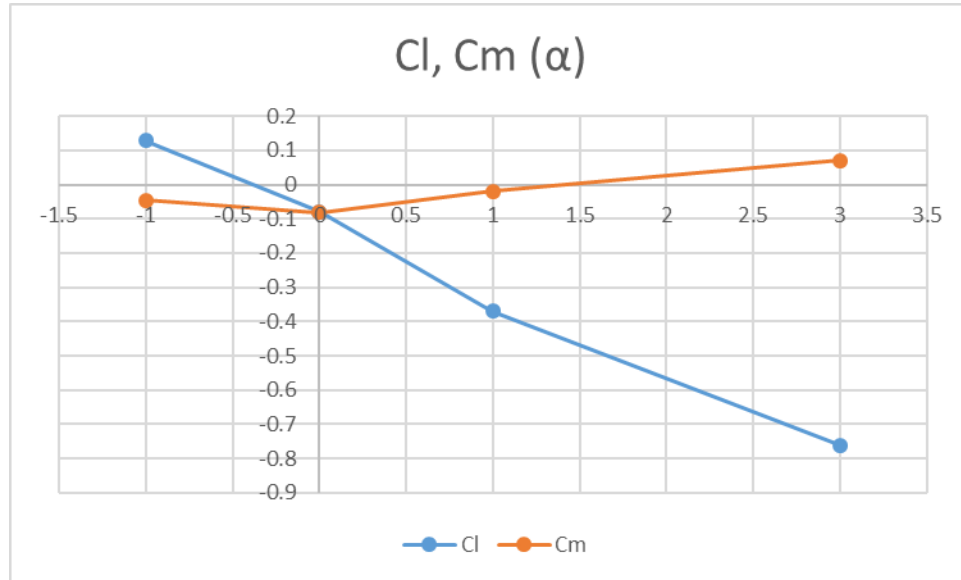


Figure 6.17: Aerodynamic static coefficients of George Washington Bridge (last version) as functions of the angle of attack.

$C_D[-]$	$C_L[-]$	$C_M[-]$	$C'_L \left[\frac{-}{rad} \right]$	$C'_M(+)\left[\frac{-}{rad} \right]$	$C'_M(-)\left[\frac{-}{rad} \right]$
0.23	0.08	0.081	13.11	1.37	0.06

Table 6-3: Aerodynamic static coefficients of George Washington Bridge (last version).

As mentioned in *section 6.2*, since the two-dimensional model of the Akashi Kaykio has not provided good results, this model cannot be considered totally reliable. Moreover, as shown in *Figure 6.17* and highlighted in *Table 6.3*, the moment coefficient is not linear around 0° . It presents a different slope in the left and right surrounds, even with different sing. For upcoming calculations, the coefficient has been supposed linear in the range $[-1^\circ; 1^\circ]$ and accordingly, the slope has been calculated as:

$$\frac{C_i(1^\circ) - C_i(-1^\circ)}{2^\circ} = 2.035 \left[\frac{-}{rad} \right] \quad (6.4.1)$$

The derivative of the lift coefficients has a reasonable value, since this is a double deck and as stated in the previous chapter, its value is close to the double of Eq. (6.3.1).

7. FLUTTER ANALYSIS OF GEORGE WASHINGTON BRIDGE

There are many methods to perform a flutter analysis of a suspension bridge; in *chapter 4* the theoretical background was introduced. In this work of thesis, it has been chosen to perform the analyses by finite element numerical models using the commercial software ANSYS APDL. One of the main reason is that the numerical models in ANSYS APDL allow to easily take in to account several non-linear aspects of fundamental importance for the suspension bridges. In fact, this kind of structures presents a non-linear geometric behavior due to hangers and main cables. The increasing of pull stresses in main cables induce a reduction of displacements given by further loads. Accordingly, the weight of the bridge itself generate a global stiffening of the structure, so neglecting the influence of these phenomena lead to wrong physical representations.

The modeling of self-excited load and the iterative technique for the determination of flutter velocity and frequency has been explained in *section 4.4*. For the numerical simulation of the mechanical behavior three different kind of finite elements has been used: BEAM189, LINK180, MASS21. BEAM 189 is a linear beam element composed by three nodes (beginning, middle, end) and an additional one to define the spatial orientation i.e. the local reference system. It is a 3D element having six degrees of freedom per node: translation and rotation in the three spatial directions defined by the local reference system; the element can be used with any cross section using the appropriate ANSYS command, and includes stress stiffness terms by default in any analysis that includes large-deflection effects. LINK180 is a 3D element that can be used to model trusses, cables and links. It is a uniaxial tension-compression element unable to transfer any moment, so it is composed by two nodes (beginning, end) each having three degrees of freedom: translation in the three spatial directions. MASS21 is a point element useful to model the structural mass properties. It can have up to 6 degrees of freedom in a 3D model and allow to assign different mass and rotary inertia to each coordinate direction. In this work it has been used only to model the mass moment of inertia in some simplified models, the weight of the elements has been defined as a combination of sectional properties and material models. Ultimately, the non-linear geometric behavior of the bridges, in particular of the main cables, has been taken into account in terms of pre-stress effects. In facts, the software allows to include effects due to the pretension in a modal damped analysis, simply by running a preliminary static analysis in which the pre-stress effects are include, and next running the modal damped analysis, again including the pre-stress effects. This method has been validated by several models, comparing the results obtained with the theoretical exact solution in some cases and with literature data in other. The validation examples have not been reported for the sake of brevity, reference can be made to [41].

In this chapter, one case study is reported in order to validate the procedure explained in *section 4.4* for the calculation of the flutter velocity and frequency of a simply supported beam-like bridge with thin airfoil cross section. Finally, the analyses of the George Washington Bridge are performed for both versions (1931,1962). For the double decked version (1962) two different approaches are developed because of the uncertainty related to the flutter derivatives input parameters.

7.1. Simply supported thin airfoil structure

The simply supported beam-like bridge with a thin airfoil cross-section is an ideal model of which is available the theoretical solution. It has been chosen as a case study in order to try the tricky method developed by [33] and introduced in *section 4.4*. It was necessary to ensure the correct usage of the matrix elements utilized for modeling the motion induced wind loads, and to get involved in the extraction of real and imaginary parts of the eigenvalues at each step. The parameters of the structure are summarized in the following table (*Table 7.1*):

Span length (L)	300 [m]
Chord (B)	40 [m]
Young modulus (E)	2.1E11 [N/m ²]
Poisson modulus (ν)	0.3 [-]
Vertical moment of inertia (I_z)	85.714 [m ⁴]
Lateral moment of Inertia (I_y)	10 [m ⁴]
Torsional moment of Inertia (I_t)	5.076 [m ⁴]
Mass moment of Inertia per unit span length (I_m)	4.5E6 [Kg*m ² /m]
Deck mass per unit span length (m)	20000 [Kg/m]
Air density	1.248 [Kg/m ³]

Table 7-1: Model parameters of the simply supported thin airfoil.

The deck was modeled with 30 BEAM189 elements, each having the same length of ten meters. A MASS21 nodal element has been located every ten meters, at the end of each element, in order to model the mass moment of inertia. As boundary conditions, the nodes at the ends of the beam are imposed to be fixed in all the translation directions and in the torsional rotation R_x , being x the longitudinal axis.

Natural modal analysis of the bridge FE model without MATRIX27 elements is first conducted, where the lumped mass formulation is used to construct the mass matrix. The first ten eigenvalues have been extracted and summarized in *Table 7.2*, where also a comparison have been done with the results obtained in [33]. The table shows a good agreement, errors always remain below 1%, except for the lateral modes, where the error of the 9th frequency reach the 4%. MATRIX27 elements are then incorporated into the structural model to perform the damped modal analyses. A total of 58 elements are employed to formulate 29 aeroelastic stiffness and 29 aeroelastic damping; the elements have been assigned to line

entities having the same length of the deck elements, the fictitious nodes external to the deck generated in this way have been fixed in all degrees of freedom. The hybrid finite element model incorporating structural model with MATRIX27 elements for flutter analysis is illustrated in *Figure 7.1*. The flutter derivatives of thin airfoil have been calculated with Eq. (2.4.4) – (2.4.11) where $C_{l,\alpha} = 2\pi$ and $C_{m,\alpha} = \frac{\pi}{2}$. In *Figure 7.2* the flutter derivatives are plotted as functions of the reduced wind speed.

Mode number	Mode shape	Mode frequency [Hz]		Error [%]
		Present simulation	[33]	
1	S-V	0.1786	0.1788	-0.112
2	S-T	0.5028	0.5028	0.000
3	S-L	0.5175	0.5236	-1.165
4	A-V	0.7123	0.7154	-0.433
5	A-T	1.004	1.0043	-0.030
6	S-T	1.503	1.503	0.000
7	S-V	1.5946	1.6096	-0.932
8	A-T	1.9976	1.9976	0.000
9	A-L	2.0014	2.0944	-4.440
10	S-T	2.4868	2.4867	0.004

Table 7-2: Modal frequencies of the simply supported thin airfoil.

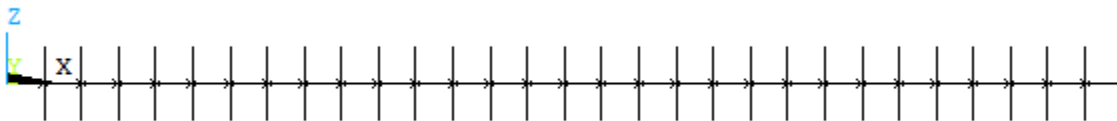


Figure 7.1: Finite element model for flutter analysis.

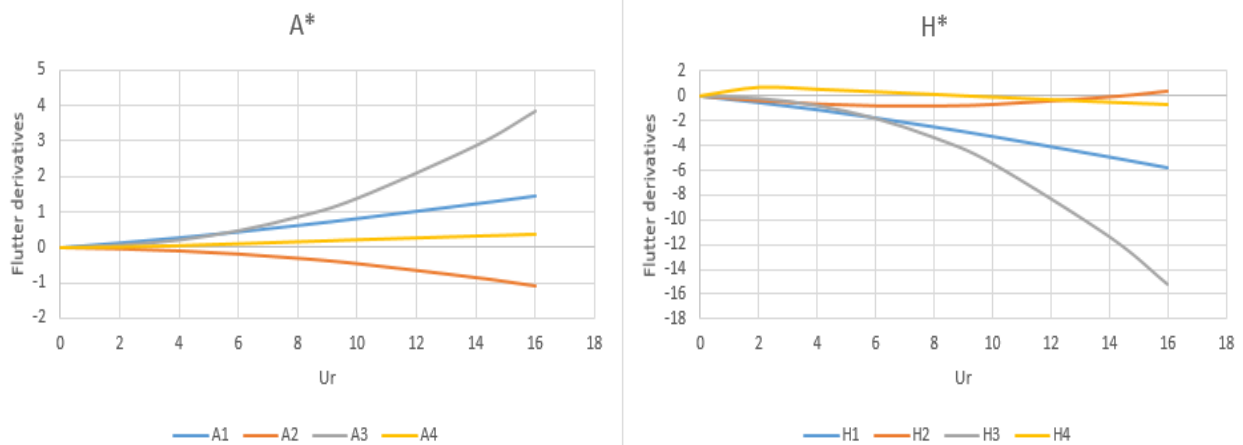


Figure 7.2: Flutter derivatives for thin airfoil.

Finally, the iterative procedure for the determination of flutter speed and frequency has been carried out. For brevity, since it was known the solution, only the evolution of the second mode has been developed and reported in *Figure 7.3* with respect to the wind velocity. The increment step of wind velocity was set variable, from a maximum value of 20 meters per second in the ranges far from the flutter instability to a minimum of 1 meter per second around the instability. So the flutter velocity resultant has the accuracy of the unit (m/s). After all, the results obtained have been compared with the exact solution and with the values obtained in [33] (*Table 7.3*).

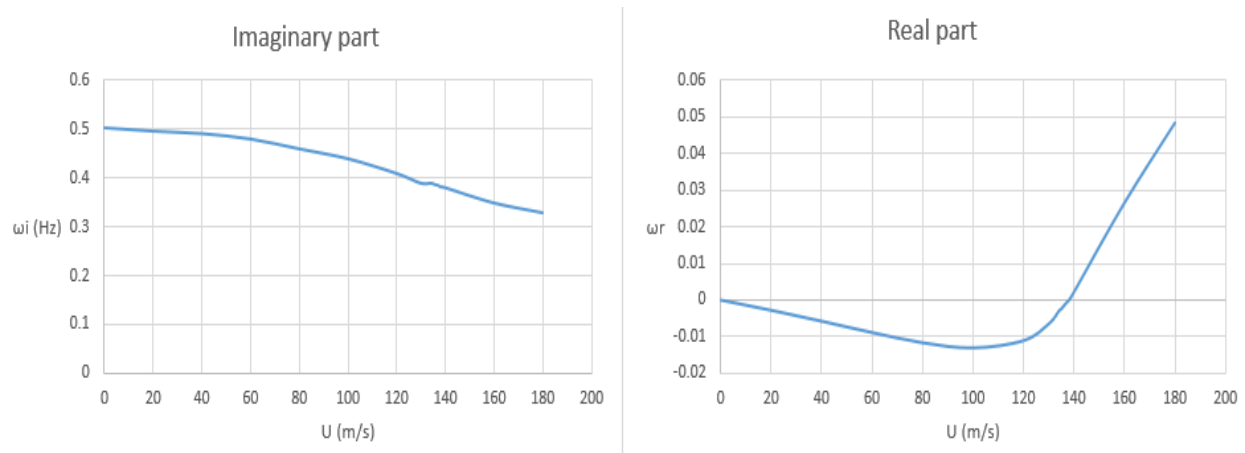


Figure 7.3: Variation of imaginary and real parts of the 2nd complex eigenvalue versus wind velocity.

Source	Flutter wind velocity [m/s]	Error [%]	Flutter frequency [Hz]	Error [%]
Present simulation	138	-	0.386	-
Exact Solution	136.5	1.10	0.3914	-1.38
()	135.1	2.15	0.394	-2.03

Table 7-3: Comparison of flutter analysis results for thin airfoil bridge.

The table above shows a good agreement between the results obtained and the ones used as a basis for comparison: the difference recorded with the exact solution are under the 2% regarding both the flutter wind velocity and frequency.

7.2. George Washington Bridge, single deck (1931)

The George Washington Bridge has been introduced in *section 1.1* and its sectional aerodynamic behavior was discussed in *section 6.3*. In this section a finite element model will be treated in order to study the global structure performance of the bridge, and finally determine the critic wind velocity and frequency that induce the flutter instability. The ANSYS numerical model was realized with the geometrical properties found in literature [42] and illustrated in *Table 7.4*. A “Fish-bone” model of the central span was realized: the slab constituting the deck was modeled as a beam element having the same geometrical properties of the slab, and its connection with the hangers has been modeled with “rigid links”.

Span length (L)	1066.8 [m]
Chord (B)	36.3 [m]
Sag	97.3 [m]
Area cable	1.03 [m ²]
Area Hangers	0.011 [m ²]
Young modulus of cables, deck, Hangers	2.1E11 [N/m ²]
Poisson modulus (ν)	0.3
Deck vertical moment of inertia (I _z)	28.8 [m ⁴]
Deck lateral moment of Inertia (I _y)	0.0101 [m ⁴]
Deck torsional moment of Inertia (I _t)	0.023 [m ⁴]
Deck mass moment of Inertia per unit span length (I _m)	4.475E6 [Kg*m ² /m]
Deck mass per unit span length	28600 [Kg/m]

Table 7-4: Geometrical and mechanical properties of George Washington Bridge.

The two main cables of each side are modeled as an equivalent cable using BEAM189 elements and are restrained by hinges at the extremities. Hangers are realized using LINK180 elements that transmit only tension forces between the deck and the main cables. As mention before, the deck is modeled with beam

7. FLUTTER ANALYSIS OF GEORGE WASHINGTON BRIDGE

elements, is connected with the hangers by rigid links and simply supported in its extremities. The mass moment of inertia of the deck was modeled using MASS21 elements at the ends of each deck element. Finally, the rigid links have been modeled with BEAM189 elements having a big inertia to obtain rigid flexural behavior and its weight is imposed equal to zero. The numerical model is shown in *Figure 7.4*. Before introducing the aeroelastic nodal forces with MATRIX27 elements, a modal analysis was performed, the results are summarized in *Table 7.5*. Since it is known that flutter instability occurs usually in the first modes at lower frequencies, only the first 7 modes have been extracted, the 6th mode is a local one so it has been neglected.

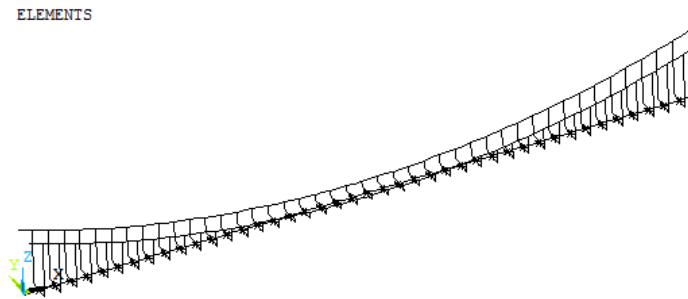


Figure 7.4: Finite element model of the George Washington Bridge (1931) without MATRIX27.

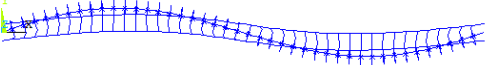
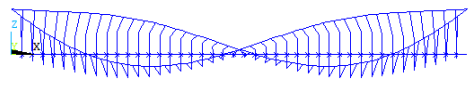
<p>DISPLACEMENT STEP=1 SUB =1 FREQ= .055917 DMX = .204E-03</p> 	<p>DISPLACEMENT STEP=1 SUB =2 FREQ= .109167 DMX = .243E-03</p> 
<i>Mode 1, L-S, 0.0559 Hz</i>	<i>Mode 2, (L+T)-A, 0.109 Hz</i>
<p>DISPLACEMENT STEP=1 SUB =3 FREQ= .116652 DMX = .199E-03</p> 	<p>DISPLACEMENT STEP=1 SUB =4 FREQ= .134989 DMX = .229E-03</p> 
<i>Mode 3, V-A, 0.1167 Hz</i>	<i>Mode 4, T-A, 0.1348 Hz</i>
<p>DISPLACEMENT STEP=1 SUB =5 FREQ= .159786 DMX = .257E-03</p> 	<p>DISPLACEMENT STEP=1 SUB =7 FREQ= .183385 DMX = .239E-03</p> 
<i>Mode 5, V-S, 0.159 Hz</i>	<i>Mode 7, (L+T)-S, 0.183 Hz</i>

Table 7-5: Modal frequencies and shapes of George Washington Bridge (1931).

Once evaluated the natural vibration frequencies, the flutter analysis has been performed with the method described in [33]. The aim of flutter analysis is to predict the lowest critical wind velocity that induces flutter instability, and the corresponding flutter frequency. MATRIX27 elements are then incorporated into the structural model to perform the damped modal analyses. A total of 84 elements are employed to formulate 42 aeroelastic stiffness and 42 aeroelastic damping. The hybrid finite element model incorporating structural model with MATRIX27 elements for flutter analysis is illustrated in *Figure 7.5*. The flutter derivatives of thin airfoil have been calculated with Eq. (2.4.4) – (2.4.11) where $C_{l,\alpha}$ and $C_{m,\alpha}$ has been calculated in *section 6.3*. In *Figure 7.6* the flutter derivatives are plotted as functions of the reduced wind speed.

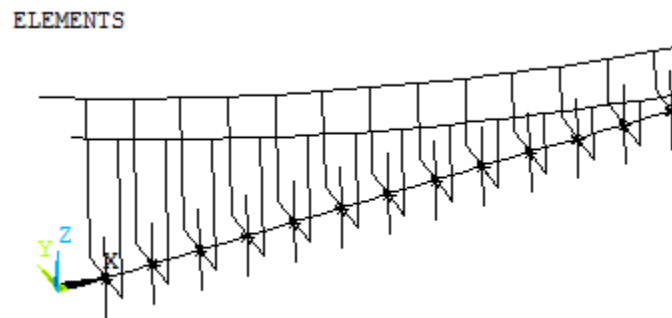


Figure 7.5: Finite element model with MATRIX 27 incorporated.

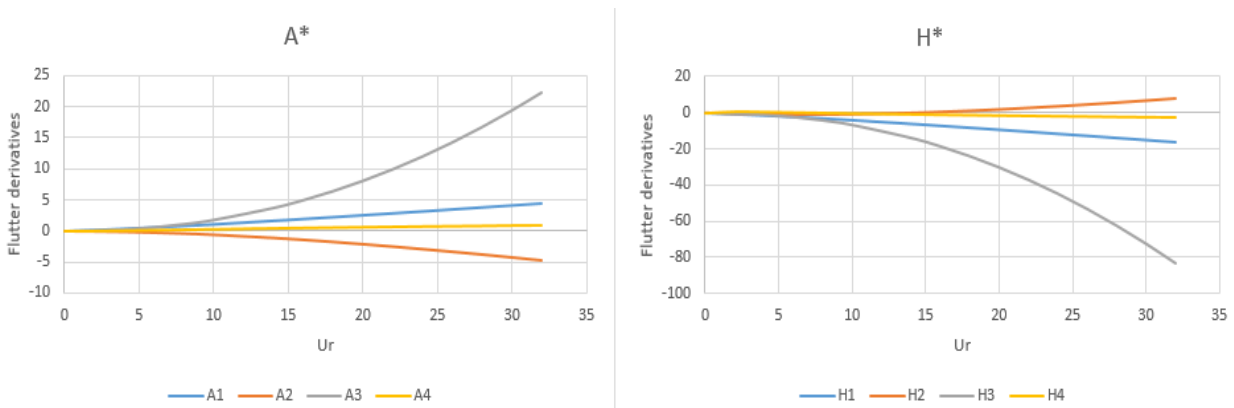


Figure 7.6: Flutter derivatives of George Washington Bridge (1931).

Finally, the iterative procedure for the determination of flutter speed and frequency has been carried out. Unlike the case study mentioned in the previous section, the computational steps have been followed for the first five modes extracted by the modal analysis and summarized in *Table 7.5*. The damped complex eigenvalue analyses were conducted for the model under wind velocities varying from 0 to 100 m/s. The increment step of wind velocity was set variable, from a maximum value of 20 m/s in the ranges far from the flutter instability to a minimum of 1 m/s around the instability. So the flutter velocity resultant has the accuracy of the unit (m/s). The first five conjugate pairs of complex eigenvalues and complex

eigenvectors are obtained, the variation of these complex eigenvalues versus wind velocity is plotted in *Figure 7.7*.

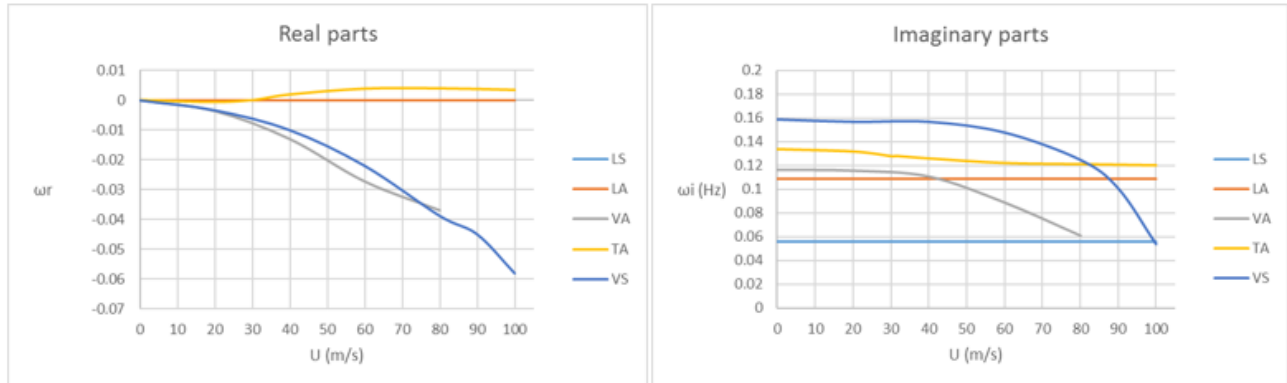


Figure 7.7: Variation of real and imaginary parts of complex eigenvalues versus wind velocity.

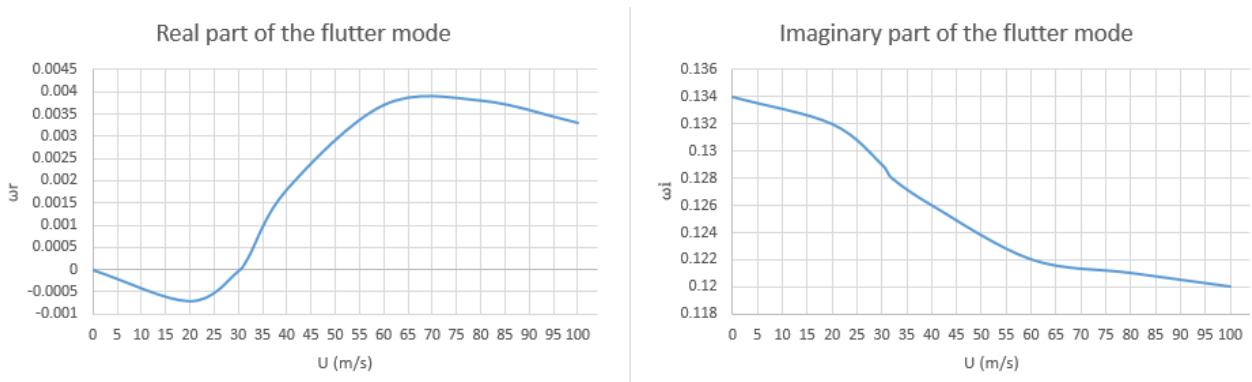


Figure 7.8: Variation of real and imaginary parts of the flutter mode.

The analysis furnished a flutter critical speed of 31 m/s and a critical frequency of 0.128 Hz.

This wind velocity, corresponding to 111,6 Km/h, belongs to the 11th level of the Beaufort scale that characterizes the “violent storms”. It is not a common situation, but for decree the safety of the bridge, several meteorological researches should be made. *Figure 7.7* shows that the frequencies of the lateral modes remain stable with the increase of the wind velocity, while the original values of vertical and torsional frequencies decrease, more strongly after the critical wind speed. It is not correct to assert that the torsional mode is the responsible of flutter instability condition, in fact a variation of the modal shape associated to the variation of the eigenvalues can be observed with the increase of the wind velocity. As stated in *Chapter 4*, the interaction between different modes is the triggering factor of the instability. Nevertheless, in a strictly analytic sense due to the model adopted, the variation of the torsional asymmetric mode (*Figure 7.8*) is the cause of the flutter instability. In fact, the flutter condition occurs when the real part of the complex eigenvalue became positive.

7.3. George Washington Bridge, double deck (1962)

The George Washington Bridge has been introduced in *section 1.1* and its sectional aerodynamic behavior was discussed in *section 6.4*. In this section a finite element model will be treated in order to study the global structure performance of the bridge, and finally determine the critic wind velocity and frequency that induce the flatter instability.

A “fish-bone” model was considered inappropriate to model the mechanical behavior of the double decked version of the bridge, further, no data was found in the literature regarding the mechanical properties. Hence, the entire truss of the central span has been modeled, with the only simplification regarding the slabs constituting the decks. As for the model treated in the previous section, the decks have been modeled using beam elements, this is a need arising from the method adopted to model the unsteady wind forces. The numerical model was realized with the properties listed in *Table 7.4*, and for the additional elements constituting the truss reference have been made to [40] and the main values are summarized in *Table 7.6*. All the elements, except the hangers, have been modeled with BEAM189. Unlike the “fish-bone” model, no rigid link and no MASS21 are needed in this model because the mechanical behavior is modeled by the interaction of the various elements. The numerical model is shown in *Figure 7.9*.

Elements	Cross section	Area [m ²]	Moment of inertia [m ⁴]	
Longitudinal upper beams	rectangular	1.82	I_{zz} 0.297	I_{yy} 0.256
Vertical beams	rectangular	1.82	I_{xx} 0.297	I_{yy} 0.256
Longitudinal lower beams	rectangular	0.9	I_{zz} 0.108	I_{yy} 0.042
V-shaped up-winds	rectangular	0.9	I_{11} 0.108	I_{22} 0.042
Transversal beams	I shaped	0.635	I_{xx} 0.886	I_{zz} 0.062

Table 7-6: Geometrical properties of the truss.

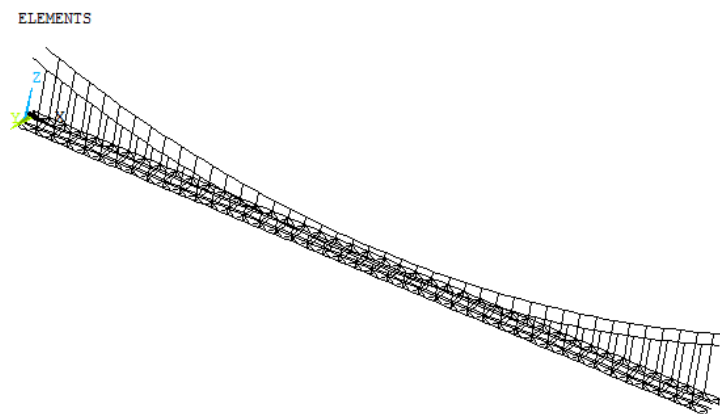


Figure 7.9: Finite element model of the George Washington Bridge (1962) without MATRIX27.

Before introducing the aeroelastic nodal forces with MATRIX27 elements, a modal analysis was performed, the results are summarized in *Table 7.5*. Since it is known that flutter instability occurs usually in the first modes at lower frequencies, only the first 8 modes have been extracted.

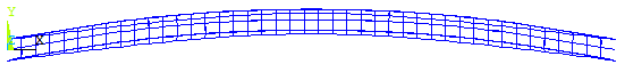
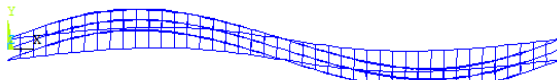
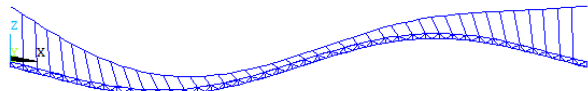
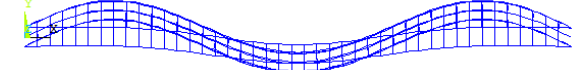
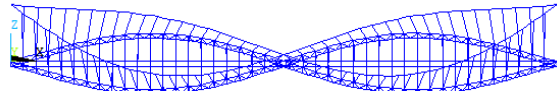
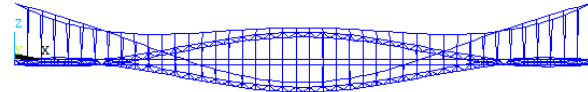
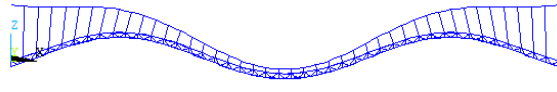
<p>DISPLACEMENT STEP=1 SUB =1 FREQ=.06475 DMX =.107E-03</p> 	<p>DISPLACEMENT STEP=1 SUB =2 FREQ=.117459 DMX =.115E-03</p> 
<i>Mode 1, L-S, 0.0647 Hz</i>	<i>Mode 2, (L+T)-A, 0.1174 Hz</i>
<p>DISPLACEMENT STEP=1 SUB =3 FREQ=.13672 DMX =.111E-03</p> 	<p>DISPLACEMENT STEP=1 SUB =4 FREQ=.158467 DMX =.142E-03</p> 
<i>Mode 3, V-A, 0.1367 Hz</i>	<i>Mode 4, V-S, 0.1584 Hz</i>
<p>DISPLACEMENT STEP=1 SUB =5 FREQ=.184211 DMX =.117E-03</p> 	<p>DISPLACEMENT STEP=1 SUB =6 FREQ=.193951 DMX =.139E-03</p> 
<i>Mode 5, (L+T)-S, 0.1842 Hz</i>	<i>Mode 6, T-A, 0.1939 Hz</i>
<p>DISPLACEMENT STEP=1 SUB =7 FREQ=.214941 DMX =.181E-03</p> 	<p>DISPLACEMENT STEP=1 SUB =8 FREQ=.225635 DMX =.122E-03</p> 
<i>Mode 7, T-S, 0.2149 Hz</i>	<i>Mode 8, V-S, 0.2256 Hz</i>

Table 7-7: Modal frequencies and shapes of George Washington Bridge (1962).

Once evaluated the natural vibration frequencies, the flutter analysis be performed with the method described in [33]. MATRIX27 elements must be incorporated into the structural model to perform the damped modal analyses. Since the aerodynamic parameters of the double deck modeled in *section 6.4* cannot be considered plenty reliable, two different methods have been proposed to model the aerodynamic forces acting on the bridge deck. Using the method developer in *section 4.4*, the aeroelastic loads are modeled as nodal forces modifying the stiffness matrix of the element to which the nodes belong.

The first method (*section 7.3.1*) consists in the application of the aeroelastic unsteady forces on the upper deck. Where the latter are expressed as functions of the flutter derivatives related to the aerodynamic coefficients calculated for the two decks in *section 6.4*.

The second method (*section 7.3.2*) has been proposed in order to avoid using the aerodynamic coefficients calculated in *section 6.4*. It consists in the application of the aeroelastic unsteady forces on both upper and lower deck. Where, in this case, the latter are expressed as functions of the flutter derivatives related to the aerodynamic coefficients calculated for the single deck in *section 6.3*. It is worth to underline that this method does not represent a linear add that should be forbidden in such a non-linear framework. Anyway this procedure is definitively wrong from different point of views. In fact, this simplification implies that there is no aerodynamic interference between the two decks, while the mechanical interference is correctly modeled by the elements composing the truss. Furthermore, the aerodynamic influence of the secondary truss elements is totally neglected.

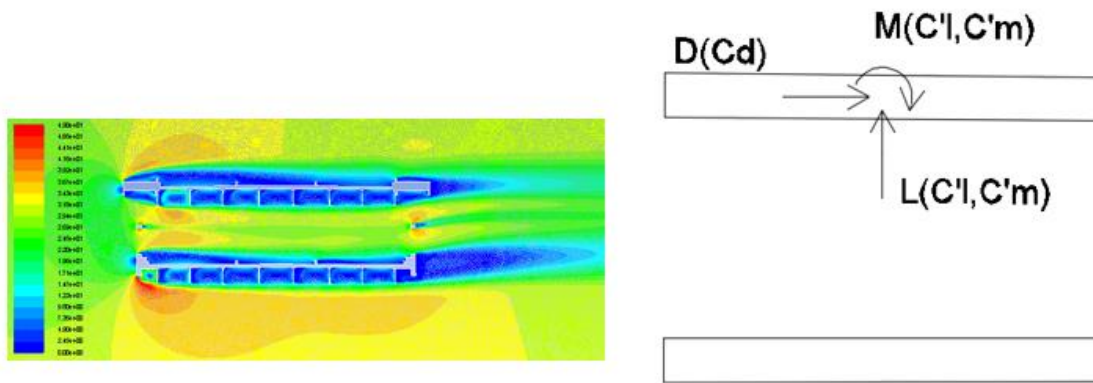


Figure 7.10: Schematization of the first method for the application of aeroelastic loads.

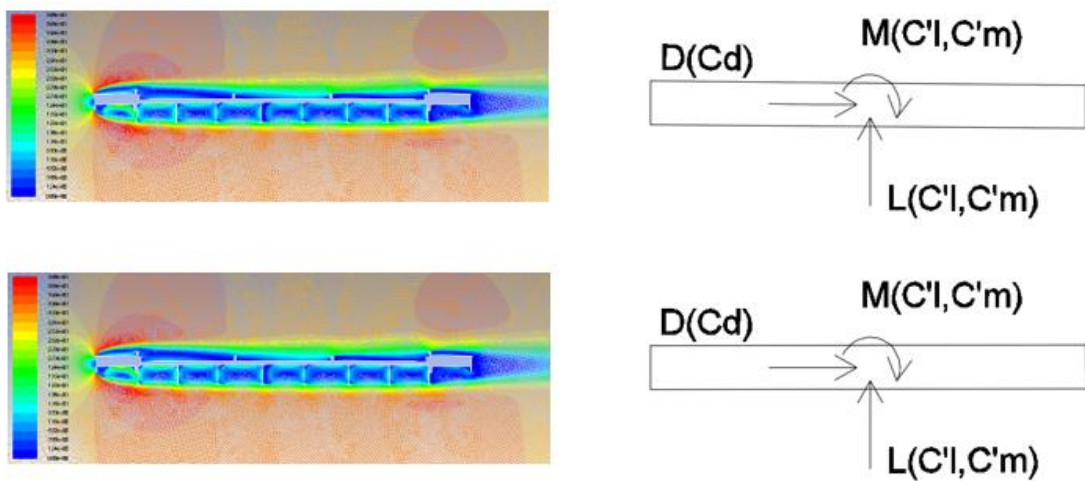


Figure 7.11: Schematization of the second method for the application of aeroelastic loads.

7.3.1. First method

As stated in the previous chapter, this method implies that the aerodynamic unsteady forces are applied only to the upper deck. A total of 84 elements are employed to formulate 42 aeroelastic stiffness and 42 aeroelastic damping. The hybrid finite element model incorporating structural model with MATRIX27 elements for flutter analysis is illustrated in *Figure 7.12*. The flutter derivatives of thin airfoil have been calculated with Eq. (2.4.4) – (2.4.11) where $C_{l,\alpha}$ and $C_{m,\alpha}$ has been calculated in *section 6.4*. In *Figure 7.13* the flutter derivatives are plotted as functions of the reduced wind speed.

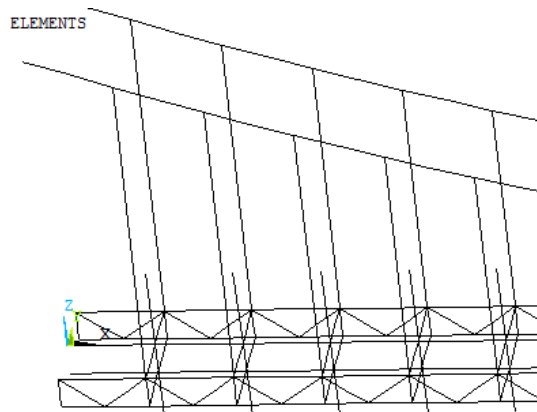


Figure 7.12: Finite element model with MATRIX 27 incorporated.

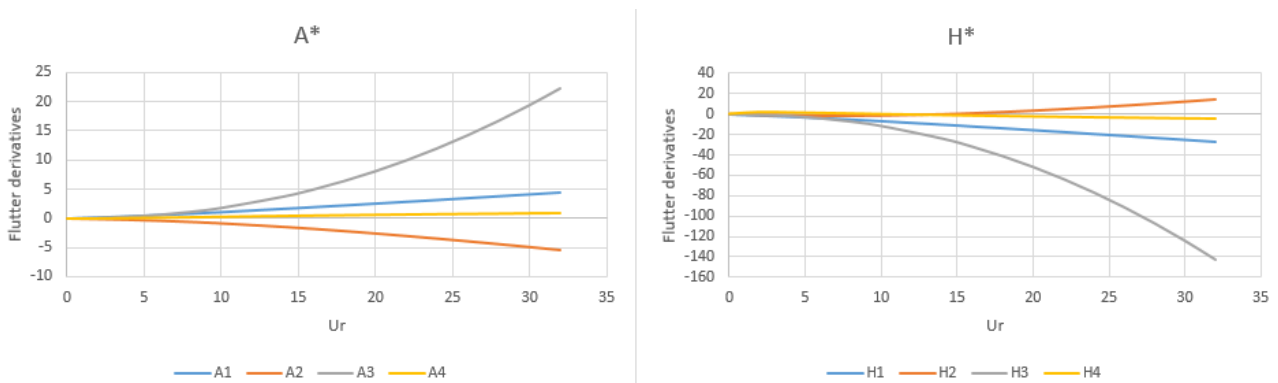


Figure 7.13 Flutter derivatives of George Washington Bridge (1962).

Finally, the iterative procedure for the determination of flutter speed and frequency has been carried out. The computational steps have been followed for the first seven modes extracted by the modal analysis and summarized in *Table 7.5*. The damped complex eigenvalue analyses were conducted for the model under wind velocities varying from 0 to 150 m/s. The increment step of wind velocity was set variable, from a maximum value of 20 m/s in the ranges far from the flutter instability to a minimum of 1 m/s

around the instability. Accordingly, the flutter wind velocity resultant has the accuracy of the unit (m/s). The first 7 conjugate pairs of complex eigenvalues and complex eigenvectors are obtained, the variation of these complex eigenvalues versus wind velocity is plotted in *Figure 7.14*.

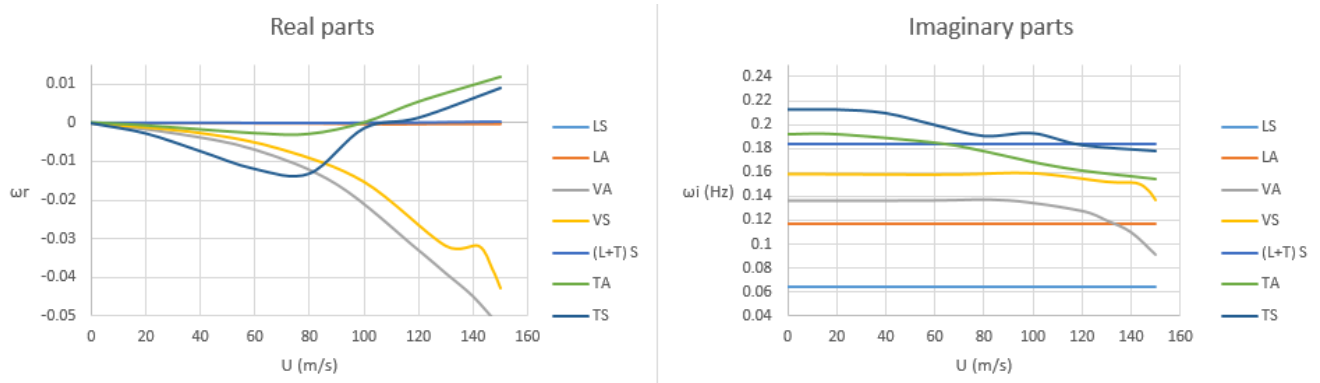


Figure 7.14: Variation of real and imaginary parts of complex eigenvalues versus wind velocity.

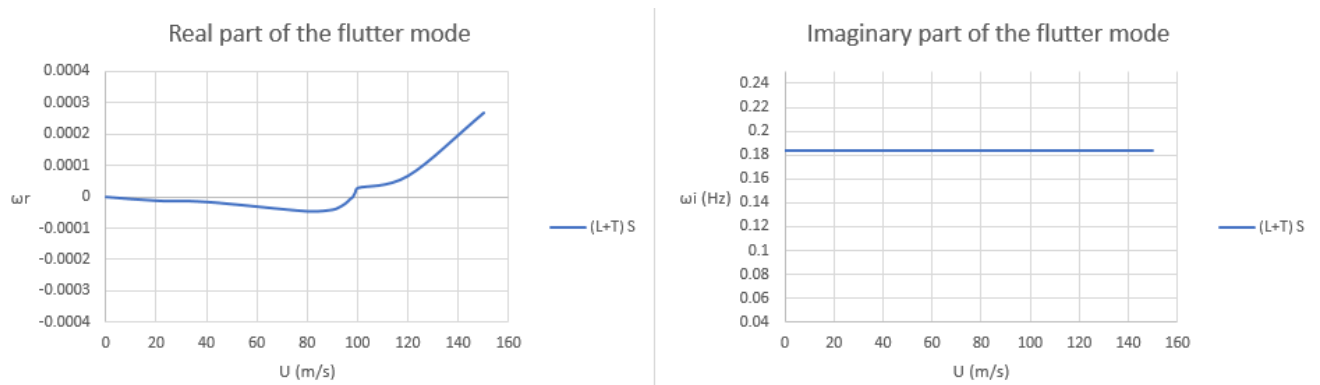


Figure 7.15: Variation of real and imaginary parts of the flutter mode.

The analysis furnished a flutter critical speed of 98 m/s and a critical frequency of 0.184 Hz. This wind velocity, corresponding to 352,8 Km/s, it is higher than the maximum ever recorded. *Figure 7.14* shows that the frequencies of the lateral modes remain stable with the increase of the wind velocity, while the original values of vertical and torsional frequencies decrease, more strongly after the critical wind speed. In a strictly analytic sense due to the model adopted, the variation of the 5th mode (*Figure 7.15*) is the cause of the flutter instability. In fact, the flutter condition occurs when the real part of the complex eigenvalue became positive. Nevertheless, as stated in *Chapter 4*, the interaction between different modes is the triggering factor of the instability. In this analysis the interaction is more evident than in the previous one. In fact, around the flutter wind velocity, the real part of three complex eigenvalues became positive, this aspect will be treated in *section 7.3.3* in order to make a comparison between the two different methods adopted.

7.3.2. Second method

This method has been proposed because allows to avoid the aerodynamic parameters obtained for the double decked version of the bridge in *section 6.4*. It implies that the aerodynamic unsteady forces are applied to both decks. A total of 168 elements are employed to formulate 84 aeroelastic stiffness and 84 aeroelastic damping. The hybrid finite element model incorporating structural model with MATRIX27 elements for flutter analysis is illustrated in *Figure 7.16*. Where blue elements are the MATRIX27 that represents the aeroelastic stiffness and damping of the upper deck, and the red elements are the MATRIX27 of the lower deck. The flutter derivatives are the same utilized in *section 7.1* for the single decked version (*Figure 7.6*).

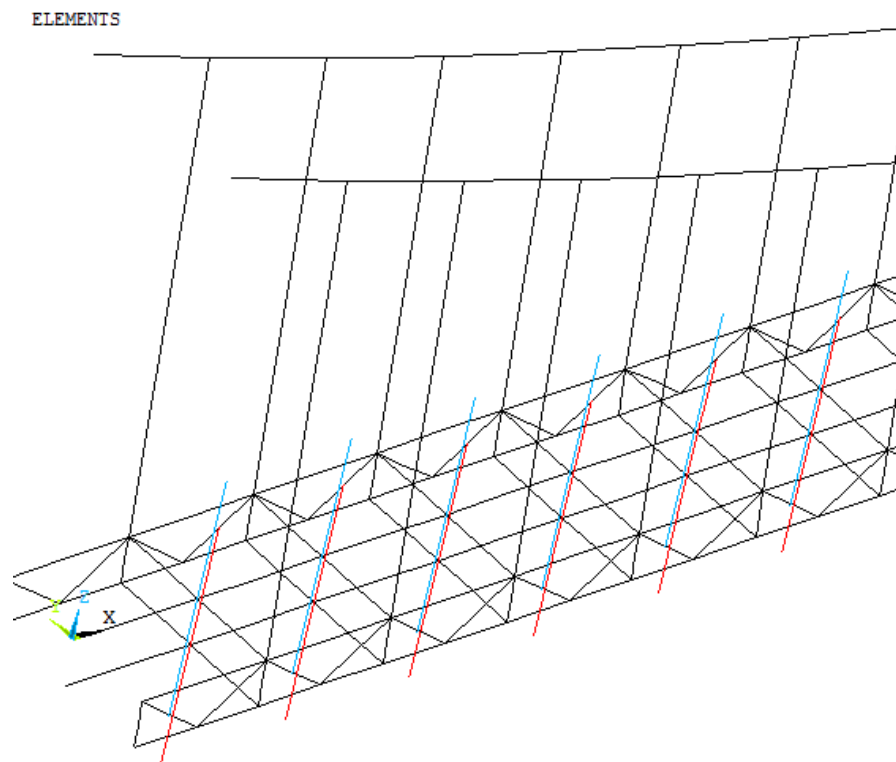


Figure 7.16: Finite element model with MATRIX 27 incorporated.

Finally, the iterative procedure for the determination of flutter speed and frequency has been carried out. The computational steps have been followed for the first seven modes extracted by the modal analysis and summarized in *Table 7.5*. The damped complex eigenvalue analyses were conducted for the model under wind velocities varying from 0 to 120 m/s. The increment step of wind velocity was set variable, from a maximum value of 20 m/s in the ranges far from the flutter instability to a minimum of 1 m/s around the instability. Accordingly, the flutter wind velocity resultant has the accuracy of the unit (m/s).

The first 7 conjugate pairs of complex eigenvalues and complex eigenvectors are obtained, the variation of these complex eigenvalues versus wind velocity is plotted in *Figure 7.17*.

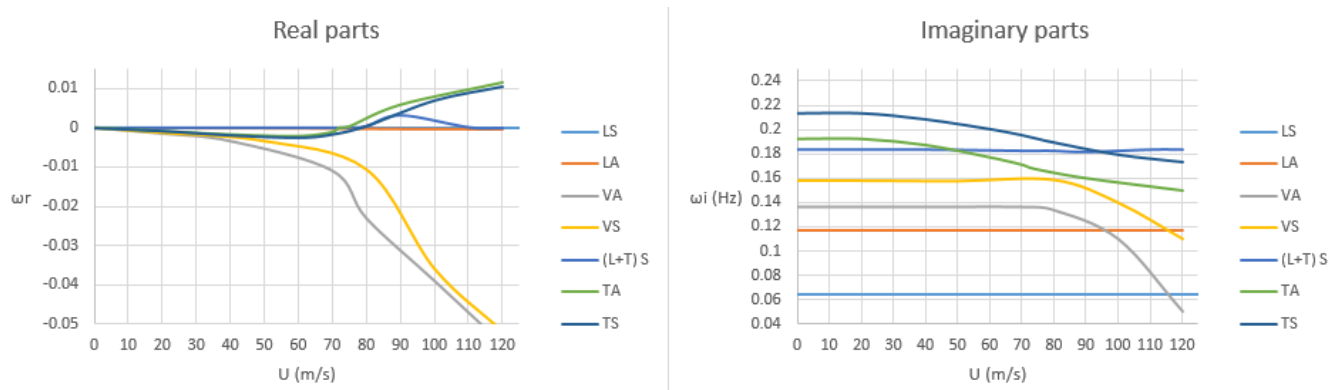


Figure 7.17: Variation of real and imaginary parts of complex eigenvalues versus wind velocity.

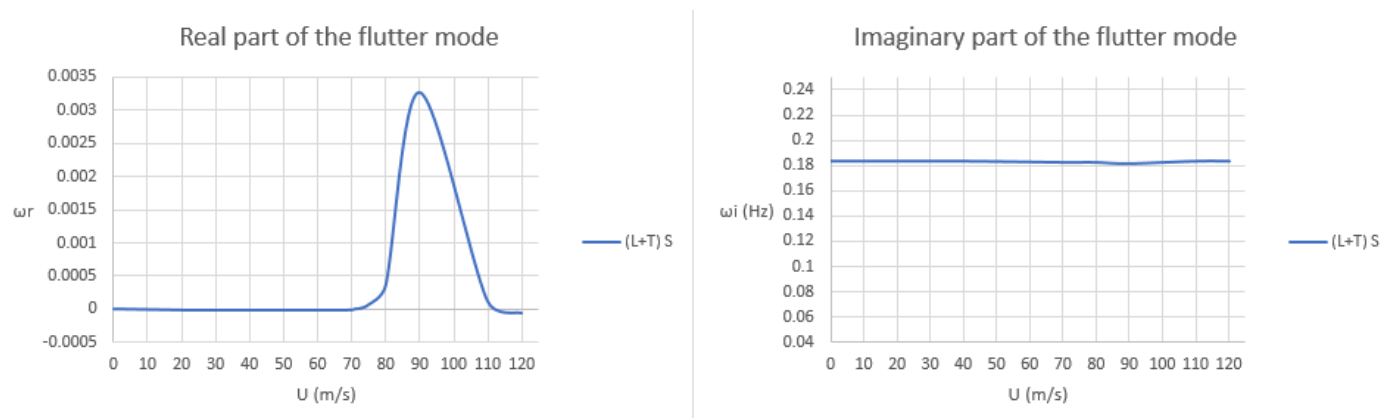


Figure 7.18: Variation of real and imaginary parts of the flutter mode versus wind velocity.

The analysis furnished a flutter critical speed of 71 m/s and a critical frequency of 0.183 Hz. This wind velocity, corresponding to 255.6 Km/h, belongs to the 5th and last category of the Saffir-Simpson scale of the hurricanes.

Figure 7.17 shows the same trends of the previous analyses: the frequencies of the lateral modes remain stable with the increase of the wind velocity, while the original values of vertical and torsional frequencies decrease, more strongly after the critical wind speed. In a strictly analytic sense due to the model adopted, the variation of the 5th mode (*Figure 7.18*) is the cause of the flutter instability. In fact, the flutter condition occurs when the real part of the complex eigenvalue became positive. Nevertheless, as stated in *Chapter 4*, the interaction between different modes is the triggering factor of the instability. In this analysis, as in the previous one, the interaction is underlined by the slope of the real part of different eigenvalues.

7.3.3. Comparison between the two methods

The two methods introduced represent a simplification of the real situation. The first, is commonly used [33] [41] for the analyses carried out with the method described in *section 4.4*, and provided good results compared with other obtained differently. Nevertheless, this method forces the center of the torsional rotation to lie in the deck axis. The validity of this assumption is related to the methods adopted for the calculation on flutter derivatives, that generally can be different. Regarding the second method, no applications have been found in literature, but no applications on double decked bridges have been found too. As mentioned before, this simplification implies that there is no aerodynamic interference between the two decks and furthermore, the aerodynamic influence of the secondary truss elements is totally neglected. Both assumptions are not so far from any realistic cases, but undoubtedly its validity must be proved. The two methods furnished significantly different values of critical wind speed, this could be attributed to the unreliability of the aerodynamic coefficients calculated for the double decked version of the bridge, on which are based the flutter derivatives of the first method. Alternatively, the cause can be attributed to the excessive simplifications on which the second method is based. Nevertheless, the methods provide a good agreement in terms of flutter frequency, and generally they show the same interaction between the different modes. In fact, both methods provide that the responsible mode of the flutter instability is the 5th (*Figures 7.15, 7.18*). Furthermore, the analyses conducted with the two methods show a similar trend of the complex eigenvalues related to the torsional modes around the flutter wind velocity (*Figure 7.19*).

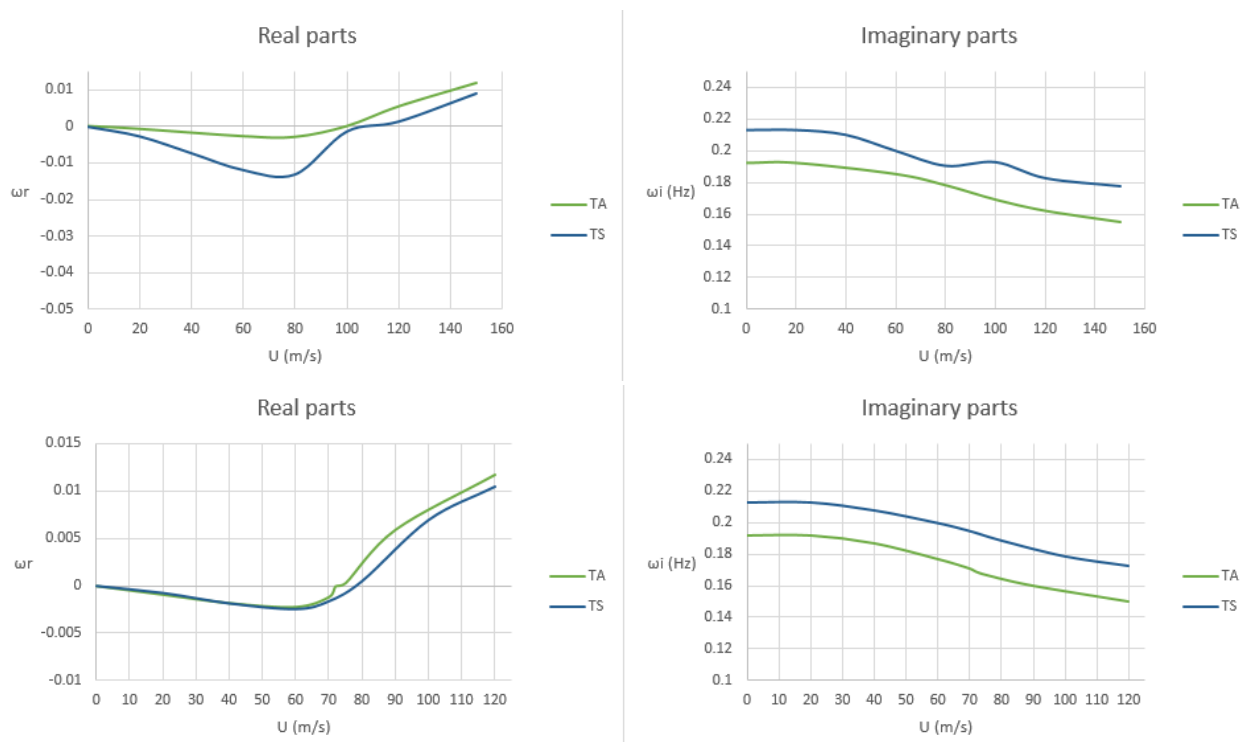


Figure 7.19: Variation of real and imaginary parts of the torsional modes versus wind velocity.

8. CONCLUSIONS AND FURTHER DEVELOPMENTS

The aerodynamic analysis of a long span suspension bridge represents a relevant challenge for the civil engineers. Most of the analytical models available for flutter analyses are based on the Scanlan aerodynamic parameters. Nowadays, the only reliable methods to calculate them, are based on sophisticated experimental tests on reduced models in the wind tunnel. In this work of thesis, it has been developed a simplified approach that allows to calculate the flutter derivatives by analytical formulations based on the aerodynamic static coefficients. Where the latter parameters have been calculated by *CFD* simulations using the finite element software ANSYS FLUENT. Once calculated the flutter derivatives, the goal was to determine the critical wind velocity that leads the bridge to the flutter instability adopting the commercial finite element software ANSYS APDL. Both, *CFD* and flutter analyses, have been carried out for the two versions of the bridge in order to evaluate the influence of the lower deck on the aerodynamic and mechanic behavior.

The results obtained in the three chapters of the second part can be summarized as follow:

The application of the simplified method, introduced for the calculation of flutter derivatives, has provided good results for the case studies analyzed in the 5th chapter. The main advantage of the method lies in the relative simplicity of the calculation of the aerodynamic static coefficients, on which the formulation is based. To further validate the method, it should be applied to several and different bridge decks, of which both aerodynamic static parameters and flutter derivatives are available for a comparison.

The methods applied in the *CFD* analyses provided good results for the 2D model of the Great Belt Est, while the results obtained for the application on the Akashi Kaikyo were considered unsatisfactory. The reason could lie in the difficult of representing the complex aerodynamic behavior of a truss girder by a two-dimensional model. In this area, many improvements can be made, only some of these are listed below:

- some detailed analyses could be carried out in order to better define the boundary conditions
- a more accurate model for the turbulence structure could be adopted
- a method to perform a 3D analysis with an affordable computational cost could be investigated

It is worth noting that in the context of *CFD*, several complex methods are already available even for the direct calculation of the flutter derivatives of bridge decks. So generally, a further development could be to reduce the computational cost of the existent methods.

Regarding the flutter analyses conducted in the seventh chapter, no literature results were available for a comparison. But the method adopted has been already validated in several cases [33] [41]. The innovative method proposed in *section 7.3.2* provided a good result in terms of flutter frequency, and generally a realistic outcome. It could represent a good solution for the design of double decked suspension bridges, it should be validated by more detailed analysis.

References

- [1] "Wikipedia," [Online]. Available: [https://en.wikipedia.org/wiki/Jacob%27s_Creek_Bridge_\(Pennsylvania\)](https://en.wikipedia.org/wiki/Jacob%27s_Creek_Bridge_(Pennsylvania)). [Accessed 10 October 2019].
- [2] R. Permata, "1.1 Motivation," in *Flutter Stabilization of Long Span Suspension Bridges with Slender Deck*, 2014, pp. I-1.
- [3] "Wikipedia," [Online]. Available: [https://en.wikipedia.org/wiki/Tacoma_Narrows_Bridge_\(1940\)](https://en.wikipedia.org/wiki/Tacoma_Narrows_Bridge_(1940)). [Accessed 10 October 2019].
- [4] [Online]. Available: (<http://www.acoustics.org/press/133rd/2psa1.html>). [Accessed 10 October 2019].
- [5] G. Piana, "5.3 Prospettive di sviluppo del lavoro presentato," in *Analisi Unitaria di Instabilità dei Ponti Sospesi*, Master thesis. Politecnico di Torino, 2009, p. 185.
- [6] "Wikipedia," [Online]. Available: https://en.wikipedia.org/wiki/George_Washington_Bridge. [Accessed 10 October 2019].
- [7] H. Wagner, "Über die entstehung des dynamischen auftriebes vontragflügeln. ZAMM," *Journal of Applied Mathematics and Mechanics* 5, p. 17–35., 1925.
- [8] T. Theodorsen, "General Theory of Aerodynamic Instability and the Mechanism of Flutter," *NACAReport*, 1935.
- [9] J. Caracoglia, "A methodology for the experimental extraction of indicial functions for streamlined and bluff deck sections," *Journal of Wind Engineering and Industrial Aerodynamics*, pp. 609-636, 2003.
- [10] L. Patruno, S. De Miranda, F. Ubertini, G. Vairo, "Indicial functions and flutter derivatives: A generalized approach to the motion-related wind loads," *Journal of Fluids and Structures* 42, pp. 466-487, 23 September 2013.
- [11] P. S. Brar, R. Raul, R. H. Scanlan, "Numerical Calculation of Flutter Derivatives via Indicial Functions," *Journal of Fluids and Structures*, pp. 337-351, 29 February 1996.
- [12] Bisplinghoff, R. , Ashley, H. , Halfman ,R., "Aeroelasticity," *Courier Dover Publications, New York*, 1996.
- [13] Y. Fung, "An Introduction to the Theory of Aeroelasticity," *Courier Dover Publications. New York*, 1993.

-
- [14] I. Garrick, "On Some Reciprocal Relations in the Theory of Non-stationary Flows," *NACA Report, 629.*, 1938.
- [15] Scanlan, R. ,Béliveau, J. , Budlong, K. ,, "Indicial aerodynamics functions for bridge decks.," *Journal of the Engineering Mechanics Division ASCE 100.*, 1974.
- [16] R. Scanlan, "Motion-related body-force functions in two-dimensional low-speed flow," *Journal of Fluids and Structures 14*, pp. 49-63, 2000.
- [17] Emil Simiu, Robert H. Scanlan, Wind effects on structures, John Wiley & Sons, Inc., 1996.
- [18] M. Rezeau, "Time-domain modelling of the wind forces acting on a bridge deck with indicial functions," Master Thesis. "Politecnico di Milano", 2010.
- [19] "CFD4AIRCRAFT," [Online]. Available: <http://www.cfd4aircraft.com/>. [Accessed 11 october 2019].
- [20] L. Bruno, "Modelli di turbolenza e procedure numeriche," in *Comportamento aerodinamico dei ponti di grande luce*, Phd thesis. Politecnico di Torino, 2000, p. 22.
- [21] F. Brusiani, Luca Patruno, "On the evaluation of bridge deck flutter derivatives using RANS," *Journal of Wind Engineering and Industrial Aerodynamics. 19*, pp. 39-47, 7 June 2013.
- [22] T. Tamura, "Reliability on CFD estimation for wind-structure interaction problems," *Journal of Wind Engineering and Industrial Aerodynamics 81*, pp. 117-143, 1999.
- [23] Tamura, T. , Ono, Y., "LES analysis on aeroelastic instability of prisms in turbulent flow," *Journal of Wind Engineering and Industrial Aerodynamics 91.*, pp. 1827-1846, 2003.
- [24] F. R. Menter, "Turbulence modeling for engineering flows," *Technical paper from Ansys Inc.*, 2011.
- [25] Som, S. ,Longman, D. E. ,Luo, Z. , Plomer, M. , Lu, T. , Senecal P. K. , Pomraning, E., "Simulating flame lift-off characteristics of diesel and biodiesel fuel using detailed chemical-kinetic mechanisms and LES turbulence model," *Proceedings of the ASME 2011 Internal Combustion Engine Division Fall Technical Conference*, 2011.
- [26] Versteeg, H. K. , Malalasekera, W. ,, An Introduction to Computational Fluid Dynamics: The Finite Volume Method, 2006.
- [27] D. C. Wilcox, Turbulence Modeling for CFD., DCW Industries Inc., 1998.
- [28] Menter, F. R. ,Kuntz, M. , Langtry, R., "Ten years of industrial experience with the SST turbulence model," *Turbulence Heat and Mass Transfer 4*, 2003.
- [29] Reinhold, T. A. , Brinch, M. , Damsgaard, A., Wind tunnel tests for the Great Belt Link, 1992.

-
- [30] Haojun Tang, Yongle Li, Yunfei Wang, Qiyu Tao, "Aerodynamic optimization for flutter performance of steel truss stiffening," *Journal of Wind Engineering & Industrial Aerodynamics* 168, pp. 260-270, 2017.
- [31] "Wikipedia," [Online]. Available: https://it.wikipedia.org/wiki/Golden_Gate_Bridge. [Accessed 10 October 2019].
- [32] A. Carpinteri, *Dinamica delle strutture*, Pitagora, 1998.
- [33] X.G. Hua, Z.Q. Chen, "Full-order and multimode flutter analysis using ANSYS," *Finite Elements in Analysis and Design* 44, pp. 537-551, 2008.
- [34] A. Al-Assaf, *Flutter Analysis of Open-Truss Stiffened Suspension Bridges Using Synthesized Aerodynamic Derivatives*, Phd Thesis. Washington State University, 2006.
- [35] A. Larsen, "Advances in aeroelastic analyses of suspension and cable-stayed bridges.," *Journal of Wind Engineering and Industrial Aerodynamics* 74, pp. 73-90, 1998.
- [36] A. Larsen, "Aerodynamic aspects of the final design of the 1624 m suspension bridge across the Great Belt," *Journal of Wind Engineering and Industrial Aerodynamics* 48, pp. 261-285, October 1993.
- [37] "Wikipwdia," [Online]. Available: https://it.wikipedia.org/wiki/Ponte_di_Akashi_Kaiky%C5%8D. [Accessed 10 October 2019].
- [38] Hiroshi Katsuchi, Nicholas P. Jones, Robert H. Scanlan, "Multimode Coupled Flutter and Buffeting Analysis," *ASCE*, 17 May 2015.
- [39] R. H. Scanlan, "Reexamination of sectional aerodynamic force," *Journal of Wind Engineering and Industrial Aerodynamics* 89, pp. 1257-1266, 27 May 2001.
- [40] L. G. Guidi, "Suspension bridge drawings," in *Long Span Bridges: the evolution of deck stiffening system and a case study on the seismic behaviour of a Maillart-Arch- Type Bridge: Viadotto Olivieri (SA)*, Phd Thesis. Università degli studi di napoli Federico II, pp. 56-64.
- [41] F. Di Agabito, *Flutter Analisis of Suspension Bridges in ANSYSS: The Akashi Kaikyo Bridge Case-Study*, Master thesis. Politecnico di Torino, 2018.
- [42] D. Cobo Del Arco, "5. Vibration Characteristics of the suspension bridges," in *An analysis of wind stability.Improvements to the response of suspension bridges*, 1998, pp. 5-4.